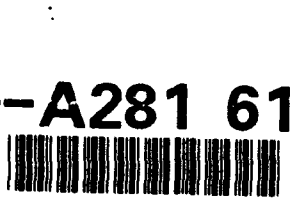

(1)

ARMY RESEARCH LABORATORY

Special Hybrid Stress Finite Elements for the Analysis of Interface Stress Distribution in Adhesive Joints

Erik Saether and Kristen Weight

ARL-TR-449 May 1994

The findings in this report are not to be construed as an official Department of the Army position unless so designated by other authorized documents.

Citation of manufacturer's or trade names does not constitute an official endorsement or approval of the use thereof.

Destroy this report when it is no longer needed. Do not return it to the originator.

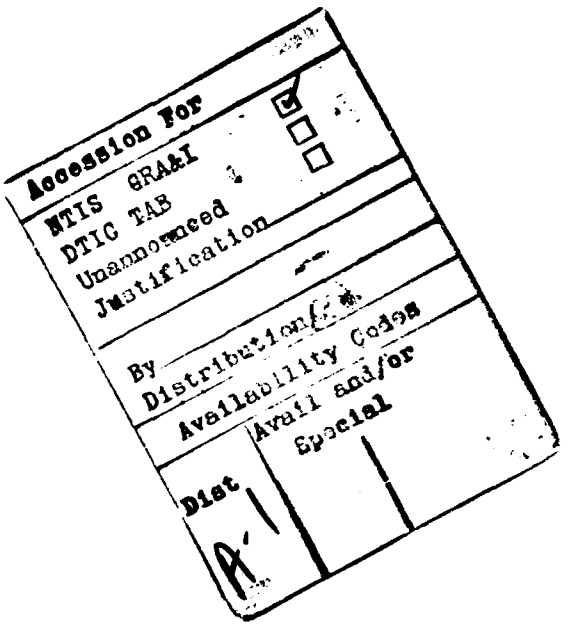

REPORT DOCUMENTATION PAGE

Form Approved
OMB No. 0704-0188

1. AGENCY USE ONLY (Leave blank)	2. REPORT DATE	3. REPORT TYPE AND DATES COVERED
	May 1994	Final Report

4. TITLE AND SUBTITLE
Special Hybrid Stress Finite Elements for the Analysis of Interface Stress Distribution in Adhesive Joints

5. FUNDING NUMBERS

6. AUTHOR(S)
Erik Saether and Kristen Weight

7. PERFORMING ORGANIZATION NAME(S) AND ADDRESS(ES)
U.S. Army Research Laboratory
Watertown, MA 02172-0001
ATTN: AMSRL-MA-PC

8. PERFORMING ORGANIZATION REPORT NUMBER
ARL-TR-449

9. SPONSORING/MONITORING AGENCY NAME(S) AND ADDRESS(ES)
U.S. Army Research Laboratory
2800 Powder Mill Road
Adelphi, MD 20783-1197

10. SPONSORING/MONITORING AGENCY REPORT NUMBER

11. SUPPLEMENTARY NOTES

12a. DISTRIBUTION/AVAILABILITY STATEMENT
Approved for public release; distribution unlimited.

12b. DISTRIBUTION CODE

13. ABSTRACT *(Maximum 200 words)*

The widespread application of adhesively bonded joints has necessitated the development of methodology to predict ultimate static joint strength and service life under cyclic loading. Due to the complexity of mathematically modelling adhesive joint response, analytical treatments are limited to highly idealized joint configurations, simplified assumed stress states, applied loading and material behavior. To overcome these limitations, a specialized finite element-based numerical approach is investigated wherein special 2-D and 3-D layered finite elements are formulated to improve the computational efficiency and accuracy of determining stresses in adhesive joints. The hybrid stress technique is used to explicitly enforce stress equilibrium throughout the element domain and stress continuity conditions at layer interfaces. The emphasis of this research is to explore a variety of possible element configurations to assess element performance. The optimum 2-D and 3-D element formulations demonstrate improved performance compared to standard displacement-based finite elements in predicting joint stresses.

14. SUBJECT TERMS
Finite element analysis, Adhesive joints

15. NUMBER OF PAGES
75

16. PRICE CODE

17. SECURITY CLASSIFICATION OF REPORT	18. SECURITY CLASSIFICATION OF THIS PAGE	19. SECURITY CLASSIFICATION OF ABSTRACT	20. LIMITATION OF ABSTRACT
Unclassified	Unclassified	Unclassified	UL

Contents

Figures

Contents (cont.)

Page

Figures

Contents (cont.)

Page

Figures

Contents (cont.)

Page

Figures

Page

Figures

Tables

1 Introduction

The use of adhesives in bonded joint concepts has given rise to a myriad of analytical and numerical treatments to ascertain the state of stress in critical regions of the bond to predict ultimate joint strength and service life. Analytical approaches have developed since the classic work of Golan and Reissner [1] in which the elastic response of a single-lap joint is analyzed using simplifying assumptions for the stress state and strain-displacement relations. Subsequent efforts have involved developing analyses accounting for various joint parameters such as nonisotropic adherends and bondline thickness effects [2-4], adhesive flexibility [3,5], geometric and material nonlinearity of the adhesive and adherends [6-10], effect of adhesive spew fillet [11,12], stress singularities [13-18], environmental effects [19], combined loading [20,21], and various joint configurations such as double lap, tapered and cylindrical [16,22,23].

For all the success of analytical approaches in elucidating the effect of joint parameters on joint behavior, an inescapable limitation is the complexity of incorporating all significant parameters in a single analytical framework for the analysis of general joint configurations. Such restrictions have limited the applicability of specialized analytic approaches for the design of practical bonded joint concepts. A preferred approach is a finite element based methodology which can provide a robust numerical technique to model any bonded joint configuration while theoretically capable of accounting for all joint variables.

Various finite element formulations specialized for the analysis of adhesive joints have been reported in the literature. A simple shear-spring element was developed in [24] which neglected the inclusion of normal stresses and was used to determine stress intensity factors in cracked and uncracked adherends. A specialized element was developed in [25] yielding a combined normal and shear-spring representation of the adhesive. Carpenter [26] formulated 1-D and 2-D elements to be joined to plate element approximations of the adherends which incorporate parameters allowing various simplifying assumptions regarding adhesive behavior to be represented in the element formulations in order to numerically simulate analytical results. An extension of Carpenter's approach to 3-D applications is presented in [27] but the element derived is a rod-type formulation not suited for 3-D elastic continuum representation. A mixed finite element is discussed in [28] which explicitly enforces interface stress conditions but details of the formulation are not presented and solutions are limited to butt joint configurations without comparison to reference solutions. In the present analysis, the aim has been to fully develop a finite element basis for a versatile numerical approach wherein the complete equations of 2-D and 3-D elasticity are used to accurately represent the elastic continuum and obtain results for actual adhesive joint configurations with realistic boundary conditions and applied loading. Of critical importance in the analysis of adhesive joints from a design standpoint are the accurate prediction of bondline stresses at the ends of the joint which tend to be maximum and, hence, the initiation sites for adhesive failure. The numerical prediction of stresses in these regions is complicated by the presence of boundary layer singularities at the joint ends due to the free-edge and material mismatch effects and by the nonlinear geometric and/or nonlinear material behavior of the joint under normal design load conditions. The present study has been conducted to evaluate the application of the hybrid stress element method [29-33] in special layered element configurations to accurately obtain bondline stresses. The selection of hybrid stress element formulations is motivated by the versatility inherent in the method by allowing independent assumptions regarding the stress and displacement field to be incorporated into element designs. The independence of stresses may be used in layered element configurations to strictly enforce stress continuity at the layer interfaces which is difficult in displacement-based element formulations. An additional capability is the modelling of zero traction boundary conditions which may be used to accurately represent true stress states at the bond ends. The present effort is thus aimed at fully exploring various modifications to the hybrid stress variational basis while formulating elements with various node configurations, layer combinations, order of interpolants and order of stress expansions to determine the optimum element design for application to predicting adhesive joint stresses. Numerous multi-layered 2-D and 3-D elements formulations are detailed herein to assess their relative performance in the prediction of interface stresses in adhesive joint configurations. With the emphasis on optimum element formulation, the present analysis is limited to linear elastic material behavior and a single common adhesive joint configuration is selected to benchmark element performance. Towards this aim, a single-lap joint configuration is selected for detailed comparative analysis. Additional enhancements such as the representation of nonlinear material and geometric behavior in the presence of singular stress fields are suggested for future development. The performance of the developed adhesive finite elements are compared with reference solutions obtained using a

highly discretized model of common single-lap adhesive joint configurations using higher-order displacement-based elements and demonstrate greater efficiency and accuracy of the developed hybrid stress elements. All specialized 'adhesive elements' were run using the ABAQUS commercial finite element program through the development of a user-defined subroutine. The complete source code and a description of the use of these elements is presented in [34].

2 Modelling Stresses in Adhesive Joints

In the joining of structural components, mechanical fastening techniques have the undesirable effect of creating highly complex stress fields and excessive stress intensification in the region of the fastener. As an alternative, adhesive bonding has been increasingly applied as a joining technique to alleviate the stress concentration by distributing the load transfer region. Although eliminating the concentration of binding forces in localized areas, however, adhesive bonding gives rise to a highly complex material system in the adhesive layer. In the local region of the adhesive-adherend interface exists a critical interphasal region in which various chemical species formed in the reaction of adhesive and adherend materials, together with possible reagents used as surface treatments to enhance bonding, create a complex stratification of material properties. Characterizing the mechanical properties of these transitional zones is important to quantify possible reductions in stiffness and strength compared to the bulk properties of the adhesive and adherend material. The modelling of adhesive layers thereby presents the common problem of scale in representing physical structures: at a microscopic level the representation of local stresses in the complex material system of the interface is of interest from the standpoint of fracture and failure; at a higher level, the global response of an entire adhesively bonded component is needed to determine overall stress distribution under applied service loads. It is the prediction of macroscopic behavior which is of interest in the current study; global stress predictions are required to provide an estimate of local stresses to be used in microstructural models for the detailed analysis of complex micromechanical response or in ultimate strength criteria for predicting the initiation of joint failure. The analysis of a structure or component containing an adhesive layer thus requires that the variation in the microstructure of the joint be neglected and gross mechanical properties used for a numerical representation. The material property variation in the local interface region are replaced by the assumption of a homogeneous continuum in order to predict the transfer of normal and shear loads between the adherends through the adhesive layer. The critical stresses are thus generated as normal and tangential components along the adhesive/adherend interface, normally in the region of the ends of the joint. At a structural level of analysis, complications arise in the finite element analysis of adhesive stresses due, in general, to the inherent mathematical idealizations made in representing an adhesive joint and, in particular, to the assumption of linear elastic material response. The interaction of free edges and material mismatch at the bond ends tend to give rise to stress singularities and may be resolved through the incorporation of assumed singular stress fields in the element formulations or, most simply, the region in the area of the singularity may be regarded as nonconvergent and material yielding is assumed *a priori*. Nonlinear viscoelastic and plastic material behavior of the adhesive under service loads commonly tend to reduce peak stresses at the joint ends through redistribution of joint loads. A linear analysis of adhesive stresses using appropriate failure prediction methods such as the average stress criteria is, therefore, conservative in predicting joint strength.

A numerical simulation of critical joint stresses requires an accurate modelling of adhesively bonded sections. This, in turn, requires an accurate representation of the elastic continuum of the adhesive and adherends along the bond line. Standard finite element formulations cannot simultaneously model the discontinuous jump in material properties while maintaining continuity of stresses across the adherend/adhesive interface. Nonlinear geometric and/or material behavior may be accounted for through a variety of solution procedures accounting for large displacements and viscoelastic/plastic material models. The focus of the current research is to assess the application of the hybrid stress technique through the development of novel element configurations to accurately account for material property discontinuity while maintaining stress continuity at the critical adhesive/adherend interfaces in 2-D and 3-D bonded joint configurations. The primary goal is to rigorously assess possible special element designs involving different orders of assumed displacements, node configuration, number of layers, assumed orders of stress expansions and constraints imposed on the stress field to determine the optimum element formulation. In order to limit the amount of joint

variables to discern comparative element behavior, analyses are restricted to a single common adhesive joint configuration incorporating linear elastic material behavior and small displacement response to applied loads.

3 Variational Basis for Specialized Adhesive Elements

The hybrid stress finite element method is used in the present study to develop specialized layered element formulations. The structure of the constituent element matrices are defined by the Hellinger-Reissner functional in which stresses and displacements are assumed as independent field quantities. Alternative statements of the basic hybrid stress variational basis may be utilized to optimize element performance through assumptions made in the selection and treatment of independence of assumed stress fields. Two basic versions of the variational basis are investigated and are referred to as the 'full' and 'partial' hybrid stress method which are detailed below.

3.1 Full Hybrid Stress Method

The complete Hellinger-Reissner functional may be stated as

$$\Pi_R = \int_v [(-1/2)\boldsymbol{\sigma}^T \mathbf{S}\boldsymbol{\sigma} + \boldsymbol{\sigma}^T(\mathbf{Lu})]dv - \int_s \mathbf{u}^T \mathbf{t} ds \tag{1}$$

where $\boldsymbol{\sigma}$ is the assumed stress field, $\mathbf{S}$ is the material compliance matrix, $\mathbf{u}$ is the assumed displacement field, $\mathbf{L}$ is the differential operator relating strains to displacements, and $\mathbf{t}$ are applied surface tractions over a portion of the element boundary, s.
The assumed stresses for the i^{th} layer may be represented by

$$\boldsymbol{\sigma}^i = \mathbf{P}^i \boldsymbol{\beta}^i \tag{2}$$

where $\mathbf{P}^i$ is a matrix of polynomial terms and $\boldsymbol{\beta}^i$ is a vector of undetermined expansion coefficients.
The displacement field is assumed over the i^{th} layer domain as

$$\mathbf{u}^i = \mathbf{N}^i \mathbf{q}^i \tag{3}$$

where $\mathbf{N}^i$ are compatible isoparametric displacement shape functions and $\mathbf{q}^i$ are nodal displacements. Neglecting applied tractions and substituting (2) and (3) into (1) yields

$$\Pi_R^i = \int_v [(-1/2)\boldsymbol{\beta}^{i^T} \mathbf{P}^{i^T} \mathbf{S}^i \mathbf{P}^i \boldsymbol{\beta}^i + \boldsymbol{\beta}^{i^T} \mathbf{P}^{i^T} (\mathbf{LN})^i] \mathbf{q}^i] dv \tag{4}$$

or

$$\Pi_R^i = (-1/2)\boldsymbol{\beta}^{i^T} \mathbf{H}^i \boldsymbol{\beta}^i + \boldsymbol{\beta}^{i^T} \mathbf{G}^i \mathbf{q}^i \tag{5}$$

where

$$\mathbf{H}^i = \int_v \mathbf{P}^{i^T} \mathbf{S}^i \mathbf{P}^i dv \tag{6}$$

$$\mathbf{G}^i = \int_v \mathbf{P}^{i^T} (\mathbf{LN}^i) dv = \int_v \mathbf{P}^{i^T} \mathbf{B}^i dv \tag{7}$$

Performing local assembly over the N element layers yields

$$\Pi_R = \sum_{i=1}^{N} \Pi_R^i = (-1/2)\boldsymbol{\beta}^T \mathbf{H} \boldsymbol{\beta} + \boldsymbol{\beta}^T \mathbf{G} \mathbf{q} \tag{8}$$

Seeking a stationary value of the functional by taking the first variation with respect to $\boldsymbol{\beta}$ yields

$$\boldsymbol{\beta} = \mathbf{H}^{-1} \mathbf{G} \mathbf{q} \tag{9}$$

By substituting $\boldsymbol{\beta}$ into (8), the variation with respect to $\mathbf{q}$ yields the element stiffness matrix as

$$\mathbf{K} = \mathbf{G}^T \mathbf{H}^{-1} \mathbf{G} \tag{10}$$

3.2 Partial Hybrid Stress Method

An augmentation of the full hybrid stress variational basis can be made in which not all stress components are represented by independently assumed stress expansions. The resulting basis, called the partial hybrid stress method, incorporates independently assumed stresses for selected components while the remaining components are obtained directly from the assumed displacement functions as in classical displacement-based element formulations. This gives the total stress field as the sum

$$\boldsymbol{\sigma} = \boldsymbol{\sigma}_1 + \boldsymbol{\sigma}_2 \tag{11}$$

Assumed independent stress components for the i^{th} layer are given by

$$\boldsymbol{\sigma}_1^i = \mathbf{P}^i \boldsymbol{\beta}^i \tag{12}$$

while the remaining stress components are derived from assumed displacements in the i^{th} layer and are expressed as

$$\boldsymbol{\sigma}_2^i = \mathbf{C}^i \mathbf{B}^i \mathbf{q}^i \tag{13}$$

where $\mathbf{C}^i$ is the material stiffness matrix partition relating dependent stresses to strains, $\mathbf{B}^i$ is the strain-displacement matrix and $\mathbf{q}^i$ is the vector of nodal displacements. The variational statement of the partial Hellinger-Reissner functional neglecting applied surface tractions may be stated as

$$\Pi_R^i = \int_v [(1/2)\mathbf{q}^{i^T} \mathbf{B}^{i^T} \mathbf{C}^i \mathbf{B}^i \mathbf{q}^i + \boldsymbol{\beta}^{i^T} \mathbf{P}^{i^T} \mathbf{B}^i \mathbf{q}^i - (1/2)\boldsymbol{\beta}^{i^T} \mathbf{P}^{i^T} \mathbf{S}^i \mathbf{P}^i \boldsymbol{\beta}^i] dv \tag{14}$$

where the constituent matrices for $\mathbf{G}^i$ and $\mathbf{H}^i$ are defined above. Performing local assembly over the element layers yields

$$\Pi_R = \sum_{i=1}^{N} \Pi_R^i = \int_v [(1/2)\mathbf{q}^T \mathbf{B}^T \mathbf{C} \mathbf{B} \mathbf{q} + \boldsymbol{\beta}^T \mathbf{G} \mathbf{q} - (1/2)\boldsymbol{\beta}^T \mathbf{H} \boldsymbol{\beta}] dv \tag{15}$$

Taking variations with respect to the independent field quantities, the contributions to the element stiffness matrix due to assumed stresses is given by

$$\mathbf{K}_1 = \mathbf{G}^T \mathbf{H}^{-1} \mathbf{G} \tag{16}$$

and the contribution due to assumed displacements is given by

$$\mathbf{K}_2 = \int_v \mathbf{B}^T \mathbf{C} \mathbf{B} dv \tag{17}$$

The total element stiffness matrix is therefore given by the sum

$$\mathbf{K} = \mathbf{K}_1 + \mathbf{K}_2 \tag{18}$$

This formulation minimizes the computational cost associated with the hybrid method and offers the benefit of increasing the accuracy of selected stress components while allowing other components to be computed less accurately from assumed displacements. The partial hybrid formulation is used to assess 2-D element performance for potential application in 3-D layered element formulations in which the large number of independent stress modes used for maintaining complete expansions may be minimized while suppressing zero energy modes. An important aspect of the partial variational statement is that it precludes the enforcement of all field equilibrium conditions on the element stresses which may limit element performance in specific applications.

Additional variations to both of the above hybrid variational basis may be made through the selective relaxation of layer equilibrium and interface stress continuity constraints.

4 Layered Element Formulations

In using the hybrid approach, the constituent matrices of individual layers are locally assembled and stress continuity conditions may be explicitly enforced at layer interfaces resulting in novel element formulations ideally capable of representing the stress state at material interfaces. In the historical development of the hybrid stress method, the improvement in element behavior has been offset by an ostensibly greater computational cost in forming element stiffness coefficients. This has resulted in the convention of utilizing minimum expansions for assumed stress components to minimize additional cost over displacement-based element formulations. Although the basic assumption that the hybrid stress technique inherently requires a greater computational cost over displacement-based element formulations has been disputed recently in References [35,36], the development of specialized elements presupposes a limited use of such elements in a complete structural finite element model. Thus, the computational efficiency of specialized elements are regarded as of secondary importance and complete emphasis is placed on developing element formulations which provide the most accurate stress prediction. An additional aspect of the hybrid method has been the problem of selecting assumed stress fields which suppress spurious zero energy modes in the resulting element stiffness matrix. This has been solved by the development of rational procedures for selecting stress expansions based on stresses assumed in mapped or natural coordinates [32,33]. In this approach a contravariant transformation based on Jacobians computed at the element centroid is used to map natural stresses into physical coordinates. For the elements developed in the current study, a minor geometric restriction is imposed which requires that all element layers are rectangular. This requirement simplifies the mapping function and allows stresses to be assumed in physical coordinates. In the selection of assumed stresses, complete stress expansions for each layer of various orders are used to assess element characteristics and performance.

The various treatments of selected stress fields and the performance of 2-D and 3-D specialized layered elements – or 'adhesive elements' – are presented below.

4.1 2-D Layered Element Configurations

Figure 1 depicts typical layered element configurations used in the present study to represent a 2-D elastic continuum. Nodal variables are restricted to u and v translational degrees of freedom. The isoparametric displacement fields presented below are assumed independently within each element layer; superscripts denoting layer designation have been dropped for clarity.

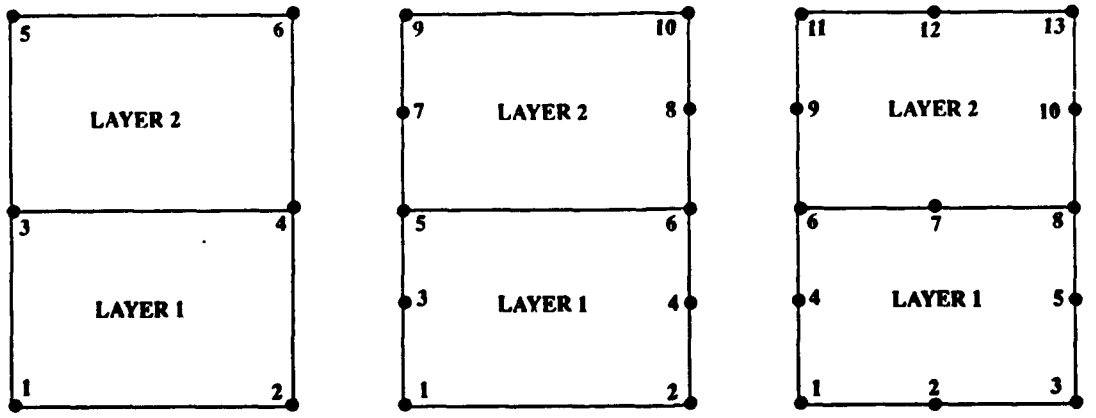

Figure 1. Typical 2-D layered element configurations.

As shown in Figure 2, a local coordinate system is assumed within each layer with the origin situated at the layer centroid. For the various element configurations shown in Figure 1, the layer displacement shape functions are presented below.

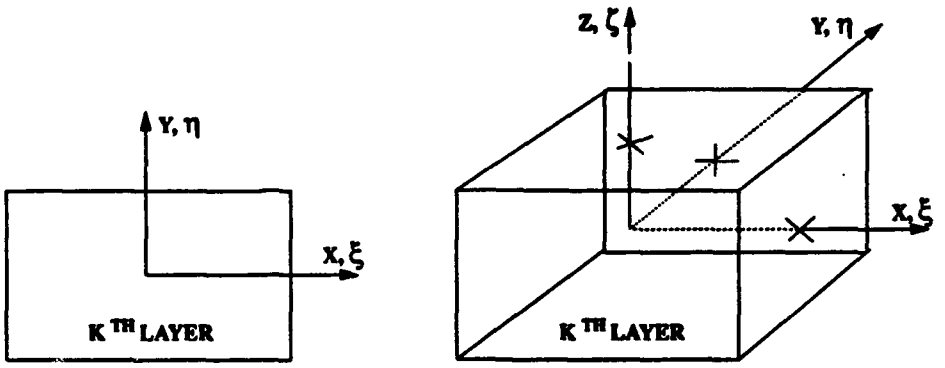

Figure 2. Local and mapped layer coordinate systems in 2-D and 3-D elements.

For a linear element with 4 nodes per layer, the isoparametric displacement functions $\mathbf{u}_q$ are given by

$$\mathbf{u}_q = \begin{pmatrix} u_q \\ v_q \end{pmatrix} = \frac{1}{4}\sum_{i=1}^{4}(1+\xi_i\xi)(1+\eta_i\eta)\begin{pmatrix} u_i \\ v_i \end{pmatrix} = \mathbf{N}_i\mathbf{q} \tag{19}$$

The mapping between physical and natural coordinates is given by

$$\begin{aligned} x &= a_0 + a_1\xi + a_2\eta + a_3\xi\eta \\ y &= b_0 + b_1\xi + b_2\eta + b_3\xi\eta \end{aligned} \tag{20}$$

where

$$\begin{bmatrix} a_0 & b_0 \\ a_1 & b_1 \\ a_2 & b_2 \\ a_3 & b_3 \end{bmatrix} = \frac{1}{4}\begin{bmatrix} 1 & 1 & 1 & 1 \\ -1 & 1 & -1 & 1 \\ -1 & -1 & 1 & 1 \\ 1 & -1 & -1 & 1 \end{bmatrix}\begin{bmatrix} x_1 & y_1 \\ x_2 & y_2 \\ x_3 & y_3 \\ x_4 & y_4 \end{bmatrix} \tag{21}$$

For a higher-order element with 8 nodes per layer, the isoparametric displacement functions $\mathbf{u}_q$ are given by

$$\mathbf{u}_q = \begin{pmatrix} u_q \\ v_q \end{pmatrix} = \frac{1}{4}\sum_{i=1}^{8}\mathbf{N}_i\begin{pmatrix} u_i \\ v_i \end{pmatrix} = \mathbf{N}_i\mathbf{q} \tag{22}$$

where

$$\mathbf{N}_i = \begin{Bmatrix} N_1 \\ N_2 \\ N_3 \\ N_4 \\ N_5 \\ N_6 \\ N_7 \\ N_8 \end{Bmatrix} = \begin{Bmatrix} (1-\xi)(1-\eta)(-1-\xi-\eta) \\ 2(1-\xi^2)(1-\eta) \\ (1+\xi)(1-\eta)(-1+\xi-\eta) \\ 2(1-\xi)(1-\eta^2) \\ 2(1+\xi)(1-\eta^2) \\ (1-\xi)(1+\eta)(-1-\xi+\eta) \\ 2(1-\xi^2)(1+\eta) \\ (1+\xi)(1+\eta)(-1+\xi+\eta) \end{Bmatrix} \tag{23}$$

The mapping between physical and natural coordinates is given by

$$\begin{aligned} x &= a_0 + a_1\xi + a_2\eta + a_3\xi\eta + a_4\xi^2 + a_5\eta^2 + a_6\xi^2\eta + a_7\xi\eta^2 \\ y &= b_0 + b_1\xi + b_2\eta + b_3\xi\eta + b_4\xi^2 + b_5\eta^2 + b_6\xi^2\eta + b_7\xi\eta^2 \end{aligned} \tag{24}$$

where

$$\begin{bmatrix} a_0 & b_0 \\ a_1 & b_1 \\ a_2 & b_2 \\ a_3 & b_3 \\ a_4 & b_4 \\ a_5 & b_5 \\ a_6 & b_6 \\ a_7 & b_7 \\ a_8 & b_8 \end{bmatrix} = \frac{1}{4} \begin{bmatrix} -1 & 2 & -1 & 2 & 2 & -1 & 2 & -1 \\ 0 & 0 & 0 & -2 & 2 & 0 & 0 & 0 \\ 0 & -2 & 0 & 0 & 0 & 0 & 2 & 0 \\ 1 & 0 & -1 & 0 & 0 & -1 & 0 & 1 \\ 1 & -2 & 1 & 0 & 0 & 1 & -2 & 0 \\ 1 & 0 & 1 & -2 & -2 & 1 & 0 & 1 \\ -1 & 2 & -1 & 0 & 0 & 1 & -2 & 1 \\ -1 & 0 & 1 & 2 & -2 & -1 & 0 & 1 \end{bmatrix} \begin{bmatrix} x_1 & y_1 \\ x_2 & y_2 \\ x_3 & y_3 \\ x_4 & y_4 \\ x_5 & y_5 \\ x_6 & y_6 \\ x_7 & y_7 \\ x_8 & y_8 \end{bmatrix} \tag{25}$$

For a mixed-order element with displacements assumed as a linear function of the x coordinate and a quadratic function of y resulting in 6 nodes per layer, the isoparametric displacement functions $\mathbf{u}_q$ are given by

$$\mathbf{u}_q = \begin{pmatrix} u_q \\ v_q \end{pmatrix} = \frac{1}{4} \sum_{i=1}^{6} \mathbf{N}_i \begin{pmatrix} u_i \\ v_i \end{pmatrix} = \mathbf{N}_i \mathbf{q} \tag{26}$$

where

$$\mathbf{N}_i = \begin{Bmatrix} N_1 \\ N_2 \\ N_3 \\ N_4 \\ N_5 \\ N_6 \end{Bmatrix} = \begin{Bmatrix} \eta(1-\xi)(\eta-1) \\ \eta(1+\xi)(\eta-1) \\ 2(1-\xi)(1-\eta^2) \\ 2(1+\xi)(1-\eta^2) \\ \eta(1-\xi)(1+\eta) \\ \eta(1+\xi)(1+\eta) \end{Bmatrix} \tag{27}$$

The mapping between physical and natural coordinates is given by

$$\begin{aligned} x &= a_0 + a_1\xi + a_2\eta + a_3\xi\eta + a_4\eta^2 + a_5\xi\eta^2 \\ y &= b_0 + b_1\xi + b_2\eta + b_3\xi\eta + b_4\eta^2 + b_5\xi\eta^2 \end{aligned} \tag{28}$$

where

$$\begin{bmatrix} a_0 & b_0 \\ a_1 & b_1 \\ a_2 & b_2 \\ a_3 & b_3 \\ a_4 & b_4 \\ a_5 & b_5 \\ a_6 & b_6 \end{bmatrix} = \frac{1}{4} \begin{bmatrix} 0 & 0 & 2 & 2 & 0 & 0 \\ 0 & 0 & -2 & 2 & 0 & 0 \\ -1 & -1 & 0 & 0 & 1 & 1 \\ 1 & -1 & 0 & 0 & -1 & 1 \\ 1 & 1 & -2 & -2 & 1 & 1 \\ -1 & 1 & 2 & -2 & -1 & 1 \end{bmatrix} \begin{bmatrix} x_1 & y_1 \\ x_2 & y_2 \\ x_3 & y_3 \\ x_4 & y_4 \\ x_5 & y_5 \\ x_6 & y_6 \end{bmatrix} \tag{29}$$

Stress equilibrium conditions for the i^{th} layer are given by

$$\frac{\delta\sigma^i_{xx}}{\delta x} + \frac{\delta\tau^i_{xy}}{\delta y} = 0, \qquad \frac{\delta\tau^i_{xy}}{\delta x} + \frac{\delta\sigma^i_{yy}}{\delta y} = 0 \tag{30}$$

Continuity conditions for stresses at the layer interfaces are given by

$$\begin{aligned} \sigma^i_{yy}|_{\eta=h_i} &= \sigma^{i+1}_{yy}|_{\eta=-h_{i+1}} \\ \tau^i_{xy}|_{\eta=h_i} &= \tau^{i+1}_{xy}|_{\eta=-h_{i+1}} \end{aligned} \tag{31}$$

In the use of the partial hybrid formulation, only the normal and shear stress components are approximated through independent expansions. *A priori* enforcement of layer equilibrium is reduced to the condition

$$\frac{\delta\tau^i_{xy}}{\delta x} + \frac{\delta\sigma^i_{yy}}{\delta y} = 0 \tag{32}$$

while the interface continuity conditions remain those given in (31).

4.2 3-D Layered Element Configurations

Representative 3-D element configurations incorporating multiple layers are depicted in Figure 3.

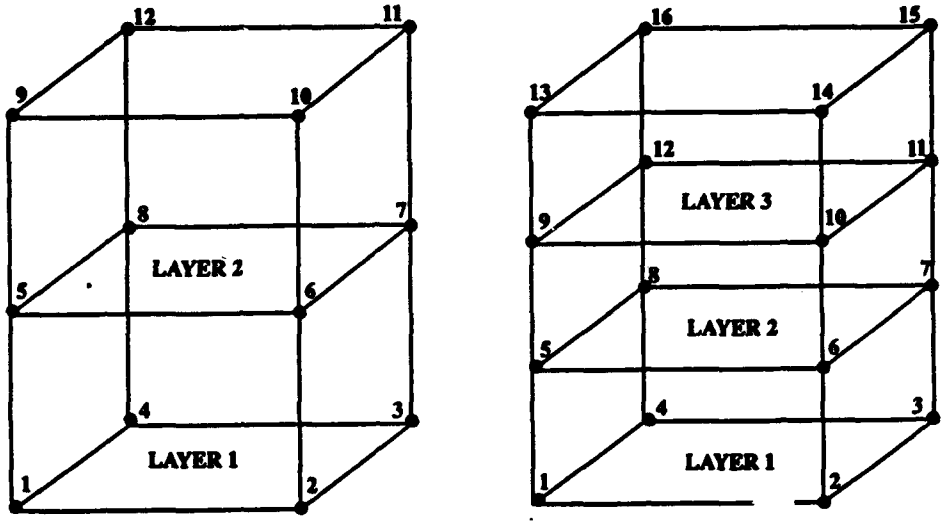

Figure 3. Typical 3-D layered element configurations.

The isoparametric displacement functions $\mathbf{u}_q$ for each layer are given by

$$\mathbf{u}_q = \begin{Bmatrix} u_q \\ v_q \\ w_q \end{Bmatrix} = \frac{1}{8}\sum_{i=1}^{8}(1+\xi_i\xi)(1+\eta_i\eta)(1+\zeta_i\zeta)\begin{Bmatrix} u_i \\ v_i \\ w_i \end{Bmatrix} = \mathbf{N}_i\mathbf{q} \tag{33}$$

The isoparametric mapping between physical and natural coordinates is given by

$$\begin{aligned} x &= a_0 + a_1\xi + a_2\eta + a_3\zeta + a_4\xi\eta + a_5\xi\zeta + a_6\eta\zeta + a_7\xi\eta\zeta \\ y &= b_0 + b_1\xi + b_2\eta + b_3\zeta + b_4\xi\eta + b_5\xi\zeta + b_6\eta\zeta + b_7\xi\eta\zeta \\ z &= c_0 + c_1\xi + c_2\eta + c_3\zeta + c_4\xi\eta + c_5\xi\zeta + c_6\eta\zeta + c_7\xi\eta\zeta \end{aligned} \tag{34}$$

where

$$\begin{bmatrix} a_0 & b_0 & c_0 \\ a_1 & b_1 & c_1 \\ a_2 & b_2 & c_2 \\ a_3 & b_3 & c_3 \\ a_4 & b_4 & c_4 \\ a_5 & b_5 & c_5 \\ a_6 & b_6 & c_6 \\ a_7 & b_7 & c_7 \end{bmatrix} = \frac{1}{8}\begin{bmatrix} 1 & 1 & 1 & 1 & 1 & 1 & 1 & 1 \\ -1 & 1 & 1 & -1 & -1 & 1 & 1 & -1 \\ -1 & -1 & 1 & 1 & -1 & -1 & 1 & 1 \\ -1 & -1 & -1 & -1 & 1 & 1 & 1 & 1 \\ 1 & -1 & 1 & -1 & 1 & -1 & 1 & -1 \\ 1 & -1 & -1 & 1 & -1 & 1 & 1 & -1 \\ 1 & 1 & -1 & -1 & -1 & -1 & 1 & 1 \\ -1 & 1 & -1 & 1 & 1 & -1 & 1 & -1 \end{bmatrix}\begin{bmatrix} x_1 & y_1 & z_1 \\ x_2 & y_2 & z_2 \\ x_3 & y_3 & z_3 \\ x_4 & y_4 & z_4 \\ x_5 & y_5 & z_5 \\ x_6 & y_6 & z_6 \\ x_7 & y_7 & z_7 \\ x_8 & y_8 & z_8 \end{bmatrix} \tag{35}$$

Stress equilibrium conditions for the i^{th} layer are given by

$$\begin{aligned} \frac{\delta\sigma^i_{xx}}{\delta x} + \frac{\delta\tau^i_{xy}}{\delta y} + \frac{\delta\tau^i_{xz}}{\delta z} &= 0 \\ \frac{\delta\tau^i_{xy}}{\delta x} + \frac{\delta\sigma^i_{yy}}{\delta y} + \frac{\delta\tau^i_{yz}}{\delta z} &= 0 \\ \frac{\delta\tau^i_{xz}}{\delta x} + \frac{\delta\tau^i_{yz}}{\delta y} + \frac{\delta\sigma^i_{zz}}{\delta z} &= 0 \end{aligned} \tag{36}$$

Continuity conditions of stresses at the layer interfaces are given by

$$\begin{aligned} \sigma^i_{zz}|_{\zeta=h_i} &= \sigma^{i+1}_{zz}|_{\zeta=-h_{i+1}} \\ \tau^i_{zx}|_{\zeta=h_i} &= \tau^{i+1}_{zx}|_{\zeta=-h_{i+1}} \\ \tau^i_{yz}|_{\zeta=h_i} &= \tau^{i+1}_{yz}|_{\zeta=-h_{i+1}} \end{aligned} \tag{37}$$

In the partial hybrid approach, only the σ_z, τ_{zx} and τ_{yz} components are based on independently assumed stress expansions. The enforcement of equilibrium throughout the i^{th} layer domain is limited to

$$\frac{\delta\tau^i_{xz}}{\delta x} + \frac{\delta\tau^i_{yz}}{\delta y} + \frac{\delta\sigma^i_{zz}}{\delta z} = 0 \tag{38}$$

The continuity conditions of stresses at the layer interfaces remain the same as given in (37).

5 Benchmark Solutions for Adhesive Stresses

A variety of 2-D and 3-D layered element formulations have been derived to assess the effect of element layers and order of stress expansion on the accuracy of stress prediction. All elements have been supported for use in the ABAQUS commercial finite element program through a user-defined subroutine [34]. The developed elements are benchmarked using a 2-D single-lap joint shown in Figure 4 and two 3-D single-lap joints with a rectangular and tapered planform configuration as shown in Figures 5 and 6. In order to assess the accuracy of stress prediction using specialized elements, a reference solution was obtained by using a highly discretized 2-D finite element model incorporating a large number of higher-order displacement-based 8-node plane-strain elements. Regular meshes were used for each model domain with the discretization indicated using the notation (n_x, n_y) to indicate the number of elements used in the x and y directions, respectively. The boundary conditions and applied loading used in both 2-D and 3-D single-lap models are depicted in Figure 7. The roller supports at the adherend ends are applied over the first few elements to enforce a zero curvature condition. The uniform applied load, P, is distributed as a tensile load over the joint end in the upper adherend while fixity conditions are applied at the opposite end of the lower adherend. Although numerous analytical approaches have been presented in the literature for the analysis of single-lap joints, all incorporate simplifying assumptions in order to yield closed-form solutions which are incompatible with the approximation framework of finite element theory. As an example, governing differential equations describing a single-lap joint are presented in Reference [15] and were solved to generate an analytical solution for bondline stresses. Assumptions made in deriving the governing equations include zero transverse deformation of the adherends, constant stresses through the adhesive thickness and joint flexibility primarily due to deformation in the adhesive layer. As shown in Figures 8 and 9, the analytical solution does not match the solution obtained numerically using a finite element based approach - most notably in the region near the singular point present in the finite element analysis assuming linear elastic material response - and hence is unsuitable for the present study.

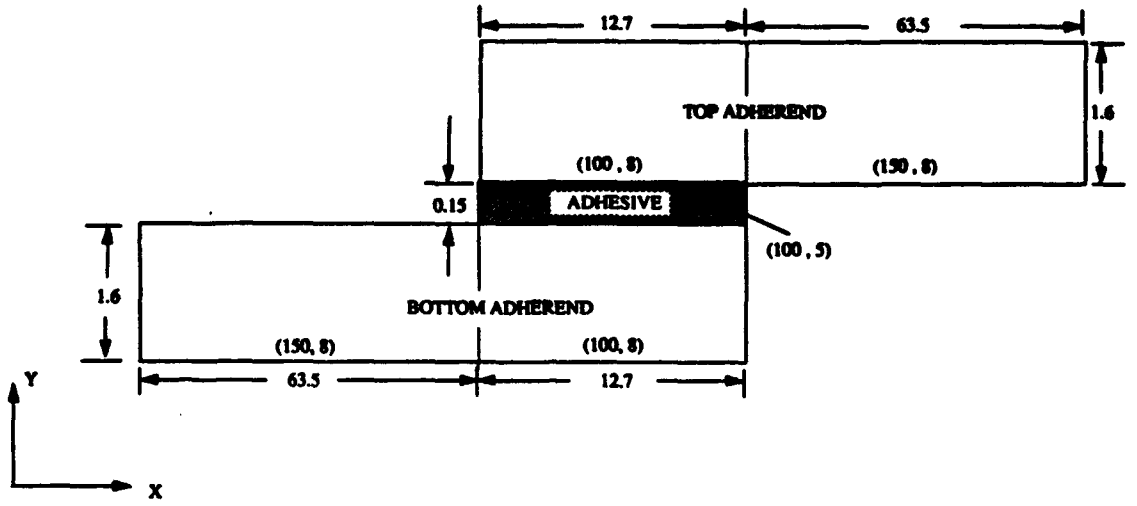

Figure 4. Geometry of a 2-D single-lap joint model and discretization used for the reference solution.

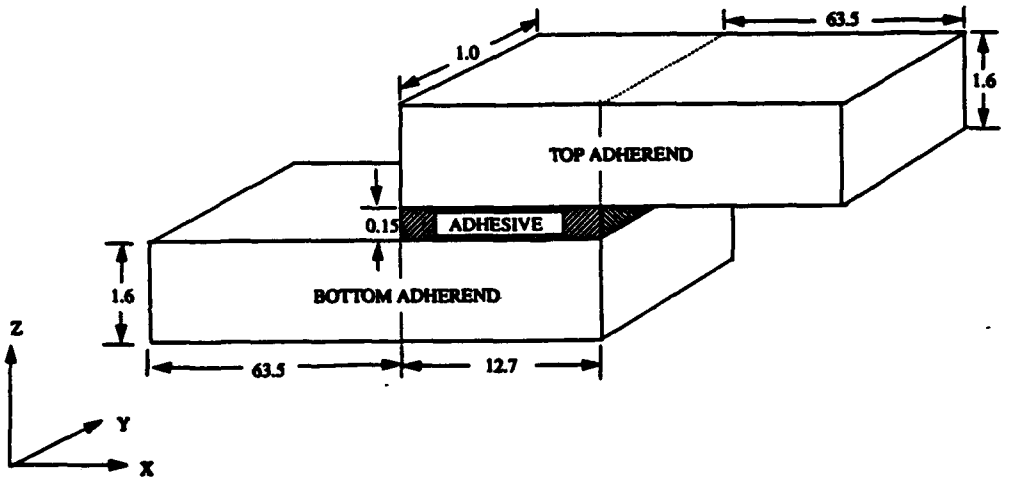

Figure 5. Geometry of a 3-D single-lap joint model with rectangular planform.

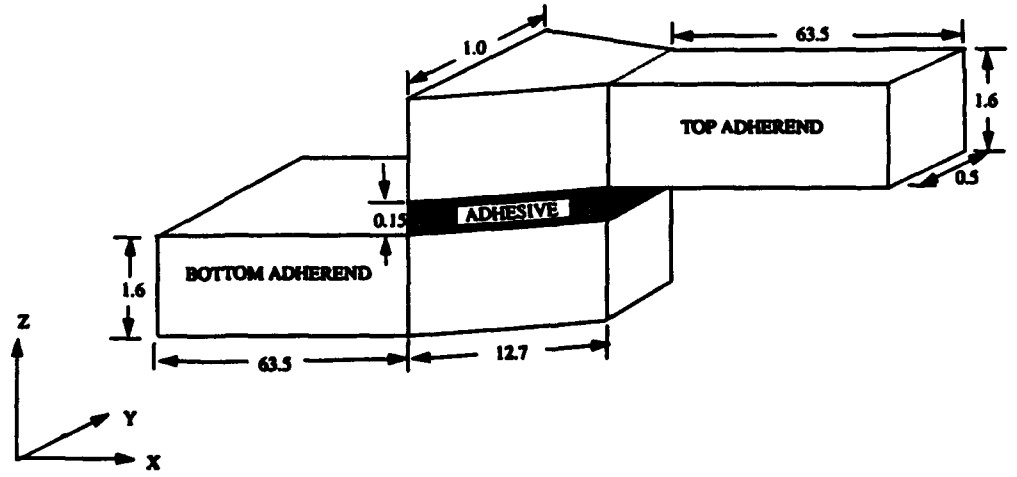

Figure 6. Geometry of a 3-D single-lap joint model with a tapered planform.

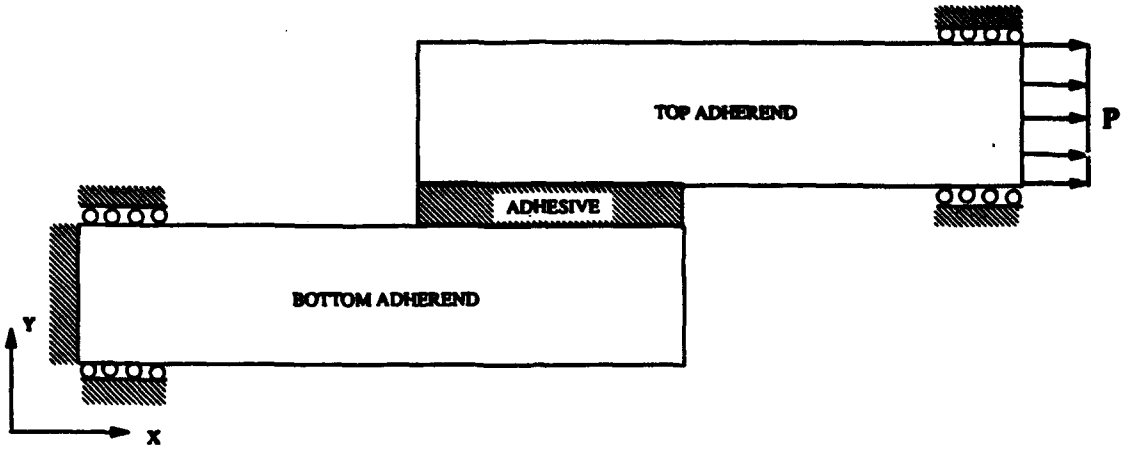

Figure 7. Boundary conditions used to define the single-lap joint model supports.

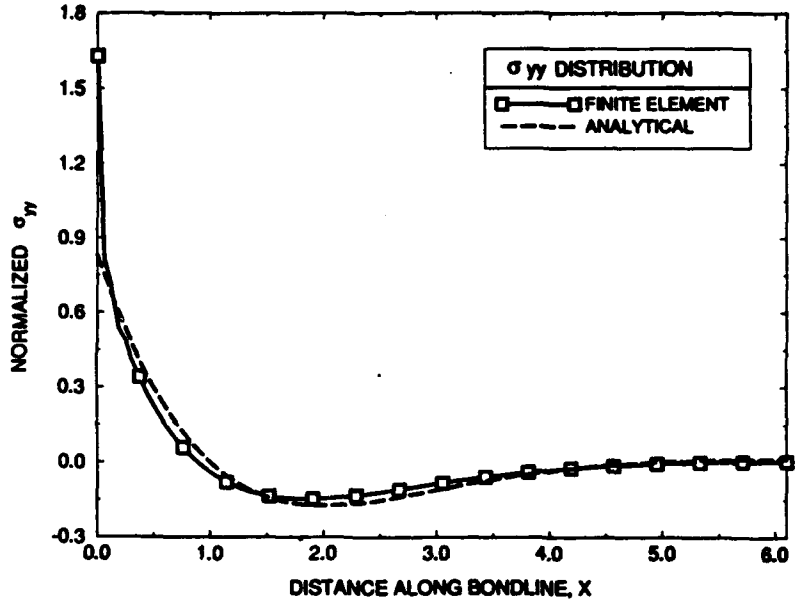

Figure 8. Analytic and finite element prediction of σ_{yy} stresses along bondline in a single-lap joint.

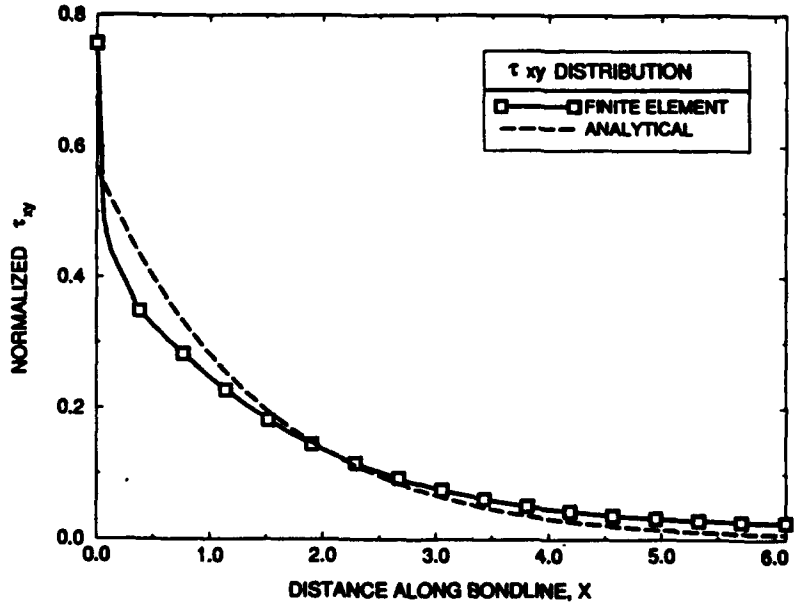

Figure 9. Analytic and finite element prediction of τ_{xy} stresses along bondline in a single-lap joint.

In addition to providing the reference solution for developed 2-D elements, the plane-strain solution is used directly as a reference solution for the 3-D single-lap joint with rectangular planform assuming negligible variation of stresses through the joint width. For the tapered 3-D single-lap joint, the bondline stresses in the reference solution are scaled according to

$$\begin{aligned} \sigma_{zz} &= (1 + x/l)\sigma_{yy} \\ \sigma_{xz} &= (1 + x/l)\sigma_{xy} \end{aligned} \tag{39}$$

where x is the axial coordinate and l is to total bond length.

Numerous element formulations and their performance are detailed in the following sections. Different combinations of element layers, node configuration, element order, stress field selection and the use of 'full' and 'partial' hybrid stress variational bases are assessed. Due to the significantly greater degree of developmental effort in 3-D element formulations, basic element performance is assessed in 2-D configurations. The optimum element design is then carried over to the development of a 3-D element. The development of a generic 3-D element with optimum stress prediction capablilities is the ultimate aim of the current research to provide a versatile numerical tool for the modelling of any arbitrary 3-D joint configuration.

6 2-D Special Adhesive Elements

Various 2-D elements are formulated and their accuracy in predicting joint stresses is assessed through a relative comparison with the reference solution. As explained above, a detailed study of 2-D element configurations is performed to ascertain the optimum element configuration based on node configurations, number of element layers, order of assumed displacement shape functions, order of assumed stress expansions and variations in stress field constraints for the development of an optimum 3-D element formulation which involves a significantly greater degree of complexity in basic formulation. The various 2-D element formulations and their accuracy in predicting joint stresses in a single-lap configuration are discussed in detail below. In the discussions of particular element performance, statements regarding the hybrid stress finite element method are presented which may provide general insight into the use of this variational basis for specialized layered finite element formulations for other intended applications. To assess the convergence of the derived elements, four different models utilizing 10, 25, 50 and 100 elements along the bondline, were constructed and compared to the reference solution. These models were specifically constructed with nonoptimal meshes in the use of available degrees of freedom in the local region of the adhesive bond to assess element performance in models with high aspect ratios and significant jumps in the degree of mesh refinement between regions in the model. The models are depicted in Figure 10 with the discretization indicated in various regions by the notation (N_xxN_y) where N_i denotes the number of elements used along the i^{th} coordinate axis. The width of the joint is assumed to be unity and isotropic material properties are selected as:

$$\textit{Adherend}: \quad E = 69000.0 \quad \mu = 0.32$$

$$\textit{Adhesive}: \quad E = 3000.0 \quad \mu = 0.36$$

All stresses are normalized as $\sigma^*_{ij} = \sigma_{ij}/\sigma_{ref}$ where $\sigma_{ref} = P/A$ in which P is a uniformly applied tensile load and A is the cross-sectional area of the adherend end.

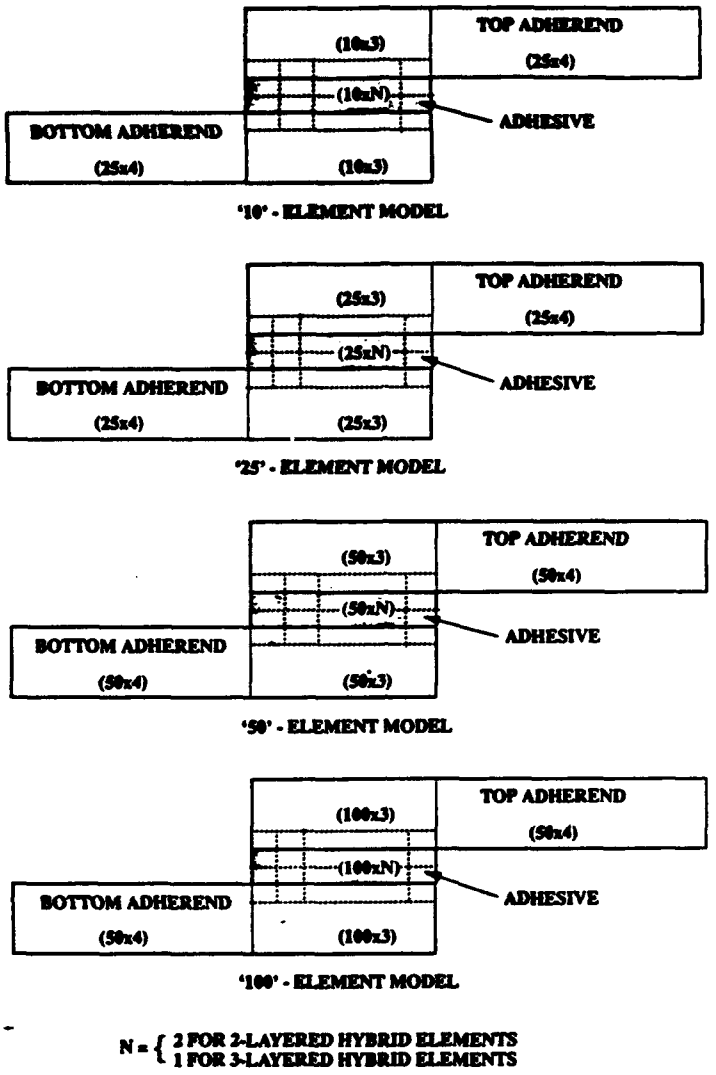

Figure 10. Discretization used in the 2-D models to assess solution convergence.

6.1 The H2L6N Element

The H2L6N element is formulated as a 6-node, two layer element as shown in Figure 11. This element is constructed specifically to provide a more accurate representation of stresses at material interfaces by explicitly enforcing stress continuity of the σ_{yy} and τ_{xy} stress components. In modelling the adhesive layer, two H2L6N elements are used through the adhesive thickness and are joined to displacement-based 4-node plane strain elements used to model the adherends. The use of the H2L6N element in modelling an adhesive layer is depicted in Figure 12. 4-node plane-strain displacement-based elements - designated CPE4 - were obtained from the ABAQUS element library and used to model the adherends.

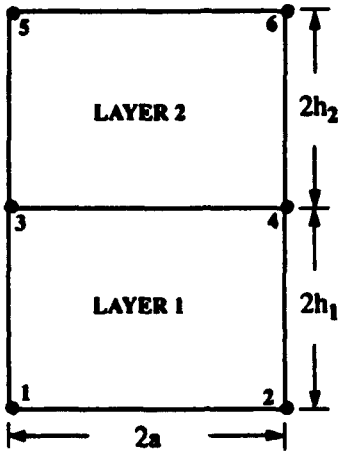

Figure 11. The H2L6N element.

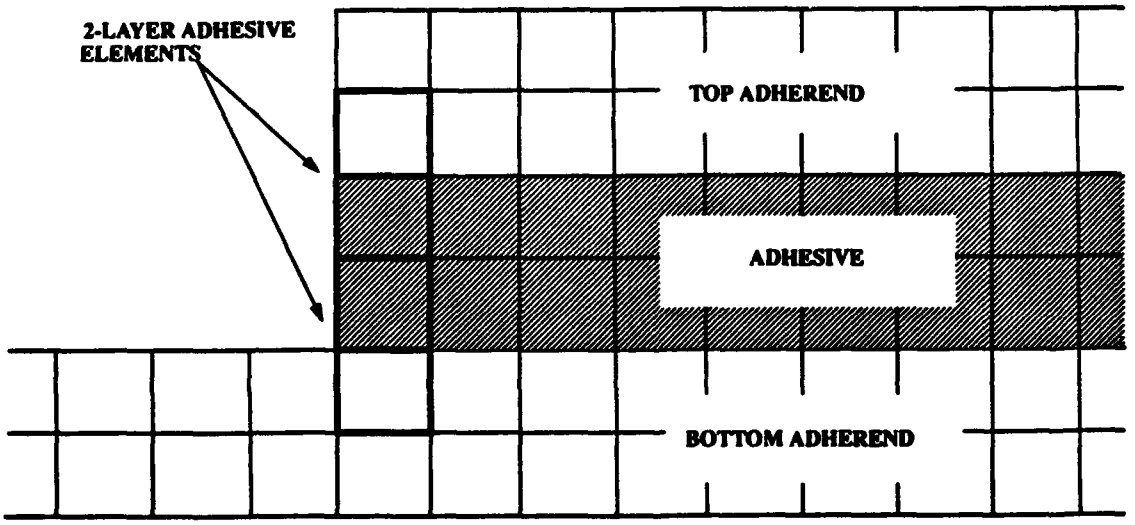

Figure 12. The use of special two-layer elements in modelling adhesive bonds.

Three versions of H2L6N were developed to assess the order of stress expansions on element performance. In all formulations field equilibrium is enforced *a priori* together with the interface continuity conditions. The number of independent strain modes, n_ϵ, may be computed as

$$n_\epsilon = n_{dof} - n_{rbm} \tag{40}$$

where n_{dof} are the number of element degrees of freedom and n_{rbm} are the number of rigid body modes. For the H2L6N element, the bilinear isoparametric displacement field yields $n_\epsilon = 12 - 3$ or 9 independent strain modes. Version I incorporates complete linear expansions for each layer resulting in a stress field possessing 10 independent stress modes which is sufficient to suppress any zero energy modes in the resultant element stiffness matrix. The stress expansions are given by:

$$\begin{aligned}
\sigma^1_{xx} &= \beta_1 + \beta_2 x + \beta_3 y \\
\sigma^1_{yy} &= \beta_4 + \beta_5 x - \beta_7 y \\
\tau^1_{xy} &= \beta_6 + \beta_7 x - \beta_2 y \\
\sigma^2_{xx} &= \beta_8 + \beta_9 x + \beta_{10} y \\
\sigma^2_{yy} &= \beta_4 + \beta_5 x - \beta_7 (h_1 + h_2 + y) \\
\tau^2_{xy} &= \beta_6 - h_1 \beta_2 + \beta_7 x - \beta_9 (h_2 + y)
\end{aligned} \tag{41}$$

Version II incorporates complete quadratic expansions for the assumed stresses yielding 18 independent stress modes given by

$$\begin{aligned}
\sigma^1_{xx} &= \beta_1 - \beta_2 x + \beta_3 y - 2\beta_4 xy - \beta_5 x^2/2 + \beta_6 y^2 \\
\sigma^1_{yy} &= \beta_7 + 2\beta_8[(h_1 + h_2)x - xy] + \beta_9 x + \beta_5 y(h_1 - y/2) - \beta_{10} y + \beta_{11} h_2 y + \beta_{12} x^2 \\
\tau^1_{xy} &= \beta_{13} + \beta_5 x(y - h_1) + \beta_{10} x - \beta_{11} h_2 x + \beta_2 y + \beta_8 x^2 + \beta_4 y^2 \\
\sigma^2_{xx} &= \beta_{14} - \beta_{15} x + \beta_6 y - 2\beta_{17} xy - \beta_{11} x^2/2 + \beta_8 y^2 \\
\sigma^2_{yy} &= \beta_7 + \beta_5 h_1^2/2 - \beta_{10}(h_1 + h_2 + y) + \beta_{11}[h_1 h_2 + (h_2^2 - y^2)/2] + \beta_9 x - 2\beta_8 xy + \beta_{12} x^2 \\
\tau^2_{xy} &= \beta_{13} + \beta_2 h_1 + \beta_4 h_1^2 + \beta_{15}(h_2 + y) + \beta_{17}(y^2 - h_2^2) + \beta_{10} x + \beta_{11} xy + \beta_8 x^2
\end{aligned} \tag{42}$$

Version III incorporates complete cubic expansions for the assumed stresses with 28 independent modes given by

$$\begin{aligned}
\sigma^1_{xx} &= \beta_1 - x\beta_2 + y\beta_3 - 2xy\beta_4 - x^2\beta_5/2 + y^2\beta_6 - 3xy^2\beta_7 - yx^2\beta_8 - x^3\beta_9/3 + y^3\beta_{10} \\
\sigma^1_{yy} &= (-h_1^2/2 + h_1 y - y^2/2)\beta_5 + (h_1^2 y - 2h_1^3/3 - y^3/3)\beta_8 + (h_1 + h_2 - y)\beta_{13} + \beta_{12} + \\
&\quad h_2(y - h_1 - h_2/2)\beta_{14} + h_2^2(h_1 + h_2/3 - y)\beta_{15} + x(2h_1 y - h_1^2 - y^2)\beta_9 + x\beta_{16} + \\
&\quad 2x(h_1 + h_2 - y)\beta_{17} + xh_2(2y - 2h_1 - h_2)\beta_{18} + 3x^2(h_1 + h_2 - y)\beta_{19} + x^2\beta_{11} + x^3\beta_{20} \\
\tau^1_{xy} &= (y - h_1)\beta_2 + (y^2 - h_1^2)\beta_4 + (y^3 - h_1^3)\beta_7 + \beta_{21} - h_2\beta_{22} + h_2^2\beta_{23} - h_2^3\beta_{24} + x(y - h_1)\beta_5 + \\
&\quad x(y^2 - h_1^2)\beta_8 + x\beta_{13} - h_2 x\beta_{14} + h_2^2 x\beta_{15} + x^2(y - h_1)\beta_9 + x^2\beta_{17} - h_2 x^2\beta_{18} + x^3\beta_{19} \\
\sigma^2_{xx} &= \beta_{25} - x\beta_{22} + y\beta_{26} - 2xy\beta_{23} - x^2\beta_{14}/2 + y^2\beta_{27} - 3xy^2\beta_{24} - yx^2\beta_{15} - x^3\beta_{18}/3 + y^3\beta_{28} \\
\sigma^2_{yy} &= \beta_{12} + x\beta_{16} - y\beta_{13} - 2xy\beta_{17} + x^2\beta_{11} - y^2/2\beta_{14} - xy^2\beta_{18} - 3yx^2\beta_{19} + x^3\beta_{20} - y^3\beta_{15}/3 \\
\tau^2_{xy} &= \beta_{21} + x\beta_{13} + y\beta_{22} + xy\beta_{14} + x^2\beta_{17} + y^2\beta_{23} + xy^2\beta_{15} + yx^2\beta_{18} + x^3\beta_{19} + y^3\beta_{24}
\end{aligned} \tag{43}$$

The element behavior in the prediction of σ_{yy} and τ_{xy} stresses utilizing the various complete orders of assumed stress expansions are depicted below. The four basic models using 10, 25, 50 and 100 H2L6N elements along the bondline are compared with the reference solution to assess convergence characteristics.

Figures 13 and 14 show the distribution of σ_y and τ_{xy} stresses across the bondline using the H2L6N element incorporating linear stress expansions. Rapid convergence to the reference solution is observed for all but the highly coarse 10-element model.

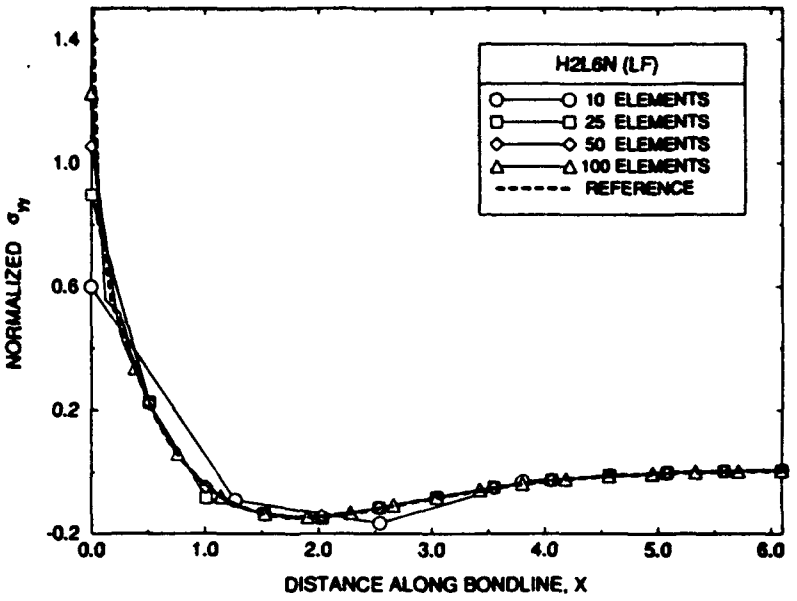

Figure 13. H2L6N Version I prediction of σ_{yy} stresses along the bondline.

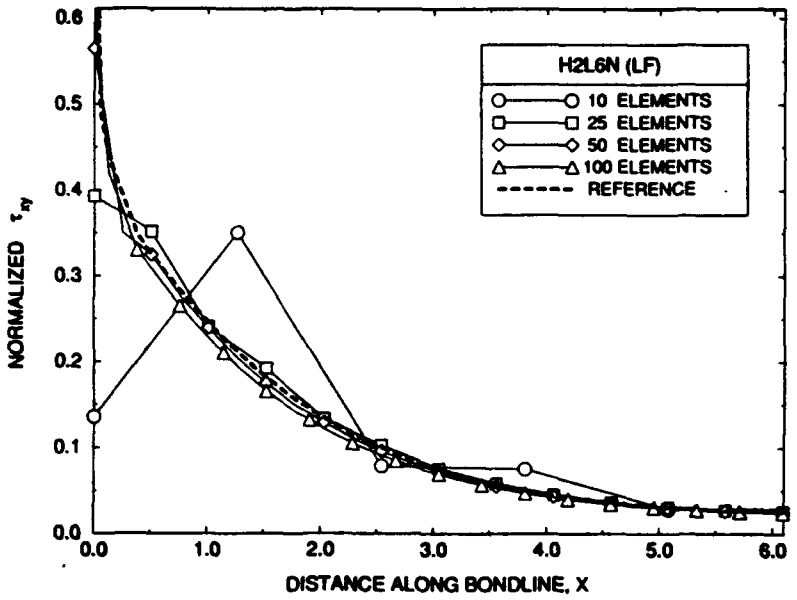

Figure 14. H2L6N Version I prediction of τ_{xy} stresses along the bondline.

Figures 15 and 16 show the distribution of σ_{yy} and τ_{xy} stresses across the bondline using the H2L6N element incorporating complete quadratic stress expansions.

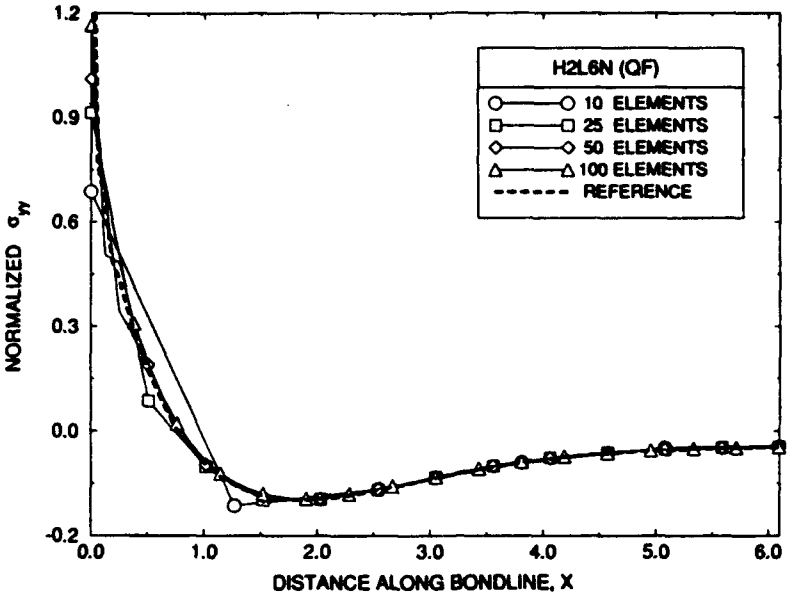

Figure 15. H2L6N Version II predictions of σ_{yy} stresses along the bondline.

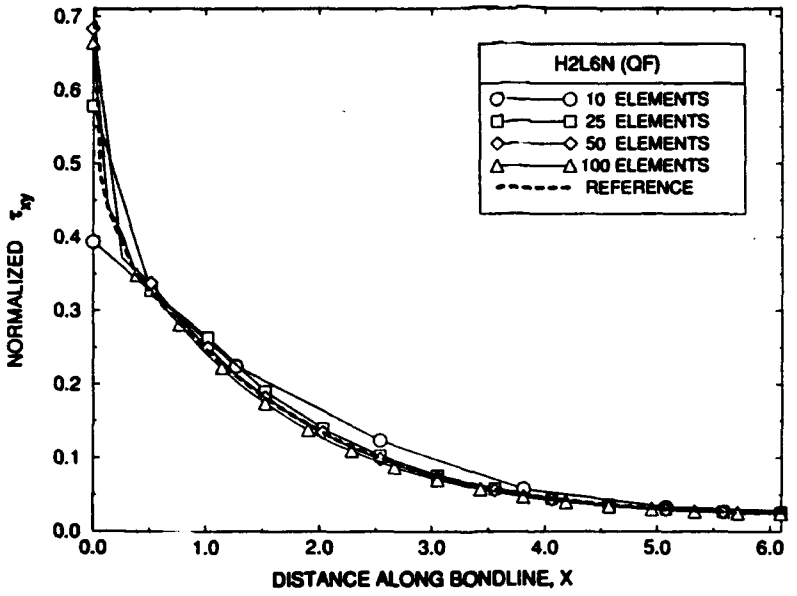

Figure 16. H2L6N Version II prediction of τ_{xy} stresses along the bondline.

Rapid convergence to the reference solution is again observed with improved convergence behavior demonstrated in the coarse mesh 10-element model.

Figures 17 and 18 show the distribution of σ_{yy} and τ_{xy} stresses across the bondline using the H2L6N element incorporating complete cubic stress expansions.

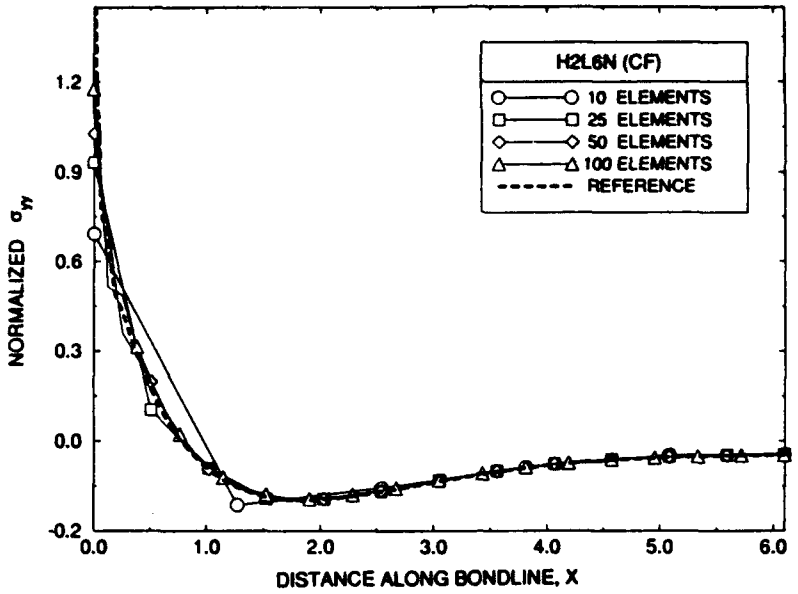

Figure 17. H2L6N Version III predictions of σ_{yy} stresses along the bondline.

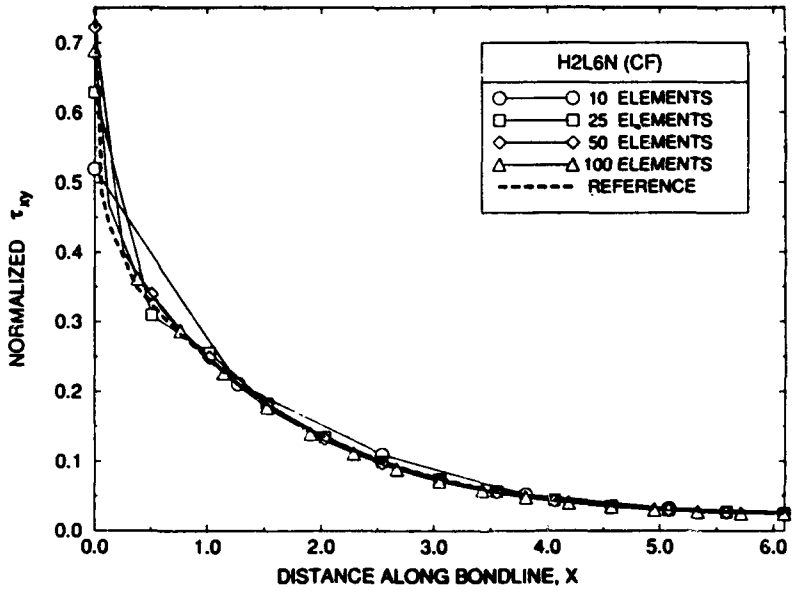

Figure 18. H2L6N Version III prediction of τ_{xy} stresses along the bondline.

Comparisons of the various models show that all element formulations yield excellent predictions for both the normal and shear stress distributions. The cubic order expansions used in version III provide little improvement over the quadratic fields incorporated in version II which indicates the diminishing return in adopting stress fields of increasingly higher order. Also demonstrated is the improvement in the coarse 10-element model with increasing order of assumed expansions for stresses.

In order to quantify the improvement in the coarse-mesh element behavior in the 10-element model, a comparison of the eigenvalues of the hybrid element stiffness matrices using complete linear, quadratic and cubic stress expansions is performed using the element geometry shown in Figure 19. A comparison is also made to a displacement-based formulation in which two separate 4-node elements where locally assembled to compare with the layered hybrid elements. The element geometry is selected to show the effect of a high aspect ratio layer which may be encountered in representing the adherend/ adhesive layers in a coarse model. The material properties used were $E = 1000$ and $\mu = 0.25$ and the joint width was taken as unity. The results depicted in Table 1 show that by adopting a higher-order stress representation, 'weak' deformation modes present in the linear field element are removed which can be related to the improvement in coarse-mesh behavior.

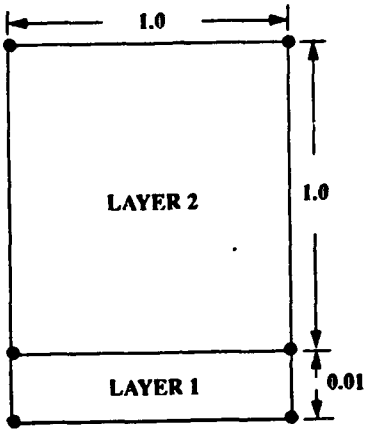

Figure 19. Sample configuration of H2L6N containing a high aspect ratio layer.

Table 1. Comparison of eigenvalues obtained in the H2L6N element incorporating complete linear, quadratic and cubic stress expansions with a displacement-based element.

λ	Linear expansions	Quadratic Expansions	Cubic Expansions	Displacement-based
1	0.0	0.0	0.0	0.0
2	0.0	0.0	0.0	0.0
3	0.0	0.0	0.0	0.0
4	2.389470	59.08495	167.7284	324.0885
5	6.608349	218.5657	257.2027	346.4270
6	250.7947	428.2339	469.4921	644.1404
7	355.4981	464.6144	545.8709	651.8773
8	536.3158	713.2400	853.5973	1219.328
9	642.8778	892.4405	1039.350	13791.84
10	905.2318	930.4139	1125.610	40050.97
11	1233.321	1961.596	2418.629	40289.39
12	1924.831	2324.951	2675.814	120303.3

The conclusion from the above study is that the minimum stress expansion used in version I is adequate to suppress zero energy modes yet is deficient as compared to higher orders of stress expansions in terms of

coarse mesh accuracy. The reason for the significant change in element characteristics with increasing order of assumed stress fields is due to the constraints imposed in formulating a layered element. These conditions constrain the element stress field such that the inner product of assumed functions comprising the stress space with those defining the strain space is highly dependent on the order of stress expansions used. The increase in the spanning of the strain space is measured by the eigencharacteristics of the resulting element stiffness matrices and represents the elastic strain energy associated with particular element deformation modes. Another observation is that the extremely 'stiff' deformation modes evidenced in the displacement-based 'layered' element formulation due to the high aspect ratio of the bottom element layer is not present in the hybrid element formulations. The comparison of element performance based on complete quadratic and cubic stress field expansions - versions II and III - show negligible difference indicating that the quadratic stress field is optimum for this element configuration.

To compare the H2L6N element predictions with conventional finite elements, figures 20 and 21 show results using standard displacement-based elements. The elements used are the CPE4 plane-strain quadrilaterals available in the ABAQUS library. In the displacement-based model, two 4-node plane strain elements were used to model the adhesive layer through the thickness utilizing the same number of degrees of freedom as in the layered hybrid elements. Because the displacement-based solution is incapable of representing continuity of stress components across the interface, stresses were extrapolated from Gauss points and averaged at nodes for all connected elements. As shown, the solution for bond interface stresses actually converges away from the reference solution with increasing mesh refinement along the bond line. The improvement in stress prediction using the layered hybrid stress approach is related to the ability of explicitly imposing the stress continuity conditions at the interface and equilibrium constraints with each layer domain.

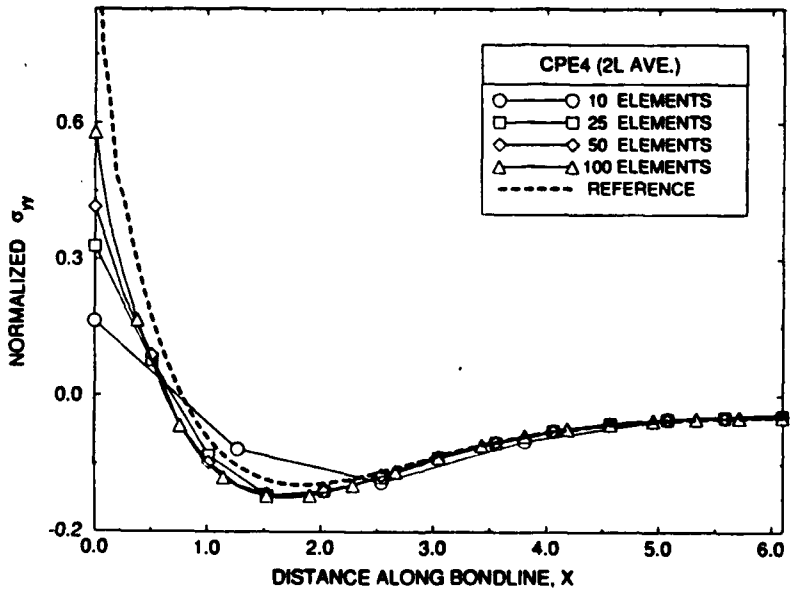

Figure 20. CPE4 prediction of σ_{yy} stress distribution along the bondline.

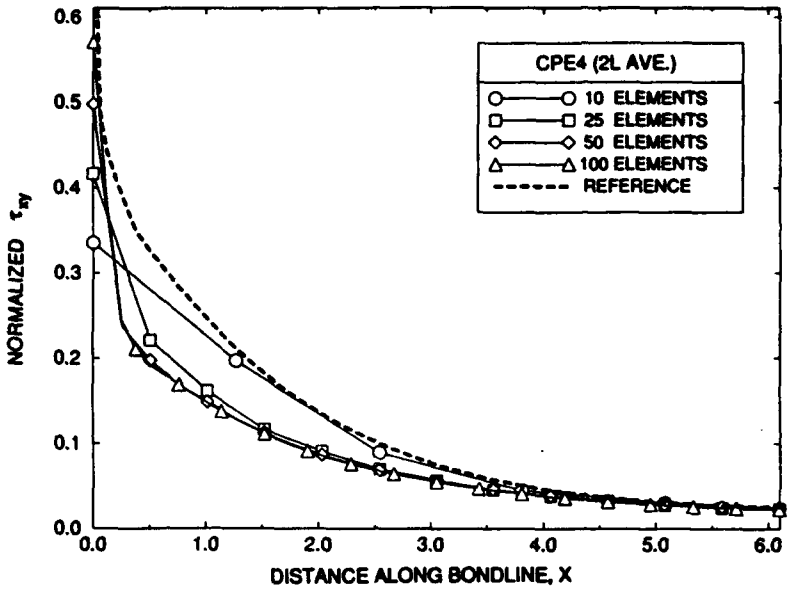

Figure 21. CPE4 prediction of τ_{xy} stress distribution along the bondline.

Stress recovery at points away from the critical bond interface region show a closer agreement between the hybrid and displacement-based elements. Figures 22 through 25 show stresses recovered at element centroids and indicates that the special layered adhesive elements and displacement-based elements converge to the same solution within material domains while the hybrid elements demonstrate greater efficiency and accuracy in stress prediction along critical domain boundaries where material properties are discontinuous such as along the adhesive/adherend interface.

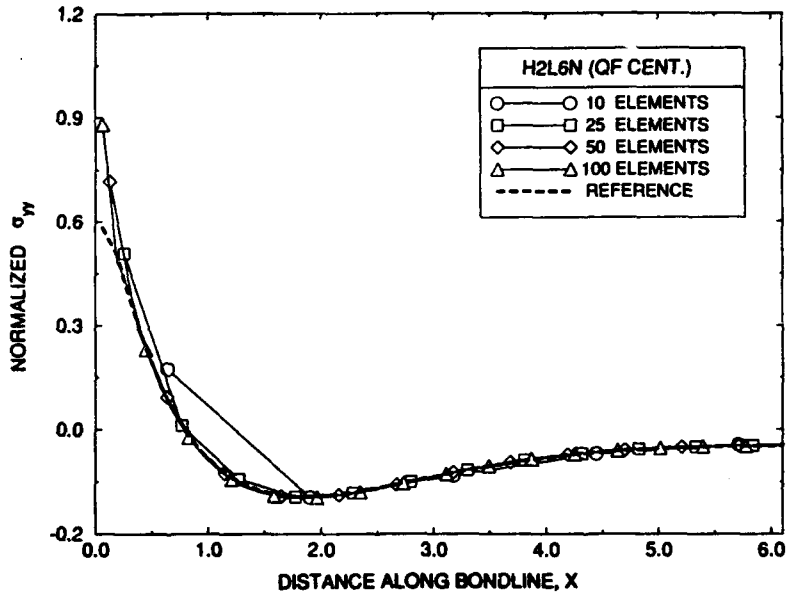

Figure 22. H2L6N prediction of σ_{yy} stress distribution computed at element centroid.

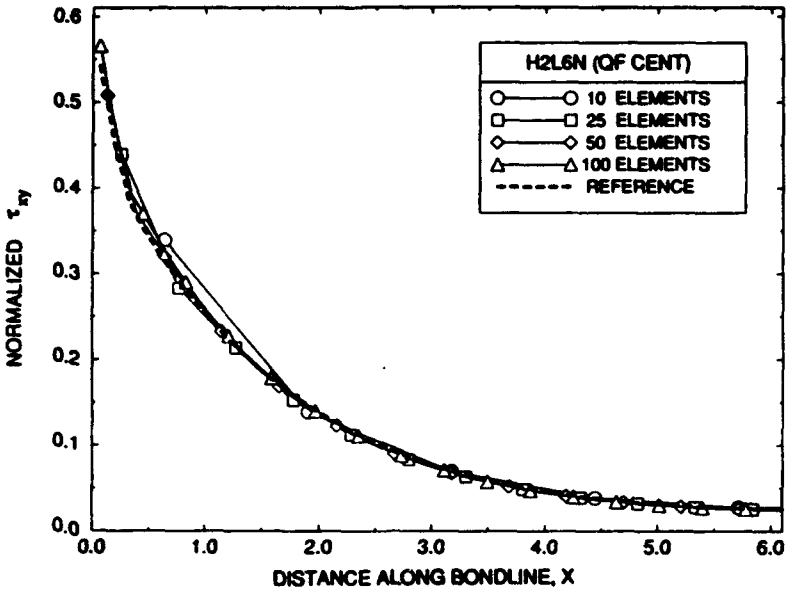

Figure 23. H2L6N prediction of τ_{xy} stress distribution computed at element centroid.

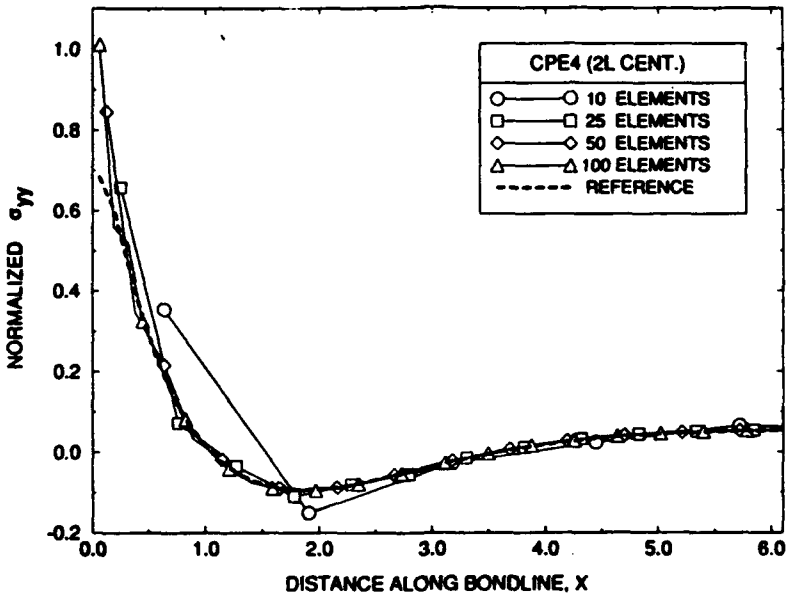

Figure 24. CPE4 prediction of σ_{yy} stress distribution computed at element centroid.

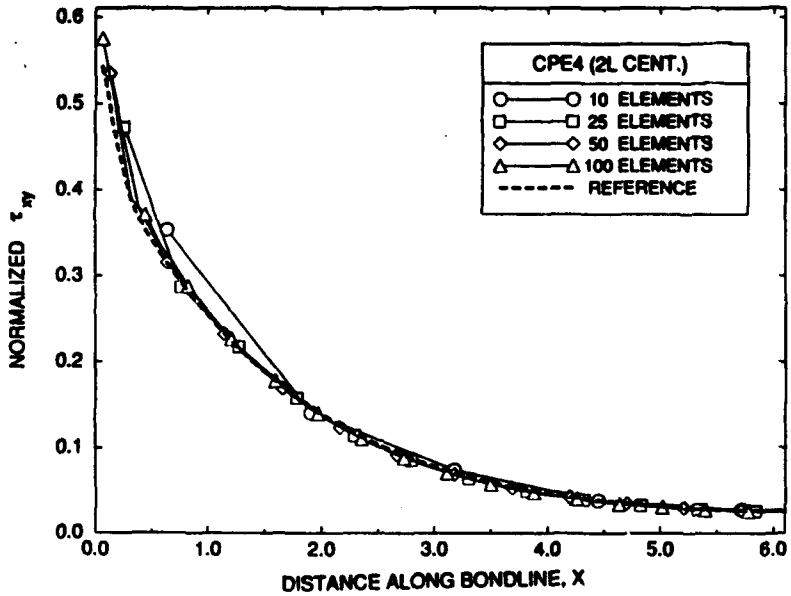

Figure 25. CPE4 prediction of τ_{xy} stress distribution computed at element centroid.

In the hybrid stress method, a limitation principle exists in which, for elements with rectangular geometry, the element stiffness coefficients become identical to those obtained from a purely displacement-based approach if no constraints are imposed on the assumed stress fields. An examination was, therefore, undertaken to qualify the improvement in hybrid element performance over displacement-based elements by assessing the the relative effect of selectively enforcing layer equilibrium and interface continuity conditions in element formulations. Figures 26 and 27 show the prediction of σ_{yy} and τ_{xy} stresses along the bondline using complete quadratic stress field expansions in which only field equilibrium constraints were enforced in each layer. The resulting stress field contains 24 independent stress modes given by

$$
\begin{aligned}
\sigma^1_{xx} &= \beta_1 + x\beta_2 + y\beta_3 + xy\beta_4 + x^2\beta_5/2 + y^2\beta_6 \\
\sigma^1_{yy} &= \beta_7 + x\beta_8 + y\beta_9 + xy\beta_{10} + x^2\beta_{11} - y^2\beta_5/2 \\
\tau^1_{xy} &= \beta_{12} - x\beta_9 - y\beta_2 + xy\beta_5 - x^2\beta_{10} - y^2\beta_2 \\
\sigma^2_{xx} &= \beta_{13} + x\beta_{14} + y\beta_{15} + xy\beta_{16} + x^2\beta_{17}/2 + y^2\beta_{18} \\
\sigma^2_{yy} &= \beta_{19} + x\beta_{20} + y\beta_{21} + xy\beta_{22} + x^2\beta_{23} - y^2\beta_{17}/2 \\
\tau^2_{xy} &= \beta_{24} - x\beta_{21} - y\beta_{14} + xy\beta_{17} - x^2\beta_{22} - y^2\beta_{14}
\end{aligned}
\tag{44}
$$

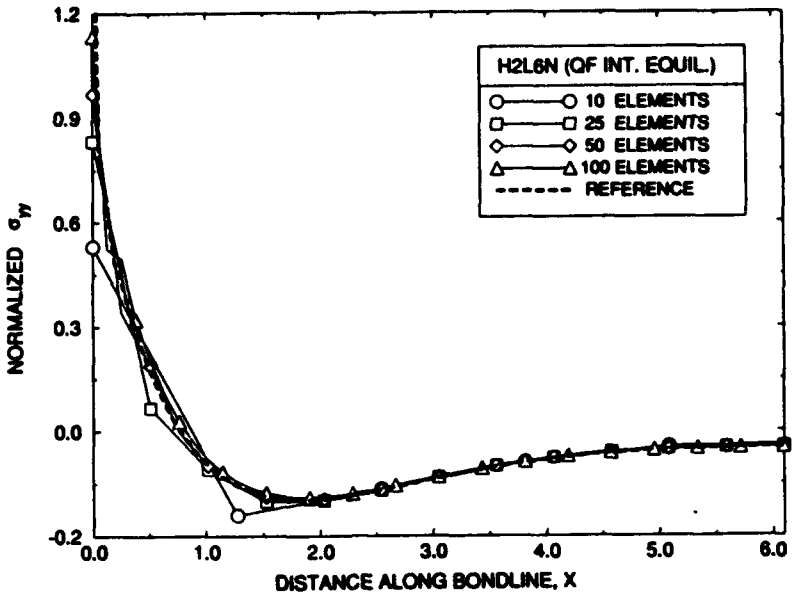

Figure 26. H2L6N σ_{yy} bondline stress prediction with only equilibrium constraints enforced.

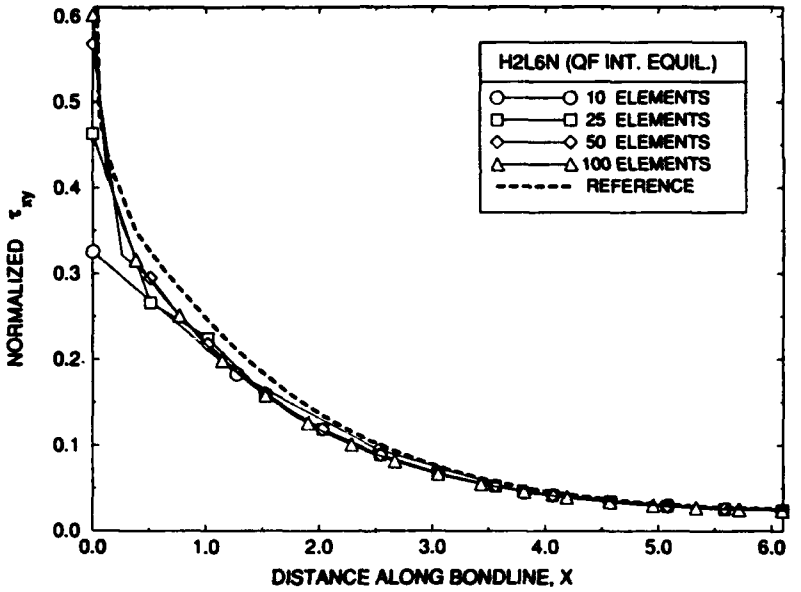

Figure 27. H2L6N τ_{xy} bondline stress prediction with only equilibrium constraints enforced.

As shown, the normal peel stresses, σ_{yy}, are accurately predicted while the shear stress distribution shows a convergence away from the reference solution. Although not as pronounced as in the use of CPE4 elements, this departure from the reference solution demonstrates the importance of enforcing the continuity conditions at the layer interface and qualifies the improved accuracy obtained in the hybrid stresss technique over displacement-based formulations when equilibrium is enforced pointwise.

Figures 28 and 29 show the stress prediction of the H2L6N element in which complete quadratic stress fields were constrained only to satisfy interface continuity conditions. The resulting stress field contains 30

independent stress modes given by

$$
\begin{aligned}
\sigma^1_{xx} &= \beta_6 + y^2\beta_1 + x^2\beta_2 + xy\beta_3 + y\beta_4 + x\beta_5 \\
\sigma^1_{yy} &= \beta_9 + x(y - h_1)\beta_7 + y\beta_8 + x^2\beta_{10} - xh_2\beta_{11} + x\beta_{12} + y^2\beta_{13} \\
\tau^1_{xy} &= \beta_{19} + y^2\beta_{14} + xy\beta_{15} + x^2\beta_{16} + y\beta_{17} + x\beta_{18} \\
\sigma^2_{xx} &= \beta_{20} + y^2\beta_{21} + x^2\beta_{22} + xy\beta_{23} + y\beta_{24} + x\beta_{25} \\
\sigma^2_{yy} &= \beta_9 + (y^2 - h_2^2)\beta_{26} + (h_2 + y)\beta_{27} + h_1\beta_8 + x^2\beta_{10} + xy\beta_{11} + x\beta_{12} + h_1^2\beta_{13} \\
\tau^2_{xy} &= \beta_{19} + (y^2 - h_2^2)\beta_{28} + x(y + h_2)\beta_{29} + (h_2 + y)\beta_{30} + h_1^2\beta_{14} + h_1x\beta_{15} + x^2\beta_{16} + h_1\beta_{17} + x\beta_{18}
\end{aligned}
\tag{45}
$$

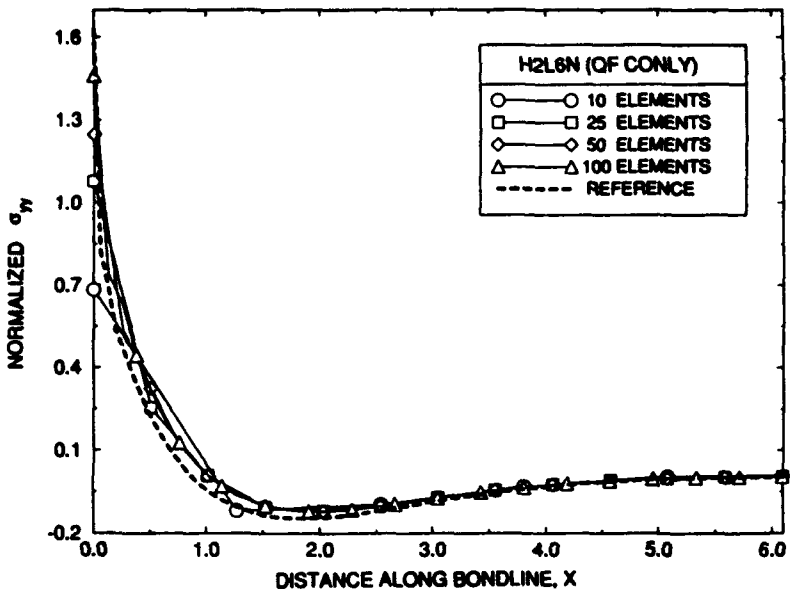

Figure 28. H2L6N σ_{yy} bondline stress prediction with only interface constraints enforced.

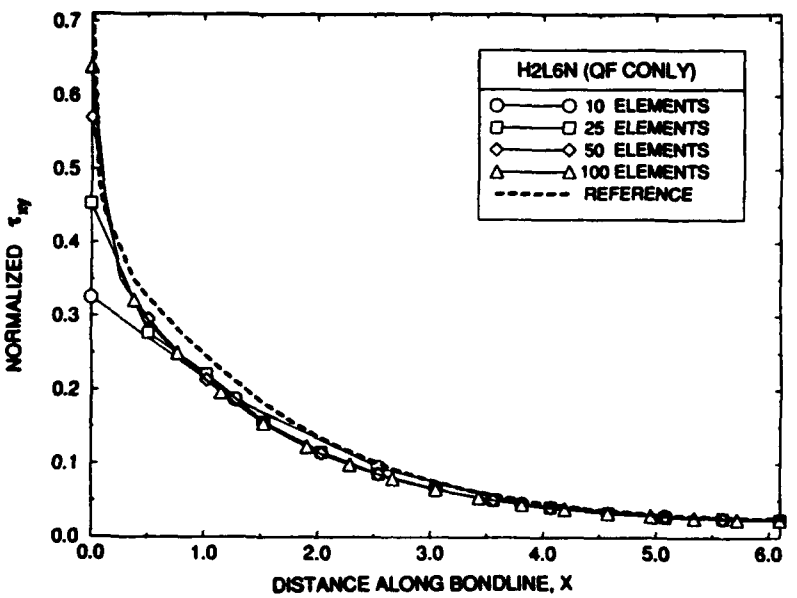

Figure 29. H2L6N τ_{xy} bondline stress prediction with only interface constraints enforced.

As shown, both the normal stress and the shear stress distribution is shown to converge away from the

reference solution. The conclusion from the above results indicate that the imposition of both layer equilibrium and interface stress continuity constraints is necessary for obtaining optimal element performance in predicting bondline stresses.

The partial hybrid stress approach is next employed to assess the effect of fully enforcing interface continuity of stress components while incorporating only partial satisfaction of the layer domain equilibrium conditions. Two stress fields were developed for σ_{yy} and τ_{xy} based on different orders of complete stress expansion. The normal stress component, σ_{zz}, was calculated from the assumed displacement field. Linear stress expansions are sufficient to suppress any spurious kinematic modes and the resulting stress field contains 6 independent modes given by

$$\begin{aligned}
\sigma^1_{yy} &= \beta_2 + (h_1 + h_2 - y)\beta_1 + x\beta_3 \\
\tau^1_{xy} &= \beta_5 + (y - h_1)\beta_4 - h_2\beta_6 + x\beta_1 \\
\sigma^2_{yy} &= \beta_2 + x\beta_3 - y\beta_1 \\
\tau^2_{xy} &= \beta_5 + x\beta_1 + y\beta_6
\end{aligned} \tag{46}$$

Complete quadratic expansions were also developed containing 12 independent stress modes given by

$$\begin{aligned}
\sigma^1_{yy} &= \beta_4 + (h_1^2 - 2h_1 y + y^2)\beta_1 + (y - h_1 - h_2)\beta_2 + h_2(2h_1 + h_2 - 2y)\beta_3 + \\
&\quad x\beta_5 + 2x(h_1 + h_2 - y)\beta_6 + x^2\beta_7 \\
\tau^1_{xy} &= \beta_{10} + (y - h_1)\beta_8 + (y^2 - h_1^2)\beta_9 - h_2\beta_{11} + h_2^2\beta_{12} + \\
&\quad 2x(h_1 - y)\beta_1 - x\beta_2 + 2h_2 x\beta_3 + x^2\beta_6 \\
\sigma^2_{yy} &= \beta_4 + x\beta_5 + y\beta_2 - 2xy\beta_6 + x^2\beta_7 + y^2\beta_3 \\
\tau^2_{xy} &= \beta_{10} - x\beta_2 + y\beta_{11} - 2xy\beta_3 + x^2\beta_6 + y^2\beta_{12}
\end{aligned} \tag{47}$$

Figures 30 through 33 depict stress predictions using the complete linear and quadratic stress fields for the two independent stress components σ_{yy} and τ_{xy} as presented above.

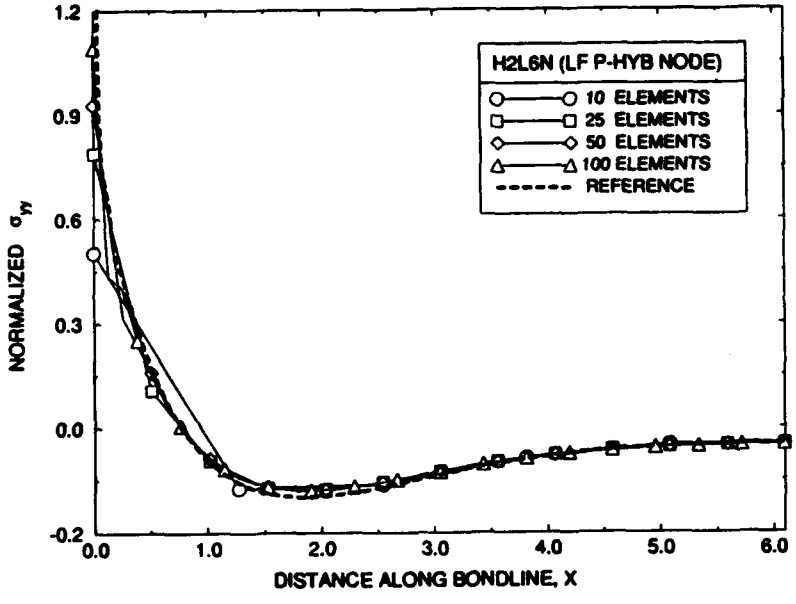

Figure 30. H2L6N σ_{yy} bondline distribution using partial hybrid stress formulation with linear stress fields.

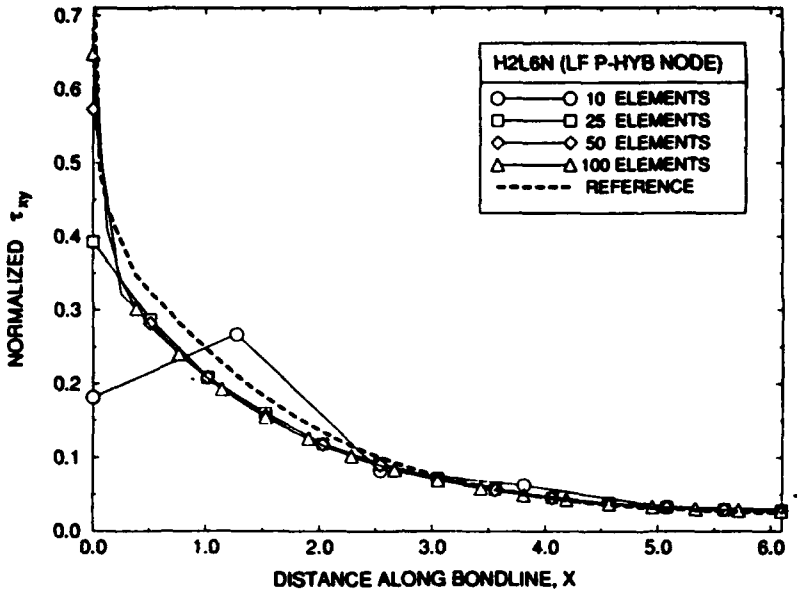

Figure 31. H2L6N τ_{xy} bondline distribution using partial hybrid stress formulation with linear stress fields.

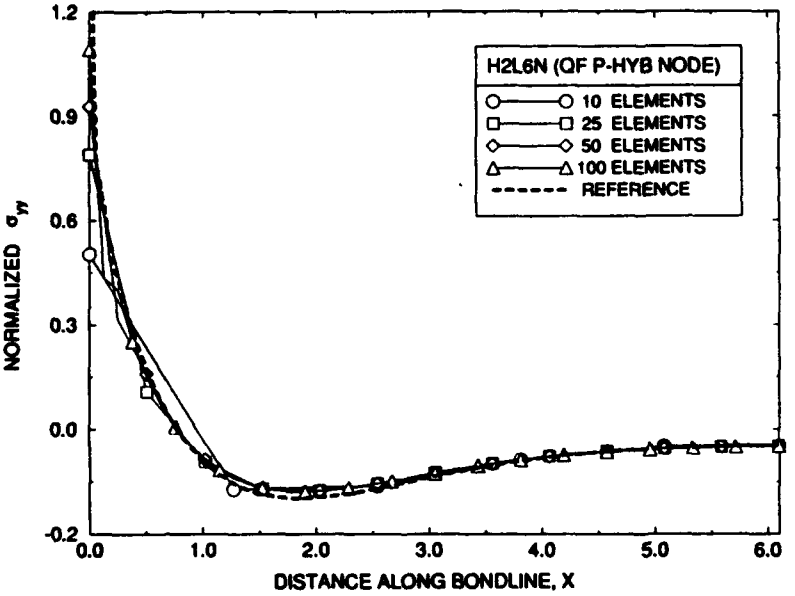

Figure 32. H2L6N σ_{yy} bondline distribution using partial hybrid stress formulation with quadratic stress fields.

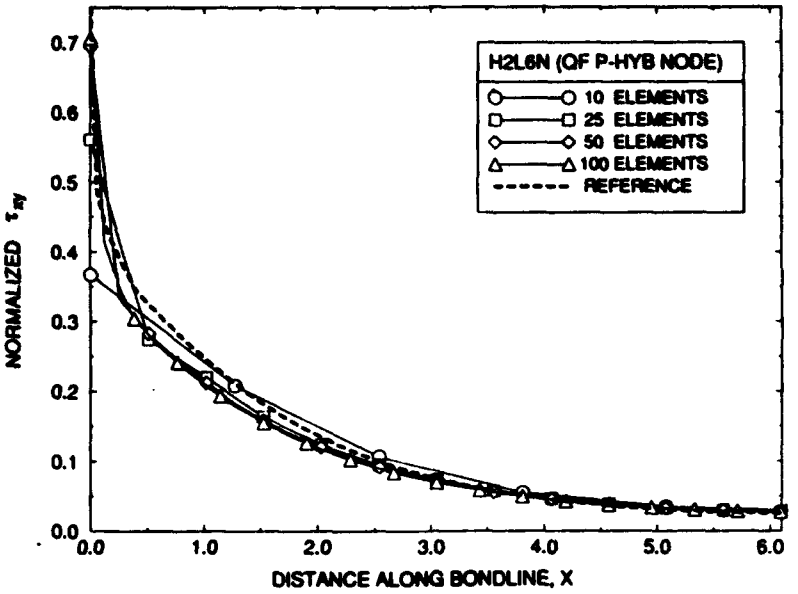

Figure 33. H2L6N τ_{xy} bondline distribution using partial hybrid stress formulation with quadratic stress fields.

From the above distributions it is evident that the normal stress distribution is predicted with good accuracy. The results for the shear stress distribution converge away from the reference solution indicating the deficiency of the partial stress method in accurately predicting all independent stress components. The increase in the order of expansions from linear to quadratic again demonstrate the improvement in coarse mesh accuracy as shown by the behavior of the 10-element model.

In an actual bonded joint, the ends of the adhesive layer are traction free. Using conventional finite element models gives rise to the prediction of nonzero shear and inplane tractions in this region. In the hybrid stress method, the ability to strictly enforce zero traction conditions of the τ_{xy} and σ_{xx} components at the free edge is obtained through *a priori* imposing the following constaints in the assumed stress field

$$\tau^i_{xy}|_{x=-a,a} = 0 \;\; ; \;\; \sigma^i_{xx}|_{x=-a,a} = 0 \tag{48}$$

where a is the element half-width. Four versions of an assumed quadratic stress field in which zero traction is specified along a particular face as depicted in Figure 34 are developed. The full hybrid variational basis is utilized in the element formulation. All stress fields possess 15 independent stress modes resulting in 'end' elements of correct rank.

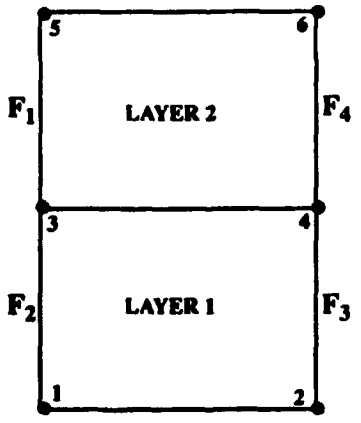

Figure 34. H2L6N element showing side designations on which zero traction conditions are explicitly enforced.

The resulting stress field expansions in which zero traction conditions are enforced on various element sides are given below.

For zero traction on element side F1:

$$\begin{aligned}
\sigma^1_{xx} &= \beta_1 - x\beta_2 + y\beta_3 - 2xy\beta_4 - x^2\beta_5/2 + y^2\beta_6 \\
\sigma^1_{yy} &= \beta_8 + (-h_1^2 + 2h_1 y - y^2)\beta_5/2 + (y - h_1 - h_2)\beta_7 + h_2(y - h_1)\beta_9 + \\
&\quad 2x(h_1 - y)\beta_{10} + x\beta_{11} - h_2 x\beta_{12} + x^2\beta_{13} \\
\tau^1_{xy} &= (y - h_1)\beta_2 + (y^2 - h_1^2)\beta_4 - (a + x)\beta_7 + (x^2 - a^2)\beta_{10} - \\
&\quad h_2(a + x)\beta_9 + x(y - h_1)\beta_5 \\
\sigma^2_{xx} &= -a(x + a)\beta_9 + (x^2 - a^2)\beta_{14} + y(x + a)\beta_{15} \\
\sigma^2_{yy} &= \beta_8 + x\beta_{11} + y\beta_7 + xy\beta_{12} + x^2\beta_{13} \\
\tau^2_{xy} &= -(x + a)\beta_7 + (x^2 - a^2)\beta_{10} + y(x + a)\beta_9
\end{aligned} \tag{49}$$

For zero traction on element side F2:

$$\begin{aligned}
\sigma^1_{xx} &= -a(x + a)\beta_9 + (x^2 - a^2)\beta_{14} + y(x + a)\beta_{15} \\
\sigma^1_{yy} &= \beta_8 + x\beta_{11} + y\beta_7 + xy\beta_{12} + x^2\beta_{13} \\
\tau^1_{xy} &= -(x + a)\beta_7 + (x^2 - a^2)\beta_{10} + y(x + a)\beta_9 \\
\sigma^2_{xx} &= \beta_1 - x\beta_2 + y\beta_3 - 2xy\beta_4 - x^2\beta_5/2 + y^2\beta_6 \\
\sigma^2_{yy} &= \beta_8 - (h_2^2 + 2h_2 y + y^2)\beta_5/2 + (h_1 + h_2 + y)\beta_7 - h_1(h_2 + y)\beta_9 - \\
&\quad 2x(h_2 + y)\beta_{10} + x\beta_{11} + h_1 x\beta_{12} + x^2\beta_{13} \\
\tau^2_{xy} &= (h_2 + y)\beta_2 + (y^2 - h_2^2)\beta_4 - (a + x)\beta_7 + (x^2 - a^2)\beta_{10} + \\
&\quad h_1(a + x)\beta_9 + x(h_2 + y)\beta_5
\end{aligned} \tag{50}$$

For zero traction on element side F3:

$$\begin{aligned}
\sigma^1_{xx} &= \beta_1 - x\beta_2 + y\beta_3 - 2xy\beta_4 - x^2\beta_5/2 + y^2\beta_6 \\
\sigma^1_{yy} &= \beta_8 - (h_2 - 2h_2 y + y^2)\beta_5/2 + (y - h_2 - h_2)\beta_7 + h_2(y - h_2)\beta_9 + \\
&\quad 2x(h_2 - y)\beta_{10} + x\beta_{11} - h_2 x\beta_{12} + x^2\beta_{13} \\
\tau^1_{xy} &= (y - h_1)\beta_2 + (y^2 - h_1^2)\beta_4 + (a - x)\beta_7 + (x^2 - a^2)\beta_{10} + \\
&\quad h_2(a - x)\beta_9 + x(-h_1 + y)\beta_5 \\
\sigma^2_{xx} &= a(x - a)\beta_9 + (x^2 - a^2)\beta_{14} + y(x - a)\beta_{15} \\
\sigma^2_{yy} &= \beta_8 + x\beta_{11} + y\beta_7 + xy\beta_{12} + x^2\beta_{13} \\
\tau^2_{xy} &= (a - x)\beta_7 + (x^2 - a^2)\beta_{10} + y(x - a)\beta_9
\end{aligned} \tag{51}$$

For zero traction on element side F4:

$$\begin{aligned}
\sigma^1_{xx} &= a(x - a)\beta_9 + (x^2 - a^2)\beta_{14} + y(x - a)\beta_{15} \\
\sigma^1_{yy} &= \beta_8 + x\beta_{11} + y\beta_7 + xy\beta_{12} + x^2\beta_{13} \\
\tau^1_{xy} &= (a - x)\beta_7 + (x^2 - a^2)\beta_{10} + y(x - a)\beta_9 \\
\sigma^2_{xx} &= \beta_1 - x\beta_2 + y\beta_3 - 2xy\beta_4 - x^2\beta_5/2 + y^2\beta_6 \\
\sigma^2_{yy} &= \beta_8 - (h_2^2 + 2h_2 y + y^2)\beta_5/2 + (h_1 + h_2 + y)\beta_7 + h_1(-h_2 - y)\beta_9 - \\
&\quad 2x(2h_2 + y)\beta_{10} + x\beta_{11} + h_1 x\beta_{12} + x^2\beta_{13} \\
\tau^2_{xy} &= (h_2 + y)\beta_2 + (y^2 - h_2^2)\beta_4 + (a - x)\beta_7 + (x^2 - a^2)\beta_{10} + \\
&\quad h_1(x - a)\beta_9 + x(h_2 + y)\beta_5
\end{aligned} \tag{52}$$

The resulting element behavior is demonstrated in Figures 35 and 36.

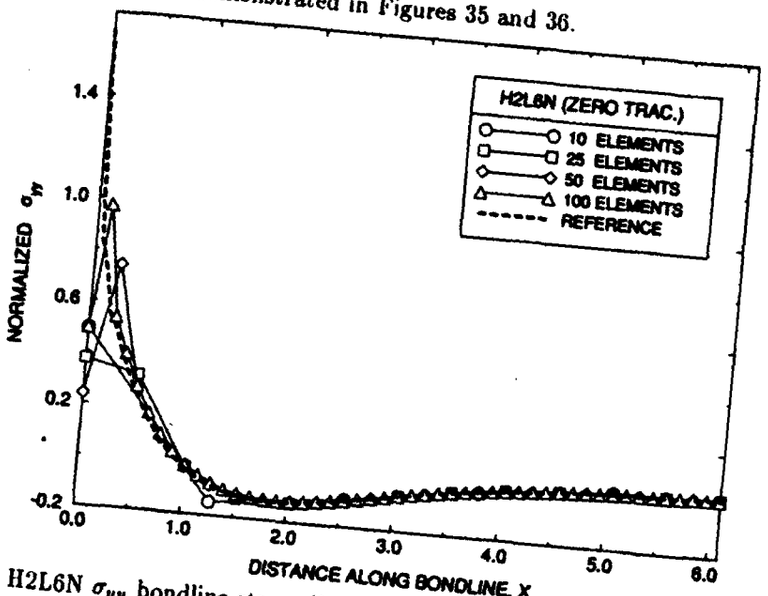

Figure 35. H2L6N σ_{yy} bondline stress distribution enforcing zero traction conditions at the bond end.

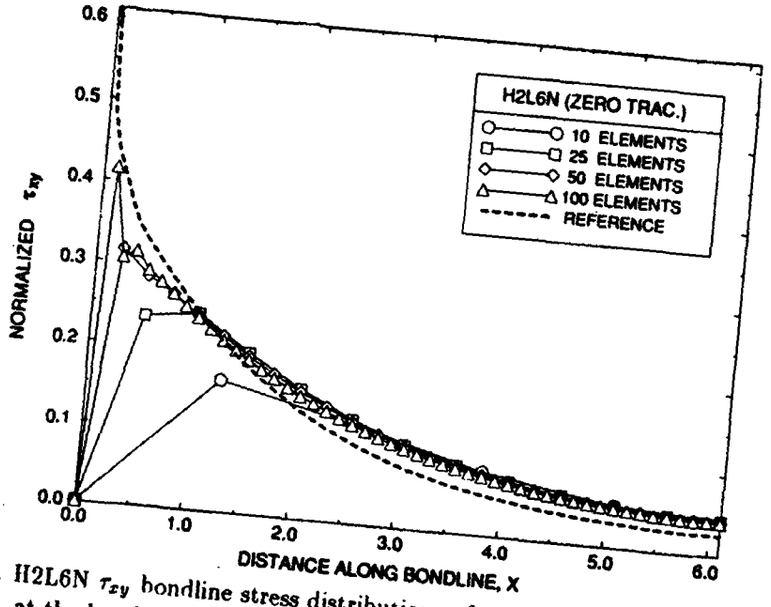

Figure 36. H2L6N τ_{xy} bondline stress distribution enforcing zero traction conditions at the bond end.

From the above predictions of stress distributions, two effects are demonstrated. First, the shear distribution is smoothed out somewhat due to the shear stress redistribution at the bond ends in order to maintain force equilibrium in the shear load transfer through the adhesive layer. Additionally, the singular behavior of the shear stress is not removed but is moved inward from the bond endpoint into the element layer domain. The normal stress distribution is significantly influenced by the zero traction condition imposed on the shear stresses through the equilibrium and continuity constraints. The singular nature of σ_{yy} appears to be diminished as the peak normal stresses show a convergent behavior in the region of the bond end. This

behavior is, however, regarded as a particular effect of the models being used in the present study; the singular nature of the normal stress solution is theoretically unaffected through the imposition of zero tractions of the shear stresses in linear elastic analysis.

6.2 The H2L10N Element

The H2L10N element is configured as a 2-layered element incorporating higher-order displacement fields in the bond thickness direction. The H2L10N element configuration is depicted in Figure 37. The interest in this element formulation is to assess the increase in the order of assumed displacement fields selectively in the direction of higher stress gradients. Two versions of this element were derived utilizing complete quadratic (version I) and complete cubic (version II) assumed stress fields. The assumed stress fields are identical to the quadratic and cubic expansions used in H2L6N and presented in equations (42) and (43). The behavior of these element formulations are presented in Figures 38 through 41.

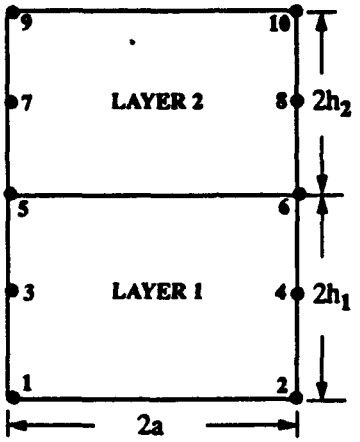

Figure 37. H2L10N element configuration.

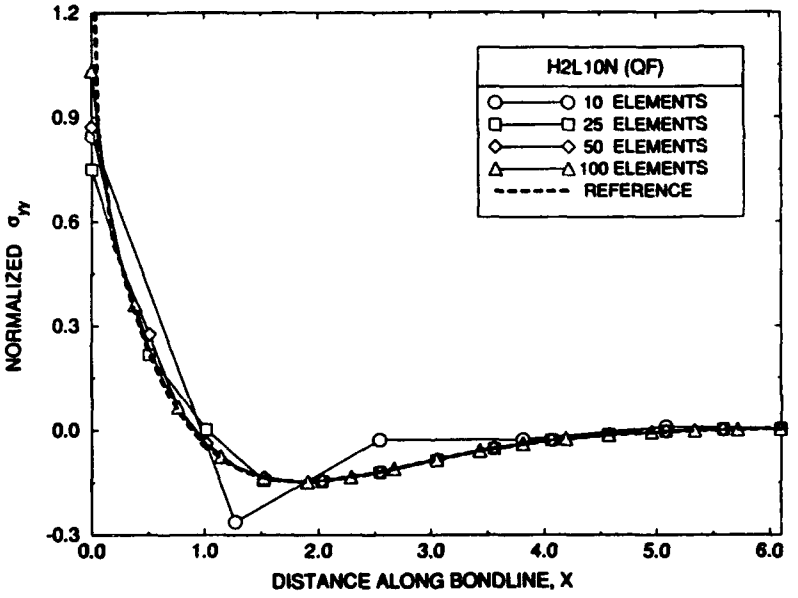

Figure 38. H2L10N Version I σ_{yy} stress distribution along the bondline.

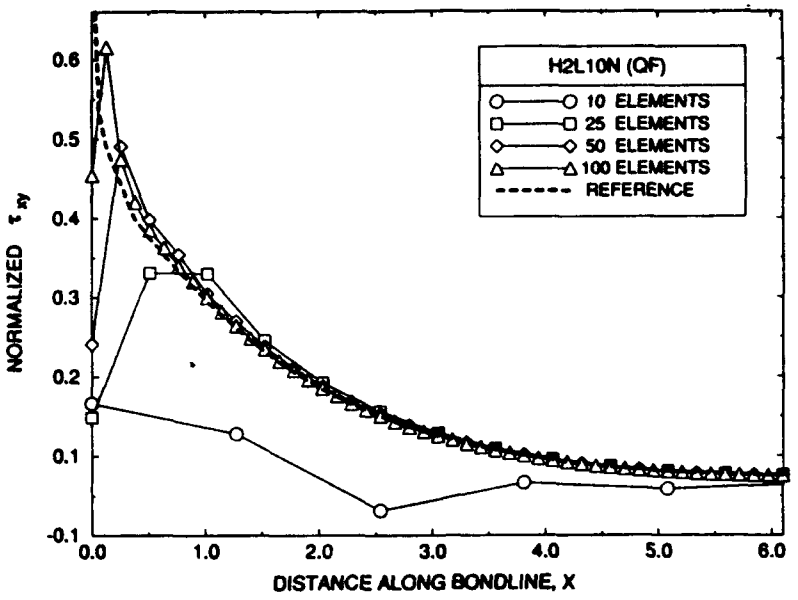

Figure 39. H2L10N Version I τ_{xy} stress distribution along the bondline.

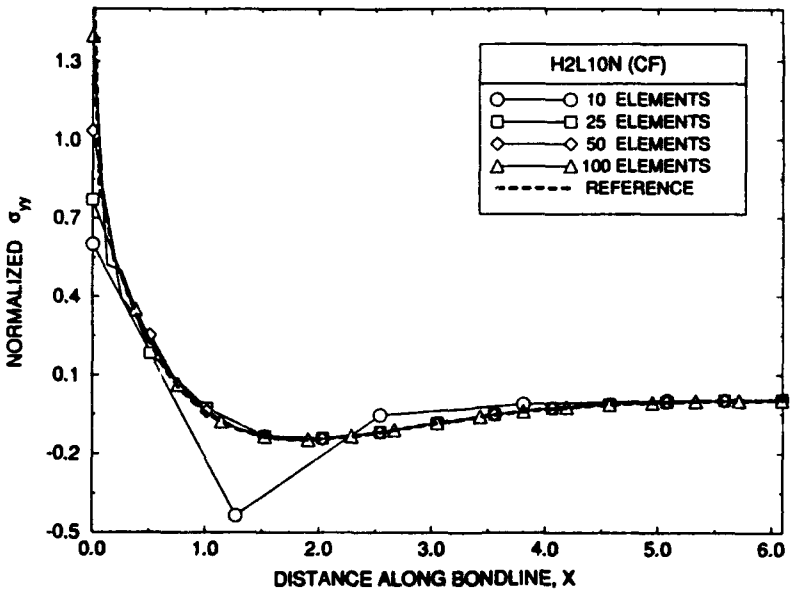

Figure 40. H2L10N Version II σ_{yy} stress distribution along the bondline.

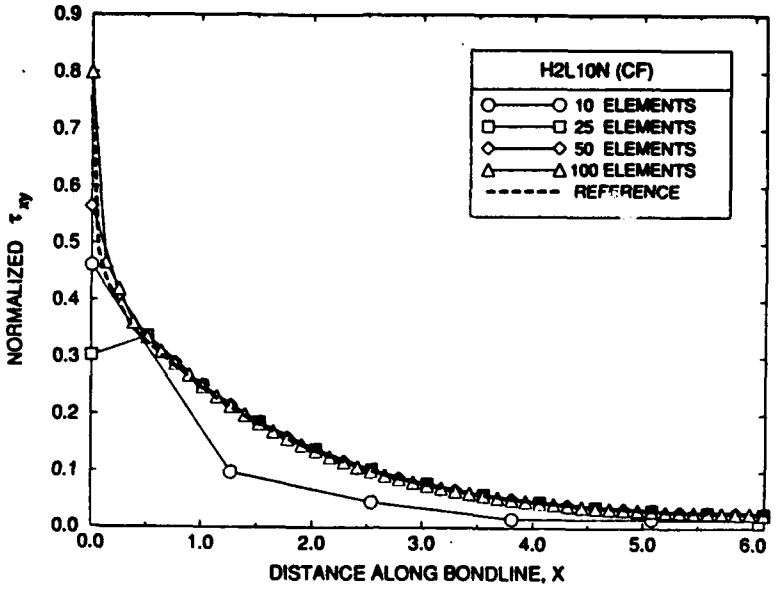

Figure 41. H2L10N Version II τ_{xy} stress distribution along the bondline.

The behavior of these elements demonstrates two interesting effects. Regardless of the higher-order strain representation in the adhesive thickness direction, the normal stress predictions are inferior to the lower-order H2L6N element in predicting maximum stresses in the singular region of the joint. The shear stress recovery in the quadratic stress version shows an inherent tendency of the element to approximate a zero traction condition at the end of the bond. Increasing the order of stress expansion tends to diminish this behavior and increases the maximum normal and shear stress prediction in the region of the singular point. Although, once again, increasing the order of assumed stress expansions improves the results compared to the reference solution, the overall behavior of this element is inferior to the linear-order H2L6N element.

6.3 The H3L8N Element

The H3L8N element is formulated as an 8-node, three layer element as shown in Figure 42. This element is formulated to model both top and bottom interfaces of the adhesive bond with the inner layer representing the adhesive domain. The use of the H3L8N element in adhesive joint modelling is depicted in Figure 43. In anticipation of the high degree of constraint imposed on the stess field to satisfy equilibrium and continuity conditions in three layer domains and two interfaces within a single element configuration, two different assumed stress expansions of increasing order were developed. The two versions of H3L8N were formulated incorporating complete quadratic and cubic stress fields to assess the effect on element performance. All assumed stress expansions provide sufficient independent stress modes to span the 13 basic element strain modes thereby suppressing spurious kinematic modes. Stress continuity of the σ_{yy} and τ_{xy} stress components is strictly enforced at each layer interface and equilibrium is enforced within each element layer.

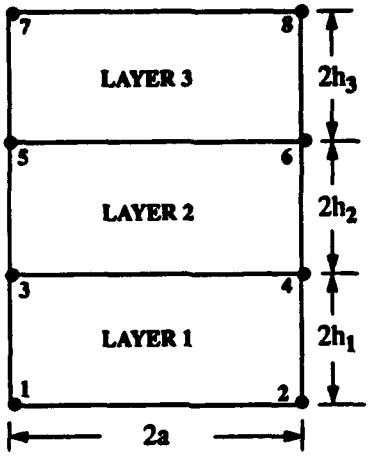

Figure 42. H3L8N element configuration.

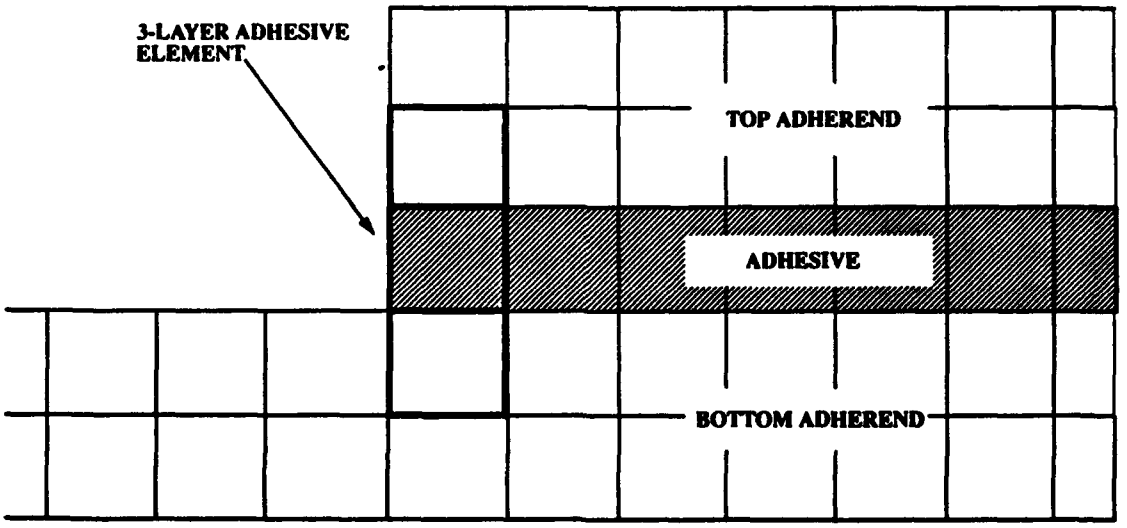

Figure 43. The use of special 3-layered elements in modeling adhesive bonds.

Version I incorporates complete quadratic expansions for each layer in which equilibrium is enforced *a priori* together with the continuity conditions. The resulting stress field possesses 24 independent stress modes which is sufficient to suppress any zero energy modes in the resultant element stiffness matrix. The stress expansions are given by

$$
\begin{aligned}
\sigma^1_{xx} &= \beta_1 + \beta_2 x + \beta_3 y + \beta_4 xy - \beta_5 x^2/2 + \beta_6 y^2 \\
\sigma^1_{yy} &= \beta_9 + \beta_{10} x - \beta_{11} x(h_1 + h_2 - y) + \beta_{12} x^2 - \beta_5 (h_1^2 - 2h_1 y + y^2)/2 + \\
&\quad \beta_7 (y - h_1 - h_2) + \beta_8 h_2 (y - h_1 - h_2/2) \\
\tau^1_{xy} &= \beta_{13} + \beta_2 (h_1 - y) + \beta_4 (h_1^2 - y^2)/2 + \beta_{14} h_2 - \beta_{15} h_2^2/2 - \beta_5 x(h_1 - y) - \\
&\quad \beta_7 x - \beta_8 h_2 x - \beta_{11} x^2/2 \\
\sigma^2_{xx} &= \beta_{16} + \beta_{14} x + \beta_{17} y + \beta_{15} xy - \beta_8 x^2/2 + \beta_{18} y^2 \\
\sigma^2_{yy} &= \beta_9 + \beta_{10} x + \beta_7 y + \beta_{11} xy + \beta_{12} x^2 - \beta_8 y^2/2 \\
\tau^2_{xy} &= \beta_{13} - \beta_7 x - \beta_{14} y + \beta_8 xy - \beta_{11} x^2/2 - \beta_{15} y^2/2 \\
\sigma^3_{xx} &= \beta_{19} + \beta_{20} x + \beta_{21} y + \beta_{22} xy - \beta_{23} x^2/2 + \beta_{24} y^2 \\
\sigma^3_{yy} &= \beta_9 + \beta_7 (h_2 + h_3 + y) - \beta_8 h_2 (h_3 + h_2/2 + y) - \beta_{23} (h_3^2 + 2h_3 y + y^2)/2 + \\
&\quad \beta_{10} x + \beta_{11} x(h_2 + h_3 + y) + \beta_{12} x^2 \\
\tau^3_{xy} &= \beta_{13} - \beta_{14} h_2 - \beta_{15} h_2^2/2 - \beta_{20} (h_3 + y) + \beta_{22} (h_3^2 - y^2)/2 - \beta_7 x + \beta_8 h_2 x + \\
&\quad \beta_{23} x(h_3 + y) - \beta_{11} x^2/2
\end{aligned}
\tag{53}
$$

Version II is formulated with complete cubic stresses to assess the effect of higher-order stress expansions on element performance. The resulting stress field contains 38 independent stress modes and is given by

$$
\begin{aligned}
\sigma^1_{xx} &= \beta_1 + \beta_2 x + \beta_3 y + \beta_4 xy - \beta_5 x^2/2 + \beta_6 y^2 - 3\beta_7 xy^2 - \beta_8 yx^2 - \beta_9 x^3/3 + \beta_{10} y^3 \\
\sigma^1_{yy} &= \beta_{21} - \beta_5 (h_1^2 - 2h_1 y + y^2)/2 - \beta_8 (2h_1^3 - 3h_1^2 y + y^3)/3 + \beta_{23} (h_1 + h_2 - y) - \beta_{15} h_2 (h_1 - h_2/2 + y) + \\
&\quad \beta_{18} h_2^2 (h_1 + h_2/3 - y) - \beta_9 x (h_1^2 - 2h_1 y + y^2) + \beta_{22} x + 2\beta_{24} x(h_1 + h_2 - y) - \\
&\quad \beta_{19} x[2h_2 y - h_2(2h_1 + h_2)] + 3\beta_{26} x^2 (h_1 + h_2 - y) + \beta_{25} x^2 + \beta_{27} x^3 \\
\tau^1_{xy} &= \beta_{28} + \beta_2 (h_1 - y) + \beta_4 (h_1^2 - y^2)/2 - \beta_7 (h_1^3 - y^3) + \beta_{12} h_2 - \beta_{14} h_2^2/2 - \beta_{17} h_2^3 - \beta_5 x(h_1 - y) - \\
&\quad \beta_8 x(h_1^2 - y^2) + \beta_{23} x - \beta_{15} h_2 x + \beta_{18} h_2^2 x - \beta_9 x^2 (h_1 - y) + \beta_{24} x^2 - \beta_{19} h_2 x^2 + \beta_{26} x^3 \\
\sigma^2_{xx} &= \beta_{11} + \beta_{12} x + \beta_{13} y + \beta_{14} xy - \beta_{15} x^2/2 + \beta_{16} y^2 - 3\beta_{17} xy^2 - \beta_{18} yx^2 - \beta_{19} x^3/3 + \beta_{20} y^3 \\
\sigma^2_{yy} &= \beta_{21} + \beta_{22} x - \beta_{23} y - 2\beta_{24} xy + \beta_{25} x^2 - \beta_{15} y^2/2 - \beta_{19} xy^2 - 3\beta_{26} yx^2 + \beta_{27} x^3 - \beta_{18} y^3/3 \\
\tau^2_{xy} &= \beta_{28} + \beta_{23} x - \beta_{12} y + \beta_{15} xy + \beta_{24} x^2 - \beta_{14} y^2/2 + \beta_{18} xy^2 + \beta_{19} yx^2 + \beta_{26} x^3 + \beta_{17} y^3 \\
\sigma^3_{xx} &= \beta_{29} + \beta_{30} x + \beta_{31} y + \beta_{32} xy - \beta_{33} x^2/2 + \beta_{34} y^2 - 3\beta_{35} xy^2 - \beta_{36} yx^2 - \beta_{37} x^3/3 + \beta_{38} y^3 \\
\sigma^3_{yy} &= \beta_{21} - \beta_{23} (y + h_2 + h_3) - \beta_{15} h_2 (h_3 + h_2/2 - y) - \beta_{18} h_2^2 (h_3 + h_2/3 + y) - \beta_{33} (h_3^2 + 2h_3 y + y^2)/2 + \\
&\quad \beta_{36} (2h_3^3 + 3h_3^2 y - y^3)/3 - 2\beta_{24} x(h_2 + h_3 + y) - 2\beta_{19} h_2 x(h_3 + h_2/2 + y) + \\
&\quad \beta_{37} x(h_3^2 - 2h_2 h_3 - 2h_2 y - y^2) + \beta_{22} x + \beta_{25} x^2 - 3\beta_{26} x^2 (h_2 + h_3 + y) + \beta_{27} x^3 \\
\tau^3_{xy} &= -\beta_{12} h_2 - \beta_{14} h_2^2/2 + \beta_{17} h_2^3 + \beta_{28} - \beta_{30} (h_3 + y) + \beta_{32} (h_3^2 - y^2)/2 + \beta_{35} (h_3^3 + y^3) + \beta_{23} x + \beta_{15} h_2 x + \\
&\quad \beta_{18} h_2^2 x + \beta_{33} x(h_3 + y) - \beta_{36} x(h_3^2 - y^2) + \beta_{24} x^2 + \beta_{19} h_2 x^2 + \beta_{37} x^2 (h_3 + y) + \beta_{26} x^3
\end{aligned}
\tag{54}
$$

Figures 44 through 47 show the stress predictions of interface bond stresses for both versions of the H3L8N element.

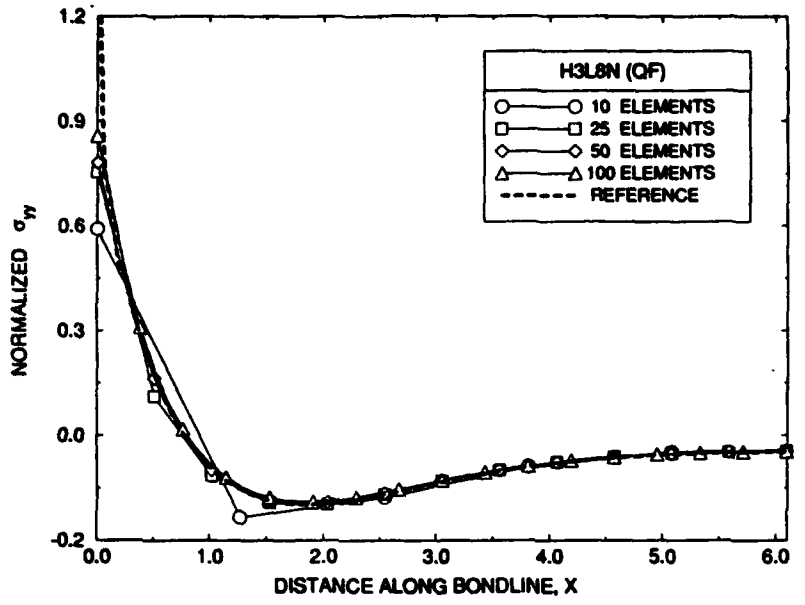

Figure 44. H3L8N Version I σ_{yy} stress distribution along the bondline.

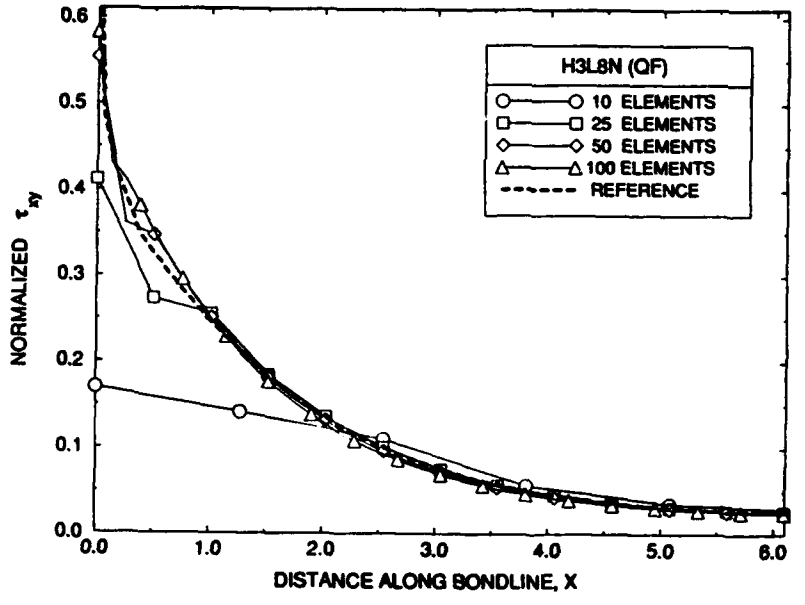

Figure 45. H3L8N Version I τ_{xy} stress distribution along the bondline.

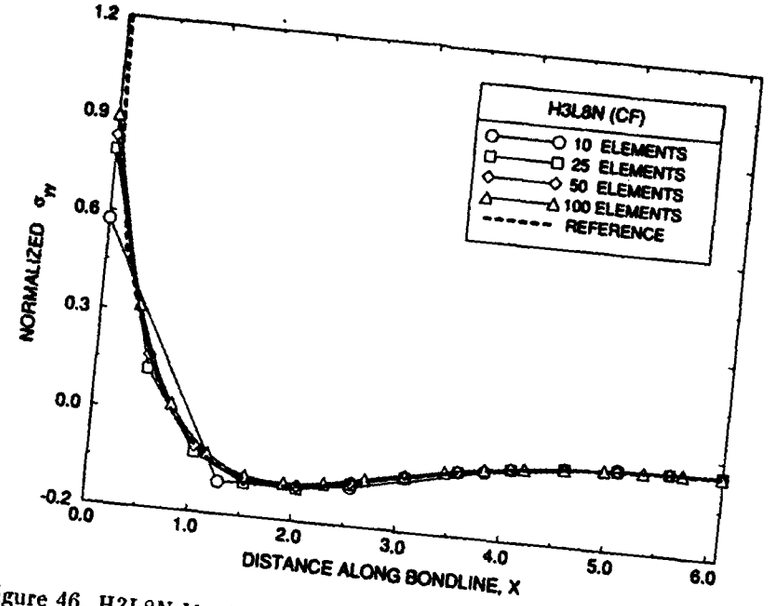

Figure 46. H3L8N Version II σ_{yy} stress distribution along the bondline.

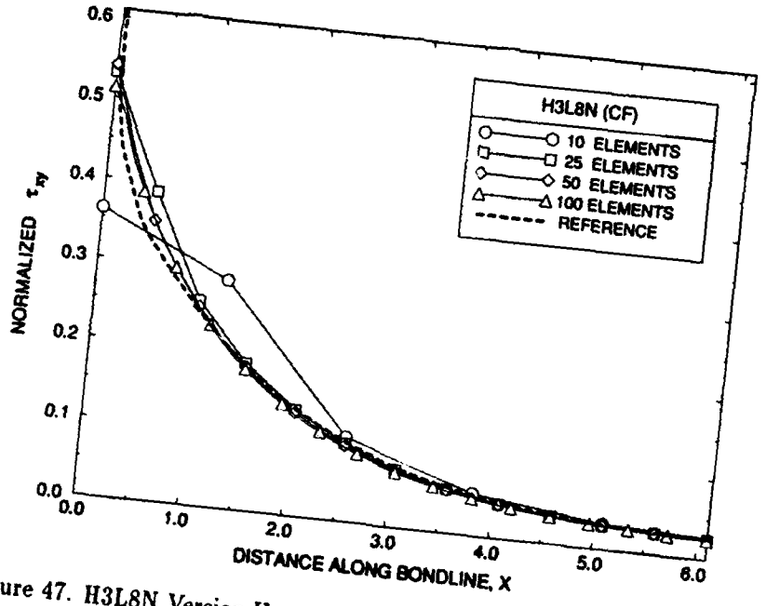

Figure 47. H3L8N Version II τ_{xy} stress distribution along the bondline.

The solutions show uniformly good behavior for the prediction of normal σ_{yy} peeling stresses as compared to the reference solution. The shear stress distribution shows chaotic behavior in the region of the singularity for the quadratic stress field which is alleviated by incorporating the higher-order cubic stress field in the element formulation. While the H3L8N element provides a convenient configuration by allowing a single element to link both upper and lower adherends with an inner layer representing the adhesive, the minimal number of degrees of freedom available to represent the elastic response of the adhesive and the cubic-order

stress field required to obtain convergent element behavior must be contrasted with the use of H2L6N which yields greater accuracy while requiring only lower-order stress field expansions.

An H3L8N element formulation explicitly enforcing zero traction conditions was developed and stress predictions presented in Figures 48 and 49. A quadratic stress field was selected which contains 21 independent modes as given below.

For zero tractions enforced on element side F1

$$
\begin{aligned}
\sigma^1_{xx} &= \beta_1 - x\beta_2 + y\beta_3 - 2xy\beta_4 - x^2\beta_5 + y^2\beta_6 \\
\sigma^1_{yy} &= \beta_8 + (-h_1^2 + 2yh_1 - y^2)\beta_5/2 + (y - h_1 - h_2)\beta_7 + h_2(y - h_1)\beta_9 + \\
&\quad 2x(h_1 - y)\beta_{10} + x\beta_{11} - xh_2\beta_{12} + x^2\beta_{13} \\
\tau^1_{xy} &= (y - h_1)\beta_2 + (y^2 - h_1^2)\beta_4 - (a + x)\beta_7 + (x^2 - a^2)\beta_{10} - \\
&\quad h_2(a + x)\beta_9 + x(y - h_1)\beta_5 \\
\sigma^2_{xx} &= -a(x + a)\beta_9 + (x^2 - a^2)\beta_{14} + y(x + a)\beta_{15} \\
\sigma^2_{yy} &= \beta_8 + x\beta_{11} + y\beta_7 + xy\beta_{12} + x^2\beta_{13} \\
\tau^2_{xy} &= -(x + a)\beta_7 + (x^2 - a^2)\beta_{10} + y(x + a)\beta_9 \\
\sigma^3_{xx} &= \beta_{16} - x\beta_{17} + y\beta_{18} - xy\beta_{19} - x^2\beta_{20}/2 + y^2\beta_{21} \\
\sigma^3_{yy} &= \beta_8 - (h_3^2 + 2h_3y + y^2)\beta_{20}/2 + (h_2 + h_3 + y)\beta_7 - h_2(h_3 + y)\beta_9 - \\
&\quad 2x(h_3 + y)\beta_{10} + x\beta_{11} + h_2x\beta_{12} + x^2\beta_{13} \\
\tau^3_{xy} &= (h_3 + y)\beta_{17} + (y^2 - h_3^2)\beta_{19} - (a + x)\beta_7 + (x^2 - a^2)\beta_{10} + h_2(a + x)\beta_9 + \\
&\quad x(h_3 + y)\beta_{20}
\end{aligned}
\tag{55}
$$

For zero tractions enforced on element side F2

$$
\begin{aligned}
\sigma^1_{xx} &= \beta_1 - x\beta_2 + y\beta_3 - 2xy\beta_4 - x^2\beta_5 + y^2\beta_6 \\
\sigma^1_{yy} &= \beta_8 + (-h_1^2 + 2yh_1 - y^2)\beta_5/2 - (h_1 + h_2 - y)\beta_7 + h_2(y - h_1)\beta_9 + 2x(h_1 - y)\beta_{10} + \\
&\quad x\beta_{11} - xh_2\beta_{12} + x^2\beta_{13} \\
\tau^1_{xy} &= (y - h_1)\beta_2 + (y^2 - h_1^2)\beta_4 + (a - x)\beta_7 + (x^2 - a^2)\beta_{10} + h_2(a - x)\beta_9 + x(y - h_1)\beta_5 \\
\sigma^2_{xx} &= a(x - a)\beta_9 + (x^2 - a^2)\beta_{14} + y(x - a)\beta_{15} \\
\sigma^2_{yy} &= \beta_8 + x\beta_{11} + y\beta_7 + xy\beta_{12} + x^2\beta_{13} \\
\tau^2_{xy} &= (a - x)\beta_7 + (x^2 - a^2)\beta_{10} + y(x - a)\beta_9 \\
\sigma^3_{xx} &= \beta_{16} - x\beta_{17} + y\beta_{18} - xy\beta_{19} - x^2\beta_{20}/2 + y^2\beta_{21} \\
\sigma^3_{yy} &= -(h_3^2 + 2h_3y + y^2)\beta_{20}/2 + (h_2 + h_3 + y)\beta_7 + \beta_8 - h_2(h_3 + y)\beta_9 - 2x(h_3 + y)\beta_{10} + \\
&\quad x\beta_{11} + h_2x\beta_{12} + x^2\beta_{13} \\
\tau^3_{xy} &= (h_3 + y)\beta_{17} + (y^2 - h_3^2)\beta_{19} + (a - x)\beta_7 + (x^2 - a^2)\beta_{10} + h_2(x - a)\beta_9 + x(h_3 + y)\beta_{20}
\end{aligned}
\tag{56}
$$

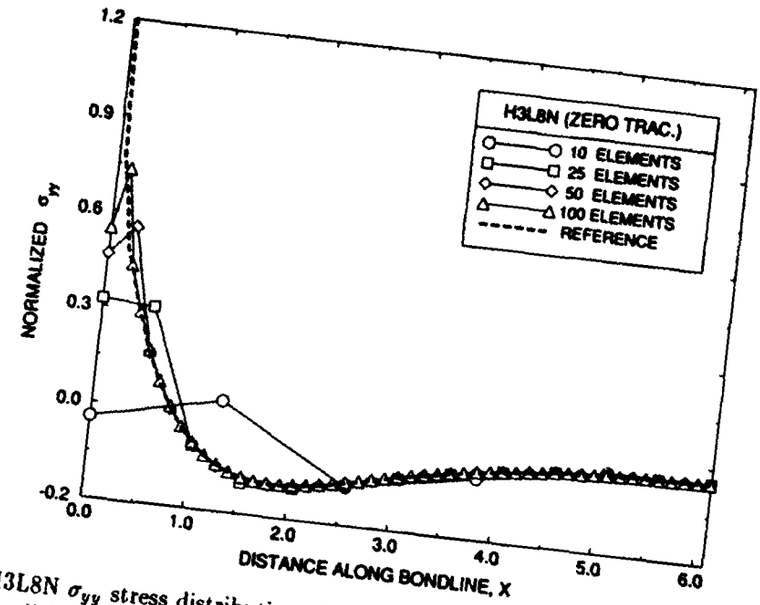

Figure 48. H3L8N σ_{yy} stress distribution along the bondline with imposed zero traction conditions at the end element.

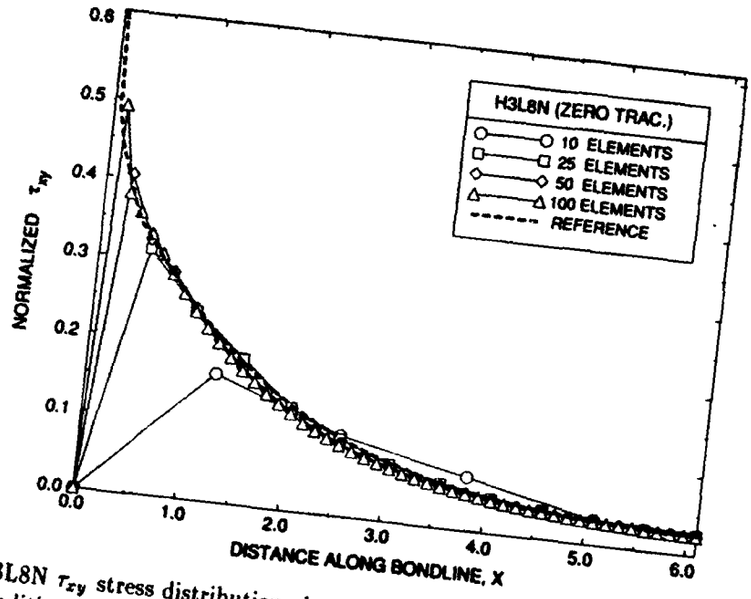

Figure 49. H3L8N τ_{xy} stress distribution along the bondline with imposed zero traction conditions at the end element.

These distributions again show the effect in linear analysis of simply moving the shear stress singularity into the interior of the end element. The coupling between the stress components through the equilibrium relations show the effect of the normal stress in the end element which, as for the τ_{xy} component, moves the singularity slightly into the end element.

6.4 The H2L13N element

The H2L13N element, as shown in Figure 50, is formulated as a 2-layered element incorporating quadratic displacement fields resulting in 8 nodes per layer. Of interest in this element formulation is the inherent improvement in the representation of in-plane bending behavior due to the quadratic isoparametric displacement fields in each layer which is lacking in the linear order elements such as H2L6N and incompletely represented in H2L10N. Incompatible displacement modes can be added to the linear order elements to improve bending response but have not been included in the present effort.

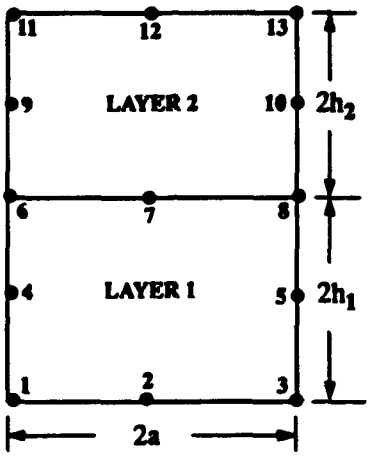

Figure 50. H2L13N element configuration.

An unexpected feature in the development of higher-order layered element configurations is the presence of spurious zero energy modes in the resultant element stiffness matrix which cannot be controlled by adopting higher-order stress expansions while enforcing all layer equilibrium and interface continuity conditions. In order to qualitatively assess this effect, various stress fields were developed. The strain field obtained from the quadratic isoparametric displacement field yields 23 fundamental strain modes which interact with the assumed stress fields in generating element stiffness characteristics. In following the procedure for selecting stress expansions in the linear-order 2-D element, complete cubic and quartic stress fields were developed which incorporate 28 and 40 independent stress modes, respectively, yet both assumed fields yield spurious kinematic modes in the resulting element stiffness matrix. The cubic order expansion is identical to that used in H2L6N and is presented in equation (43). The quartic order expansion is not shown due to the inadequacy of the assumed field to suppress spurious zero energy modes. Although the individual element stiffness matrices are rank deficient, sufficient constraints are introduced through the assembly and support conditions of the complete model to contain the propagation of zero energy modes. Predictions using H2L13N incorporating the complete cubic order stress field are presented in Figures 51 and 52.

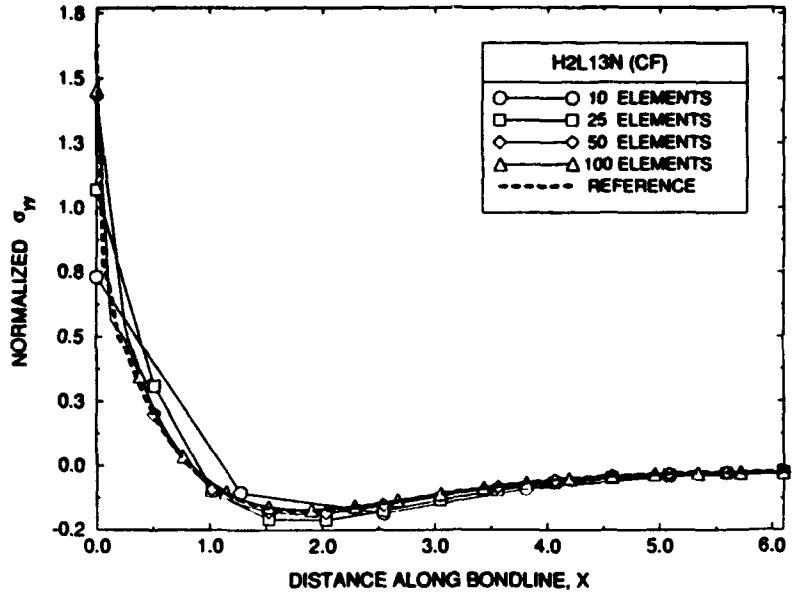

Figure 51. H2L13N σ_{yy} stress distributions incorporating complete cubic stress expansions.

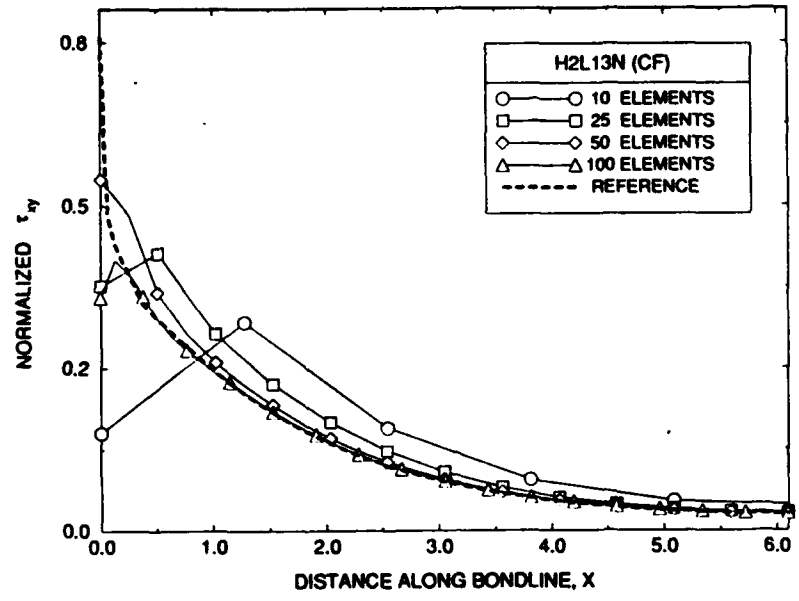

Figure 52. H2L13N τ_{xy} stress distributions incorporating complete cubic stress expansions.

As shown, the solution for normal peel stress distribution is accurate but the transverse shear stress prediction is shown to converge slowly to the reference solution. To assess the effect of increasing the order of assumed stress expansions, predictions using H2L13N incorporating complete quartic order stress field are presented below in Figures 53 and 54.

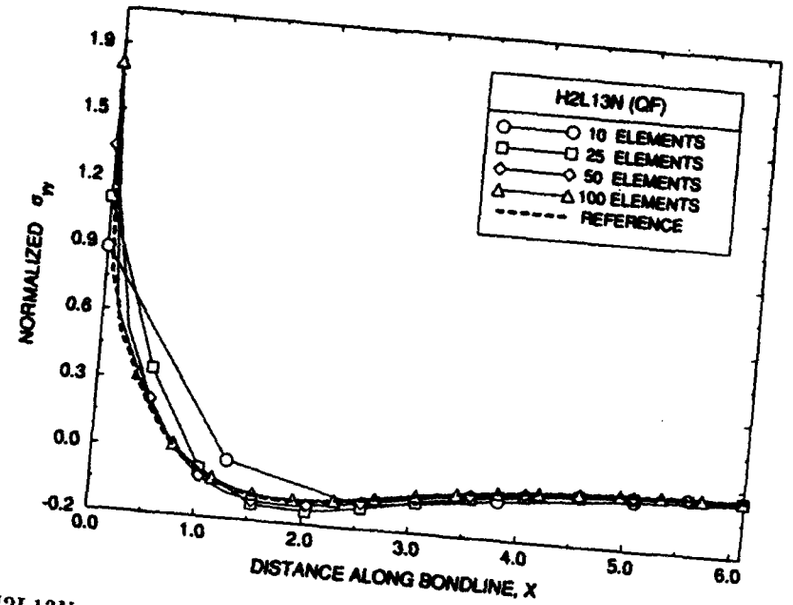

Figure 53. H2L13N σ_{yy} stress distributions incorporating complete quartic stress expansions.

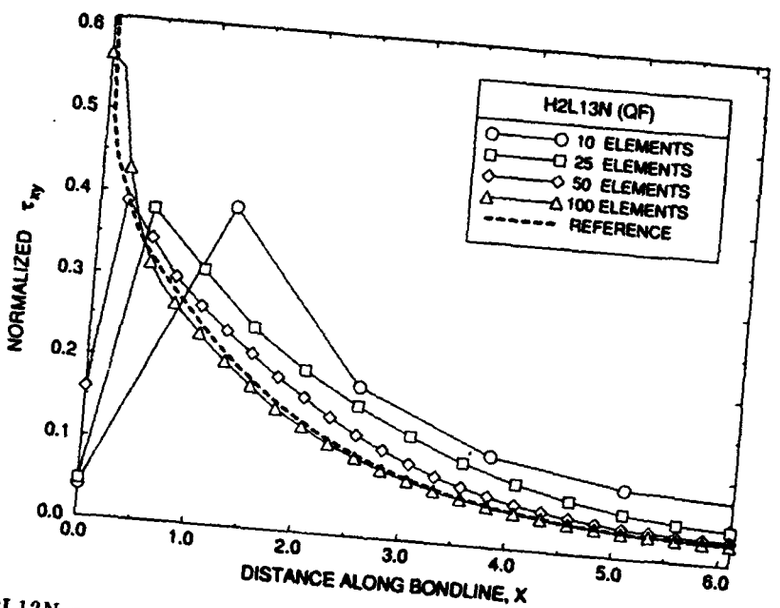

Figure 54. H2L13N τ_{xy} stress distributions incorporating complete quartic stress expansions.

The normal stress component is again adequately predicted but the shear stress prediction shows a similarly poor convergence to the reference solution. The convergence difficulties may be related to the presence of the zero-energy or weak deformation modes which are ameliorated only in a highly discretized model. The general conclusion from the above is that formulating the higher-order H2L13N element with complete stress expansions in which all field constraints are enforced do not yield useful elements due to an unavoidable presence of spurious kinematic modes.

In an attempt to improve element behavior, various augmentations of the applied stress constraints were assessed and are detailed below. A version of H2L13N was developed in which continuity constraints were violated in selected higher-order stress terms to obtain the requisite number of rigid body modes. A detailed analytic approach as presented in Reference [32] was used to precisely identify the strain modes which are independent of the constrained stress field and suggested particular higher-order terms to be added to the assumed stress expansions in order to suppress zero energy modes. Continuity is violated by the addition of two terms - $\beta_{26}x^4$ and $\beta_{27}x^4$ - to the shear stress expansions. The influence of higher-order terms have, in general, a diminishing influence on recovered stresses yet function to stabilize the element stiffness matrix. The resulting stress field contains 27 independent stress modes and may be contrasted with the complete cubic field presented in Equation (43). The developed stress field is given by

$$
\begin{aligned}
\sigma^1_{xx} &= \beta_1 + \beta_2 x + \beta_3 y + \beta_4 x^2 + \beta_5 xy + \beta_6 y^2 + \beta_7 x^3 + 3\beta_8 x^2 y + 3\beta_9 x y^2 \\
\sigma^1_{yy} &= \beta_{11} + \beta_4(h_1^2 - 2h_1 y + y^2) + \beta_8(2h_1^3 - 3h_1^2 y + y^3) + \beta_{16}(y - h_1 - h_2) + \beta_{17} h_2(h_2 + 2h_1 - 2y) + \\
&\quad \beta_{23} h_2^2(3y - h_2 - 3h_1) + 3\beta_7 x(h_1^2 - 2h_1 y + y^2) + \beta_{20} x(y - h_1 - h_2) + 3\beta_{22} x h_2(2h_1 + h_2 - 2y) + \\
&\quad \beta_{14} x + \beta_{25} 3x^2(y - h_1 - h_2) + \beta_{18} x^2 \\
\tau^1_{xy} &= \beta_{12} + \beta_2(h_1 - y) + \beta_5(h_1^2 - y^2)/2 + \beta_9(h_1^3 - y^3) + \beta_{13} h_2 - \beta_{19} h_2^2/2 + \beta_{24} h_2^3 + \\
&\quad 2\beta_4 x(h_1 - y) + \beta_8 x(2h_1^2 - 3y^2) - \beta_{16} x + 2\beta_{17} h_2 x - 3\beta_{23} h_2^2 x + 3\beta_7 x^2(h_1 - y) - \\
&\quad \beta_{20} x^2/2 + 3\beta_{22} h_2 x^2 - \beta_{25} x^3 + \beta_{26} x^4 \\
\sigma^2_{xx} &= \beta_{10} + \beta_{13} x + \beta_{15} y + \beta_{17} x^2 + \beta_{19} xy + \beta_{21} y^2 + \beta_{22} x^3 + 3\beta_{23} x^2 y + 3\beta_{24} x y^2 \\
\sigma^2_{yy} &= \beta_{11} + \beta_{14} x + \beta_{16} y + \beta_{17} y^2 + \beta_{18} x^2 + \beta_{20} xy + 3\beta_{22} x y^2 + \beta_{23} y^3 + 3\beta_{25} x^2 y \\
\tau^2_{xy} &= \beta_{12} - \beta_{13} y - \beta_{16} x - 2\beta_{17} xy - \beta_{19} y^2/2 - \beta_{20} x^2/2 - 3\beta_{22} x^2 y - 3\beta_{23} x y^2 - \\
&\quad \beta_{24} y^3 - \beta_{25} x^3 + \beta_{27} x^4
\end{aligned}
\tag{57}
$$

Figures 55 and 56 depicts normal and shear stress predictions along the adhesive/adherend interface using H2L13N incorporating the above stress field.

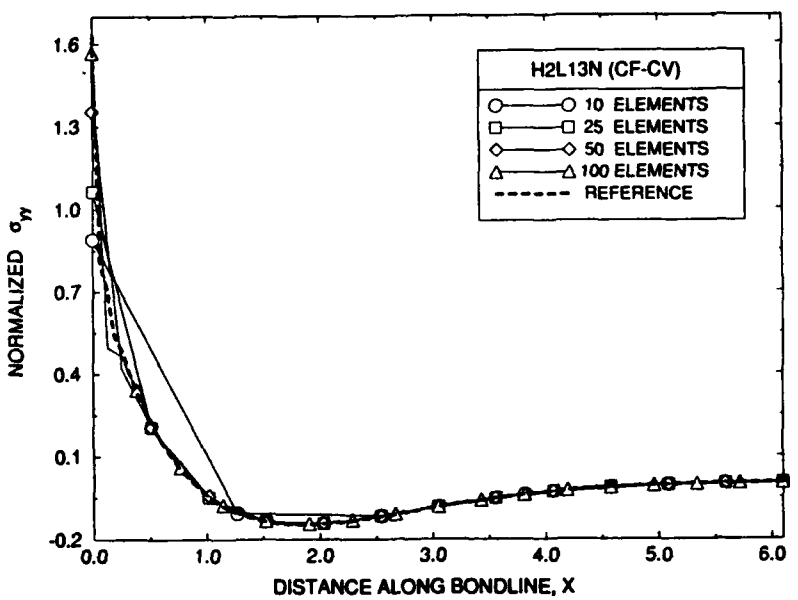

Figure 55. H2L13N σ_{yy} stress distributions with continuity violated in higher-order shear stress terms.

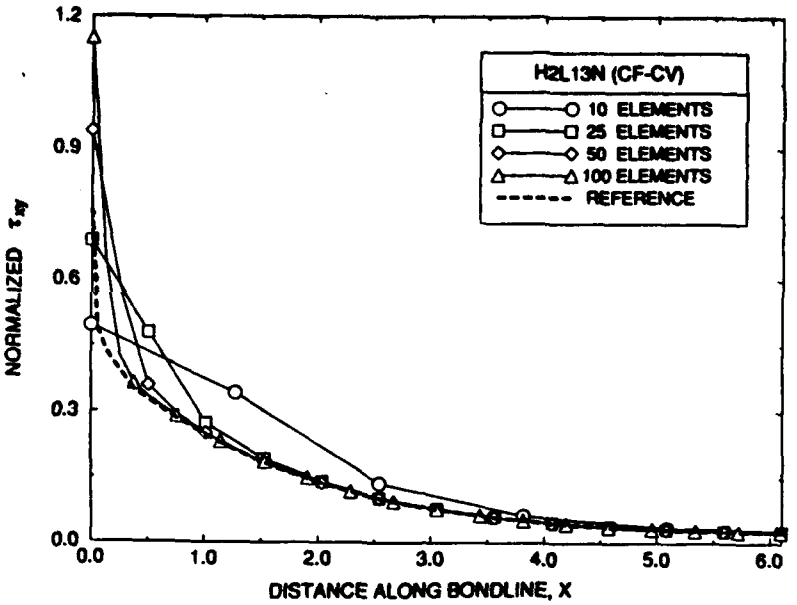

Figure 56. H2L13N τ_{xy} stress distributions with continuity violated in higher-order shear stress terms.

The eigencharacteristics of the element demonstrate the requisite three rigid body modes and the convergence is improved for both stress components. The peak normal and shear stress predictions at the joint end - which is a nonconvergent point in the model in linear elastic analysis - shows that this version of H2L13N is superior in 'capturing' the singular behavior than even the highly discretized model used for the reference solution. Although strict continuity is violated in the interface shear stresses, the unconstrained shear expansion terms are of quartic order which have only a small contribution to the total recovered shear stresses yet are capable of stabilizing the element by removing spurious zero energy modes.

In order to avoid violating continuity constraints, an alternative formulation was developed in which full interface continuity is enforced but layer equilibrium conditions are relaxed such that the field equilibrium equations were satisfied in an integral sense rather than pointwise. This condition is enforced by requiring that

$$\int_v [\frac{\delta \sigma^i_{xx}}{\delta x} + \frac{\delta \tau^i_{xy}}{\delta y}] dv = 0, \qquad \int_v [\frac{\delta \tau^i_{xy}}{\delta x} + \frac{\delta \sigma^i_{yy}}{\delta y}] dv = 0 \tag{58}$$

With this formulation, stress field constraints due to enforcing equilibrium are significantly reduced. The resulting field contains 26 independent stress modes given by

$$\begin{aligned}
\sigma^1_{xx} &= \beta_6 + y^2\beta_1 + x^2\beta_2 + xy\beta_3 + y\beta_4 - x\beta_5 \\
\sigma^1_{yy} &= \beta_{14} + (y^2 - h_1^2)\beta_7 + (y - h_1)\beta_8 + x(y - h_1)\beta_9 + x^2\beta_{10} - h_2 x\beta_{11} - h_2\beta_{12} + \\
&\quad x\beta_{13} + h_2^2\beta_{15} \\
\tau^1_{xy} &= \beta_{19} + x(y - h_1)/h_1\beta_8 + y^2\beta_{16} - xy/h_1\beta_{12} + x^2\beta_{17} + y\beta_5 - xyh_2/h_1\beta_{18} \\
\sigma^2_{xx} &= \beta_{20} + y^2\beta_{21} + x^2\beta_{22} + xy\beta_{23} + y\beta_{24} + x\beta_{25} \\
\sigma^2_{yy} &= \beta_{14} + x^2\beta_{10} + xy\beta_{11} + y\beta_{12} + x\beta_{13} + y^2\beta_{15} \\
\tau^2_{xy} &= \beta_{19} + (y^2 - h_2^2)\beta_{26} - (h_2 + y)\beta_{25} + h_1^2\beta_{16} - x\beta_{12} + x^2\beta_{17} + h_1\beta_5 + xy\beta_{18}
\end{aligned} \tag{59}$$

Figures 57 and 58 depicts the interface stress predictions using H2L13N incorporating the above stress field.

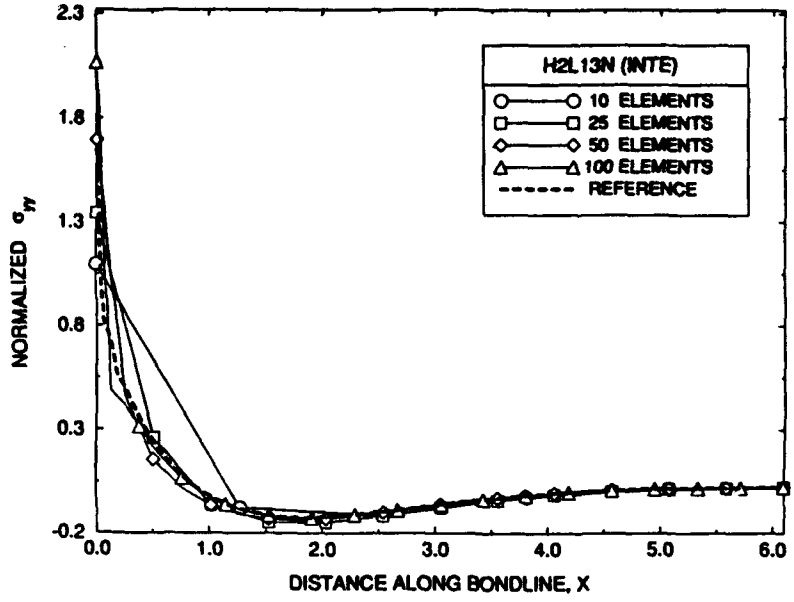

Figure 57. H2L13N σ_{yy} stress distributions with relaxed equilibrium constraints.

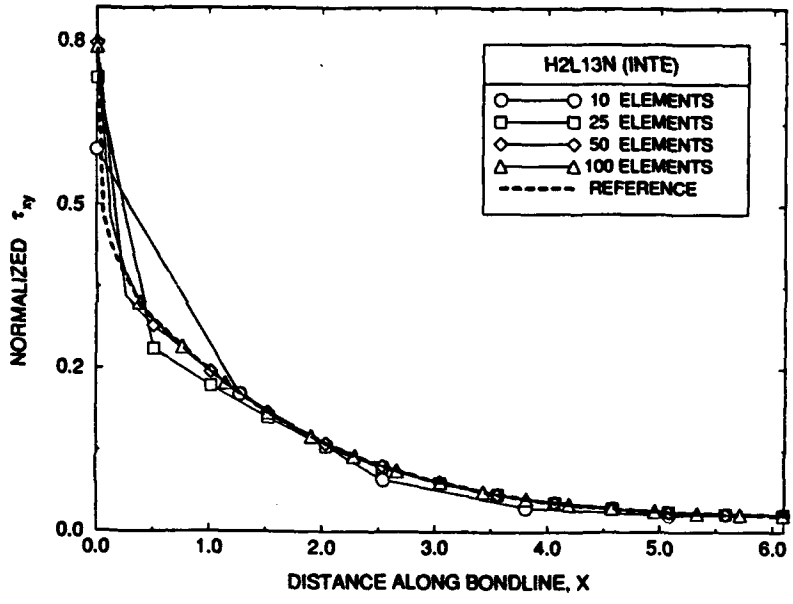

Figure 58. H2L13N τ_{xy} stress distributions with relaxed equilibrium constraints.

An eigenanalysis of this element demonstrates the presence of two spurious zero energy modes indicating that the relaxation of equilibrium with the 'weak' form as given above in equation (59) still yields stress fields which do not span the strain space. The performance of the element is good in the particular single-lap joint used to provide a comparison between various elements assessed in the current study but is unsuitable for use as a general element.

To explore in greater detail the effect of imposed constraints, a version of H2L13N was developed in which all interface continuity conditions were eliminated and only layer equilibrium constraints were enforced pointwise. A complete quadratic field yielded three spurious kinematic modes and was discarded. A complete cubic field was found to span the strain space which yielded only the requisite zero energy modes associated with rigid body modes. The resulting field contains 36 independent stress modes given by

$$
\begin{aligned}
\sigma^1_{xx} &= \beta_{10} - 3xy^2\beta_1 + y^2\beta_2 + y\beta_3 - x^2y\beta_4 - x^3\beta_5/3 - 2xy\beta_6 - x^2\beta_7/2 - x\beta_8 - y^3\beta_9 \\
\sigma^1_{yy} &= \beta_{17} - 3x^2y\beta_{11} - y^3\beta_4/3 - xy^2\beta_5 - 2xy\beta_{12} - y^2\beta_7/2 - y\beta_{13} + x^3\beta_{14} + x^2\beta_{15} + x\beta_{16} \\
\tau^1_{xy} &= \beta_{18} + y^3\beta_1 + x^3 \quad + xy^2\beta_4 + x^2y\beta_5 + y^2\beta_6 + x^2\beta_{12} + xy\beta_7 + y\beta_8 + x\beta_{13} \\
\sigma^2_{xx} &= \beta_{26} - x^2y\beta_{19} - x^3\beta_{20}/3 - 2xy\beta_{21} + y^2\beta_{22} - x^2\beta_{23}/2 - x\beta_{24} + y\beta_{25} - 2xy^2\beta_{27} + y^3\beta_{28} \\
\sigma^2_{yy} &= \beta_{35} - y\beta_{29} - 3x^2y\beta_{30} - y^3\beta_{19}/3 - xy^2\beta_{20} + x^3\beta_{31} - 2xy\beta_{32} - y^2\beta_{23}/2 + x^2\beta_{33} + x\beta_{34} \\
\tau^2_{xy} &= \beta_{36} + y^3\beta_{27} + x^3\beta_{30} + xy^2\beta_{19} + x^2y\beta_{20} + y^2\beta_{21} + x^2\beta_{32} + xy\beta_{23} + y\beta_{24} + x\beta_{29}
\end{aligned}
\tag{60}
$$

Predictions of bondline stresses are depicted below in Figures 59 and 60.

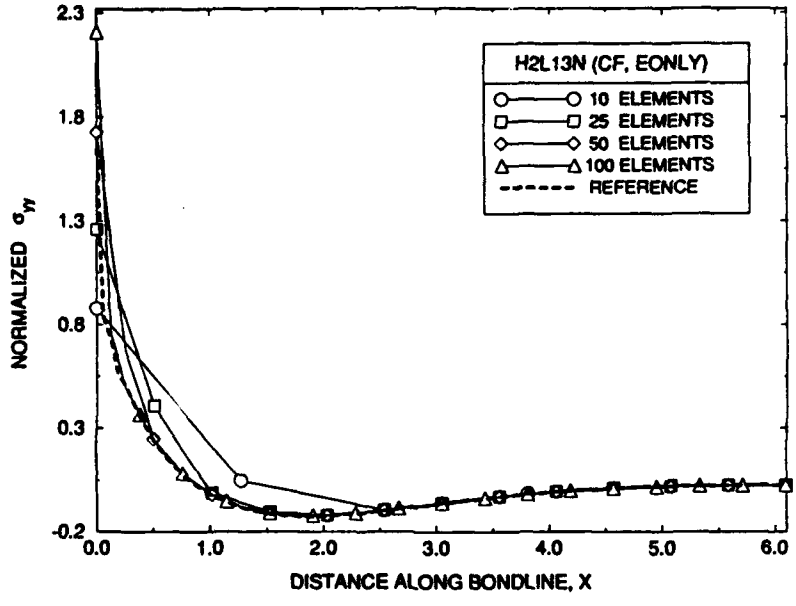

Figure 59. H2L13N σ_{yy} stress distributions with only layer equilibrium conditions enforced.

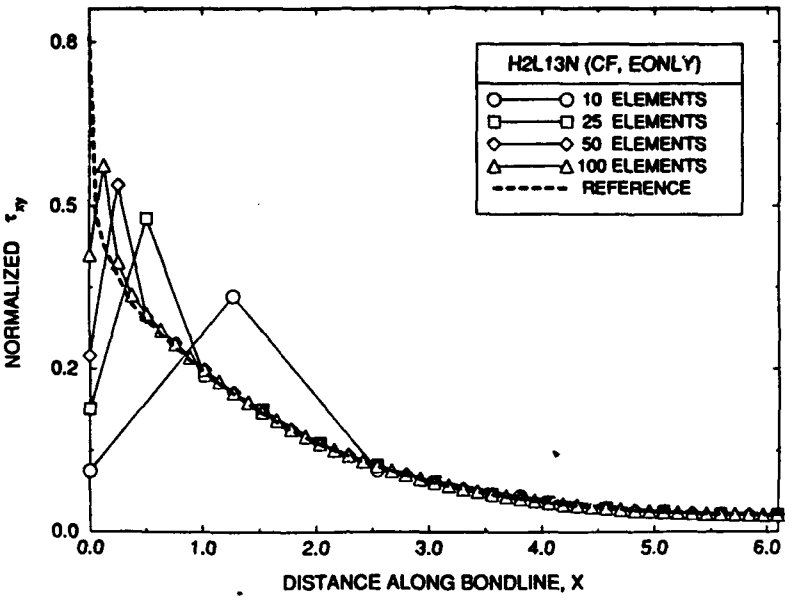

Figure 60. H2L13N τ_{xy} stress distributions with only layer equilibrium conditions enforced.

As shown, the normal stress predictions show a convergence to the reference solution, but, with the removal of continuity constraints, the shear stress distribution is incorrectly predicted.

An element utilizing a complete quadratic stress field was formulated in which the enforcement of layer equilibrium was eliminated and only interface continuity was enforced. As presented below, the resulting stress field possesses 30 independent stress modes and does not exhibit any spurious zero energy deformation modes.

$$
\begin{aligned}
\sigma^1_{xx} &= \beta_6 + y^2\beta_1 + x^2\beta_2 + xy\beta_3 + y\beta_4 + x\beta_5 \\
\sigma^1_{yy} &= \beta_9 + x(y-h_1)\beta_7 + y\beta_8 + x^2\beta_{10} - xh_2\beta_{11} + x\beta_{12} + y^2\beta_{13} \\
\tau^1_{xy} &= \beta_{19} + y^2\beta_{14} + xy\beta_{15} + x^2\beta_{16} + y\beta_{17} + x\beta_{18} \\
\sigma^2_{xx} &= \beta_{20} + y^2\beta_{21} + x^2\beta_{22} + xy\beta_{23} + y\beta_{24} + x\beta_{25} \\
\sigma^2_{yy} &= \beta_9 + (y^2 - h_2^2)\beta_{26} + (h_2 + y)\beta_{27} + h_1\beta_8 + x^2\beta_{10} + xy\beta_{11} + x\beta_{12} + h_1^2\beta_{13} \\
\tau^2_{xy} &= \beta_{19} + (y^2 - h_2^2)\beta_{28} + x(y + h_2)\beta_{29} + (h_2 + y)\beta_{30} + h_1^2\beta_{14} + h_1x\beta_{15} + \\
&\quad x^2\beta_{16} + h_1\beta_{17} + x\beta_{18}
\end{aligned}
\tag{61}
$$

The resulting element stress predictions are presented below in Figures 61 and 62.

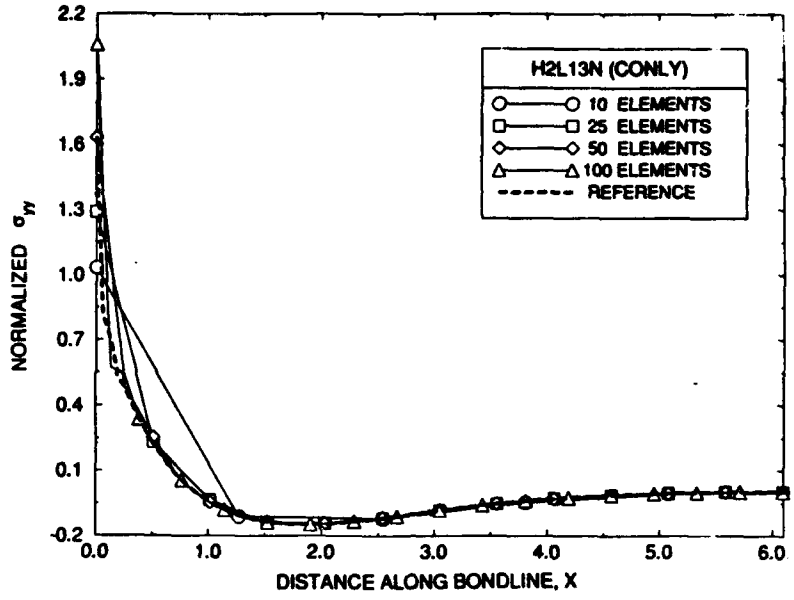

Figure 61. H2L13N σ_{yy} stress distributions with only continuity conditions applied.

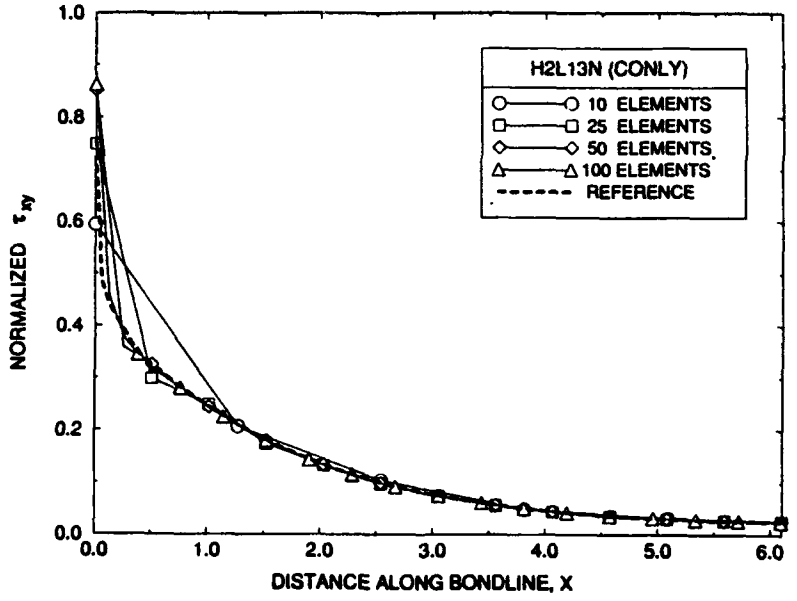

Figure 62. H2L13N τ_{xy} stress distributions with only continuity conditions applied.

Rapid convergence to the reference solution is demonstrated which constrasts with the reduced convergence behavior demonstrated in H2L6N with similar stress field constraints applied. This shows that in a higher-order formulation, the neglect of satisfying layer equilibrium appears to have little influence in accurately predicting stress distributions in the problem under study. It also demonstrates the importance of enforcing stress continuity at the layer interfaces in realizing greater accuracy in layered hybrid formulations.

A comparative eigenanalysis is presented in Table 2 below. Isotropic material properties were selected with $E = 1000.0$ and $\mu = 0.25$ for each layer and layer dimensions were chosen to be unity. For a 2-D element, the three required rigid body modes are depicted in Figure 63 and the two spurious kinematic modes resulting from the use of cubic and quartic stress fields are depicted in Figure 64. Without performing a detailed analysis of independent element strain energy contributions, it is apparent that the combined application of field equilibrium and interface continuity conditions constrain the assumed stress field such that spurious kinematic modes are unavoidable without selective relaxation or violation of constraints to stabilize the element. The continuity constraints link the stress fields in each layer and tend to combine stress modes which are a function of the thickness coordinate which diminishes their span of the strain space as a function of y. As can be seen in Figure 64, the deformation modes corresponding to zero strain energy states qualitatively show that they are exclusively composed of v component deformations which are functions of the thickness coordinate.

Table 2. Comparison of eigenvalues obtained in the H2L13N element incorporating various stress fields: complete cubic (Cubic-I), complete quartic (Quart-I), modified cubic (Cubic-II), quadratic with relaxed equilibrium constraints (Quad-I), cubic with only equilibrium enforced (Cubic III) and quadratic with only continuity conditions (Quad-II).

λ	Cubic-I	Quartic-I	Cubic-II	Quad-I	Cubic-III	Quad-II
1	0.0	0.0	0.0	0.0	0.0	0.0
2	0.0	0.0	0.0	0.0	0.0	0.0
3	0.0	0.0	0.0	0.0	0.0	0.0
4	0.0	0.0	23.69772	0.0	72.43028	60.86598
5	0.0	0.0	34.05380	0.0	163.0501	78.74336
6	75.76981	82.01182	76.95349	60.53644	225.6264	156.9013
7	126.6998	227.4995	134.2405	81.16368	268.1523	161.8190
8	178.7381	278.2503	196.9742	80.78365	314.8713	331.5214
9	211.6415	337.8555	218.3887	172.7010	388.8823	358.9699
10	293.2313	378.8533	316.7293	173.2961	391.7162	413.1536
11	325.1373	441.0916	341.2829	331.0209	458.1095	557.5755
12	355.5333	480.2937	386.6343	376.4624	553.0599	564.5969
13	371.5992	545.4102	431.6523	424.4714	603.3747	809.1861
14	405.7435	568.8378	530.7245	474.6536	733.2789	920.7719
15	517.5139	602.9718	587.1902	559.7191	753.5590	988.4729
16	587.8730	715.4142	640.0043	577.7691	766.3474	1010.934
17	674.6511	773.2681	768.9178	929.2014	1040.206	1259.228
18	766.4438	152.7025	901.8028	913.4121	1152.900	1403.390
19	819.4111	950.2543	1013.777	1071.387	1221.521	1643.767
20	1044.450	1110.563	1083.736	1211.052	1361.066	1974.218
21	1087.227	1181.065	1123.716	1389.199	1420.998	2549.088
22	1210.914	1288.766	1555.517	1672.933	1537.543	2768.760
23	1469.354	1548.891	1575.495	1726.760	1851.332	3645.037
24	1529.672	1595.397	1580.724	2022.144	1969.350	4235.017
25	1866.629	1871.165	1936.631	2680.260	2462.195	4727.452
26	1950.449	1961.606	2113.241	3173.282	3038.038	7906.456

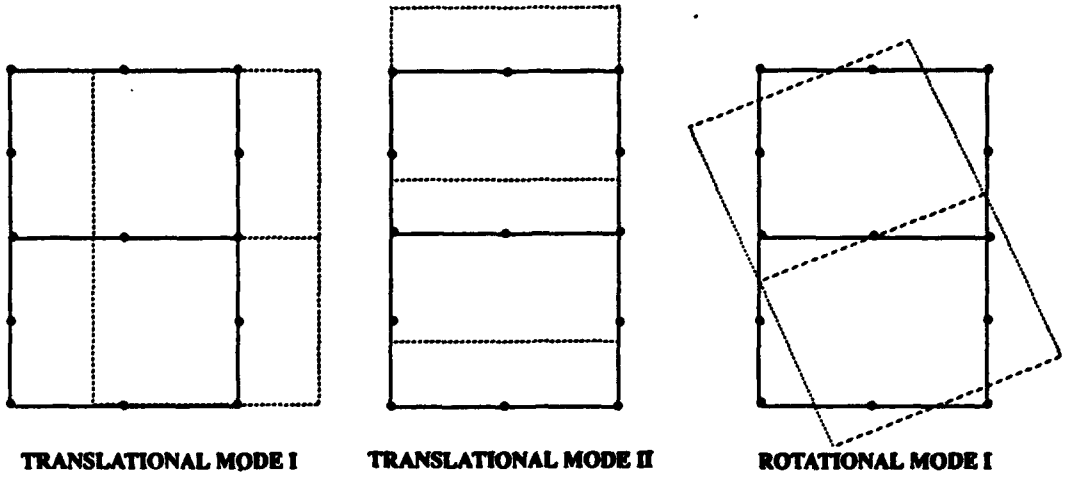

Figure 63. Required translational and rotational rigid body modes

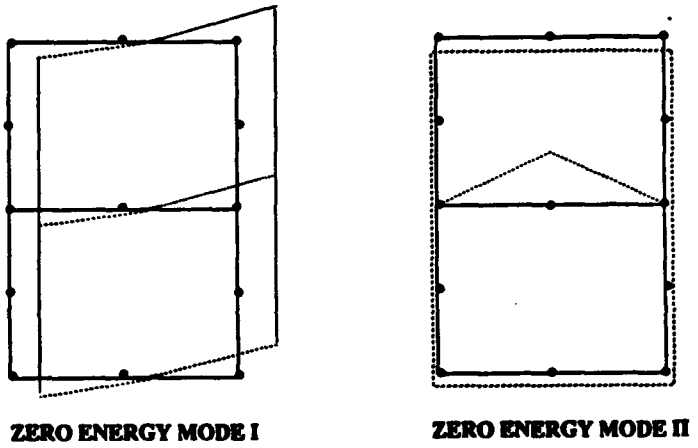

Figure 64. Spurious kinematic modes.

The inability to enforce all stress field constraints without giving rise to zero energy modes makes the general utility of the higher-order H2L13N element questionable. Although accurate stress predictions are demonstrated in the 'Cubic-II' version in which higher-order expansion terms are introduced which violate continuity and in the 'Quad-II' version in which only continuity is enforced, element performance may degrade in the modelling of other general adhesive joint configurations.

6.5 Remarks on 2-D Element Behavior

The detailed study undertaken with various 2-D element formulations has highlighted certain features of the hybrid stress method in layered element configurations which may provide insight into the use of the hybrid technique in other similar applications. For the present use in developing layered element formulations for the analysis of adhesive joints, various observations may be summarized. The study of the linear-order H2L6N element involving selective enforcement of stress equilibrium and continuity constraints has demonstrated that the best performing element formulation is one which strictly enforces all constraints. A related conclusion is drawn from the use of the partial hybrid stress functional as the stress prediction has been shown to deteriorate due to the mixed nature of the element incorporating both displacement-based and stress-based element field assumptions. Related to the H2L6N element performance in which field equilibrium conditions are neglected, the inability of enforcing field equilibrium in each layer with the partial hybrid functional, leads to inaccuracies in the prediction of bondline stresses. The investigation of selective

higher-order element formulations such as in H2L10N results in an element which offers no advantage. The formulation of a fully higher-order layered element configuration as in H2L13N results in an element with an inherent presence of kinematic modes if all constraint equations are strictly applied to the assumed stress fields. The performance of various higher-order element formulations over lower-order elements have not demonstrated significantly improved performance in the prediction of bondline stresses. It is therefore concluded that the optimum 2-D stress prediction is obtained in linear-order layered element formulations in which all stress constraints are identically satisfied pointwise.

7 3-D Special Adhesive Elements

Two 3-D adhesive joint problems are analyzed involving a rectangular and a tapered single-lap joint. Nodal variables are restricted to u, v and w translational degrees of freedom. The joint geometries are depicted above in Figures 5 and 6. The applied loading and boundary conditions are shown above in Figure 7. As previously discussed, reference solutions are obtained from a highly discretized 2-D model using 8-node plane-strain elements shown in Figure 4. For the 3-D single-lap joint with rectangular planform, the 2-D reference solution is used directly assuming negligible three-dimensional effects through the joint width. In the 3-D tapered joint, stresses from the 2-D reference solution are linearly scaled to account for the effect of stress intensification as a function of joint taper. The reference solutions for the σ_{zz} and τ_{xz} stress distributions together with a depiction of the τ_{yz} stress field over the adhesive domain are presented in Figures 65 through 70 for the rectangular and tapered joint configurations. The τ_{yz} distribution was obtained using the developed 3-D hybrid elements discussed below and shows the three-dimensional singular nature of this stress component at the bond corners. Because all stress components are related through equilibrium constraints, the presence of this effect causes a slight departure of predicted σ_{zz} and τ_{xz} stresses from the reference solution obtained from the 2-D plane-strain model. Stress recovery for the rectangular configuration was obtained along the lower adhesive/adherend interface while, in the tapered joint, stresses were recovered along the upper interface.

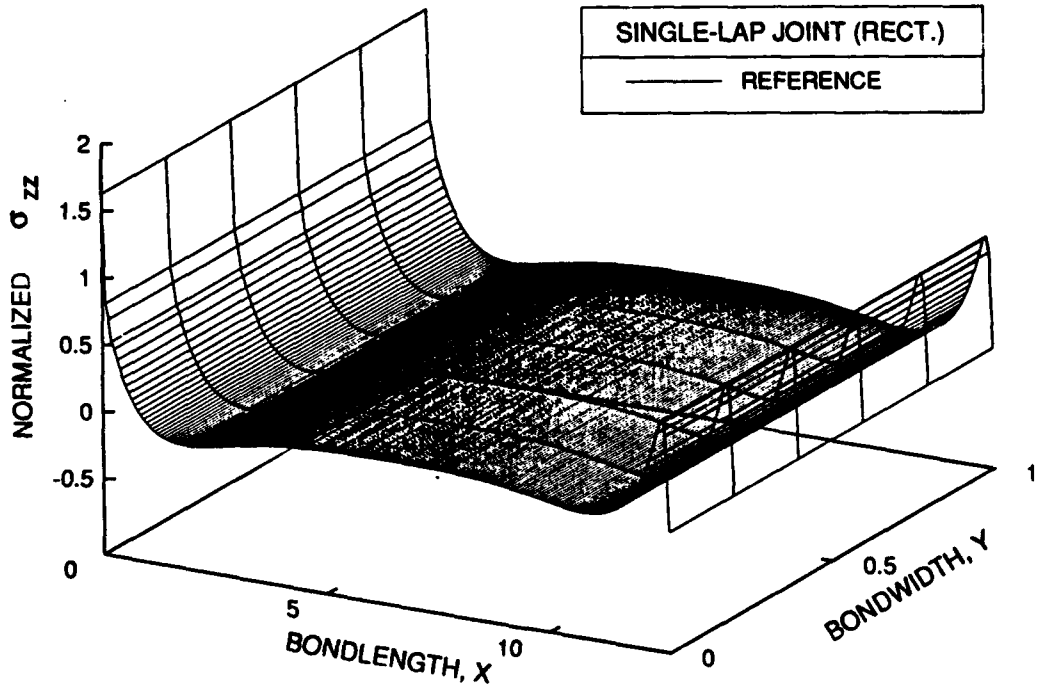

Figure 65. Reference σ_{zz} stress distribution in the rectangular 3-D single-lap joint.

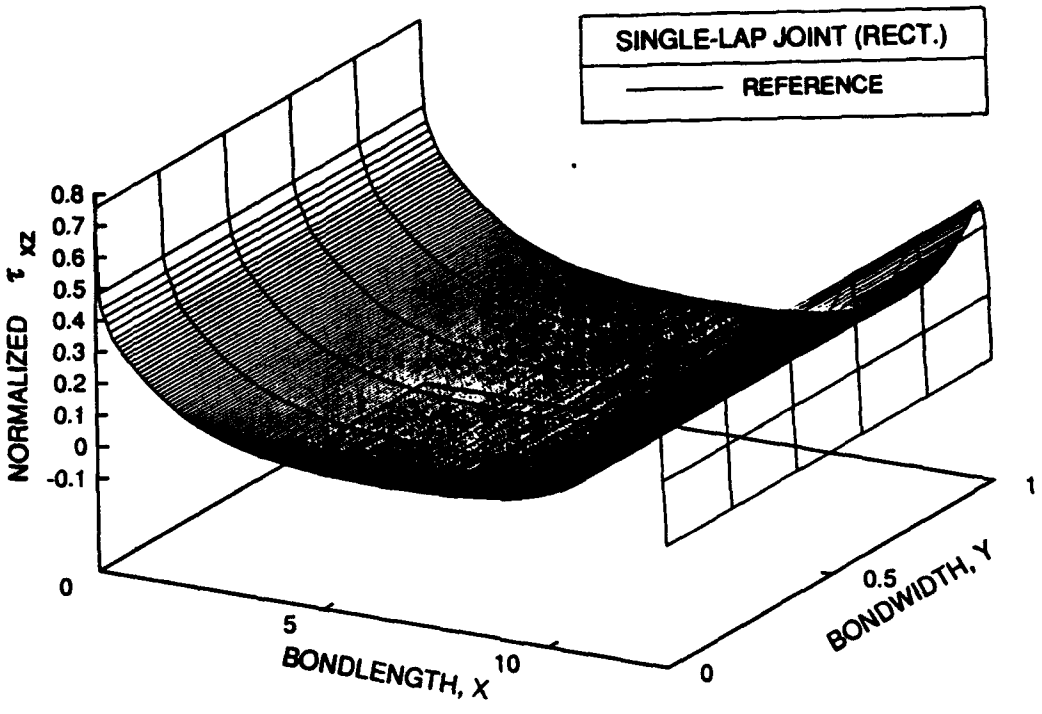

Figure 66. Reference τ_{xz} stress distribution in the rectangular 3-D single-lap joint.

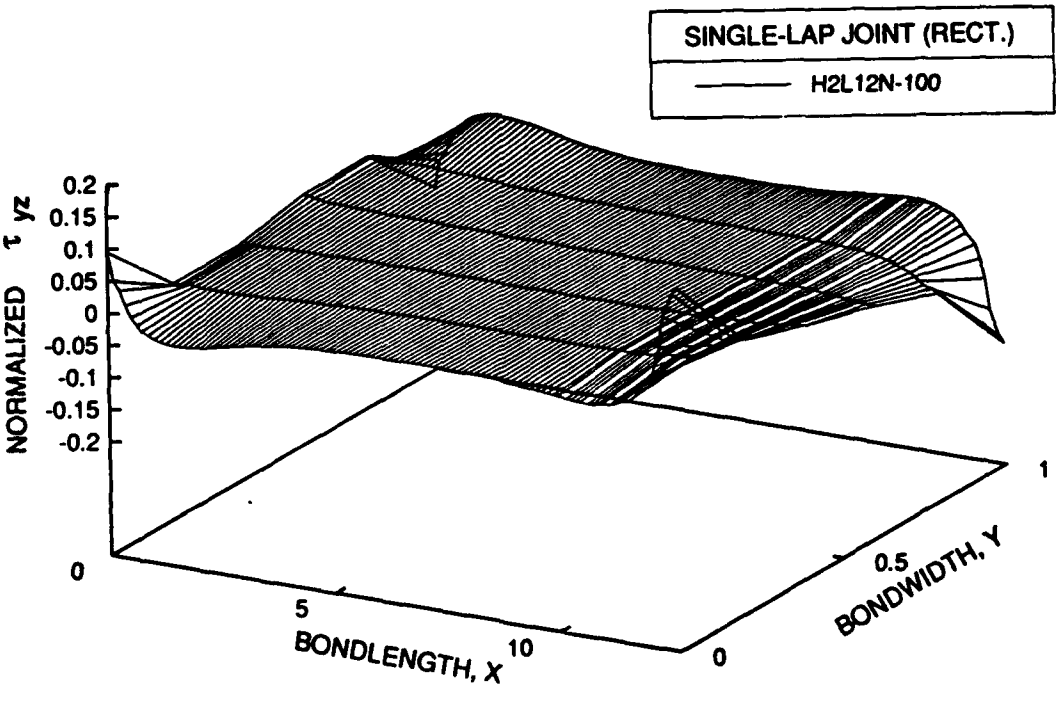

Figure 67. Singular τ_{yz} stress field in the rectangular 3-D single-lap joint.

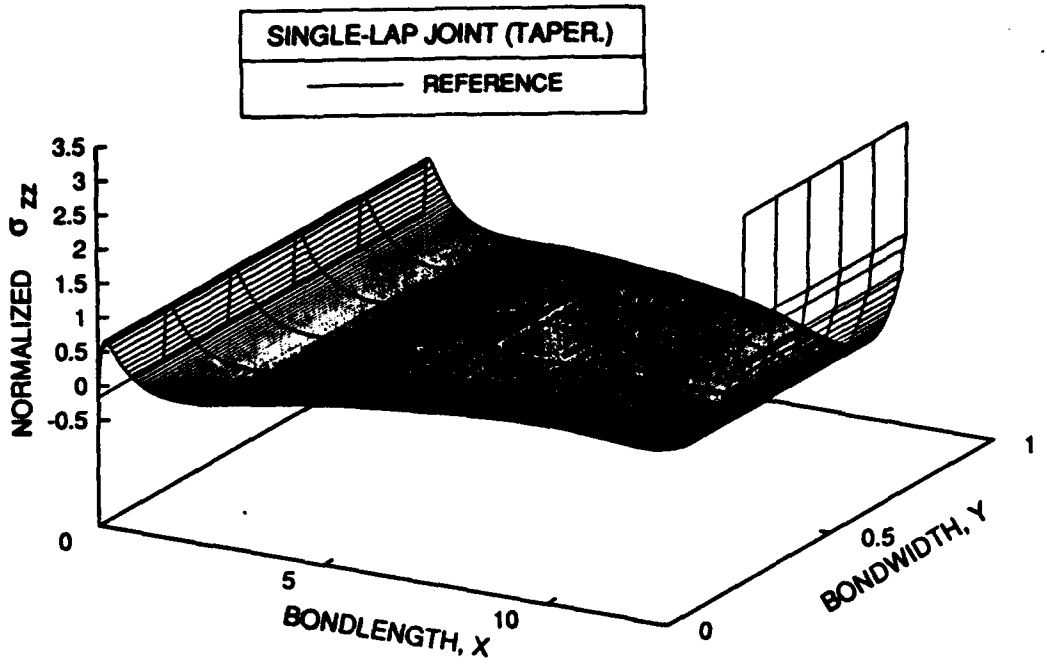

Figure 68. Reference σ_{zz} stress distribution in the tapered 3-D single-lap joint.

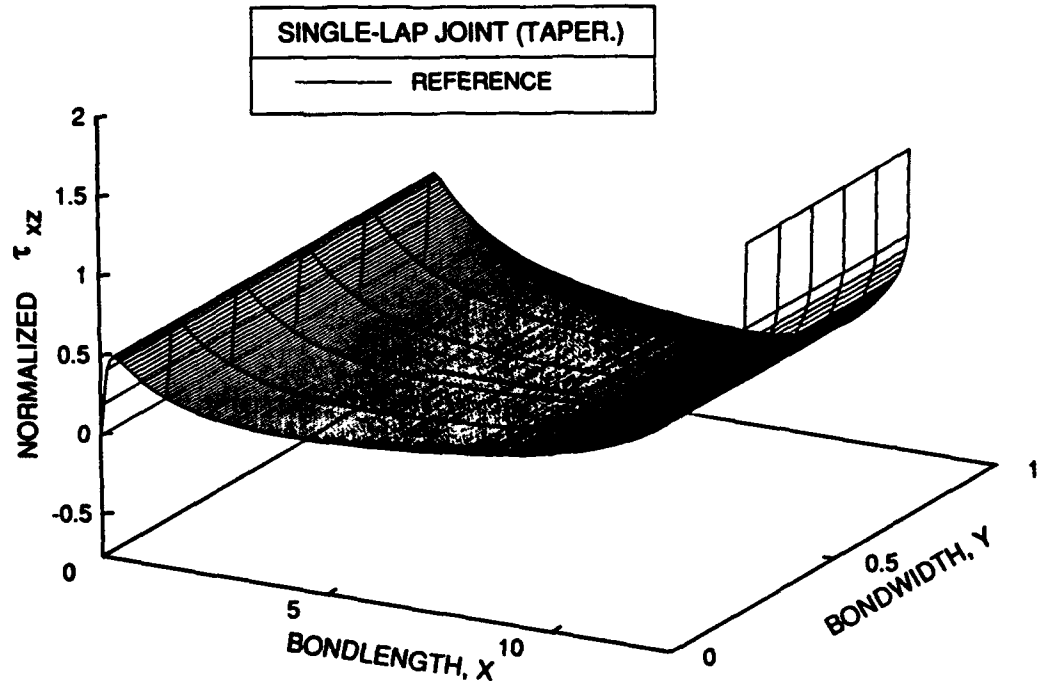

Figure 69. Reference τ_{xz} stress distribution in the tapered 3-D single-lap joint.

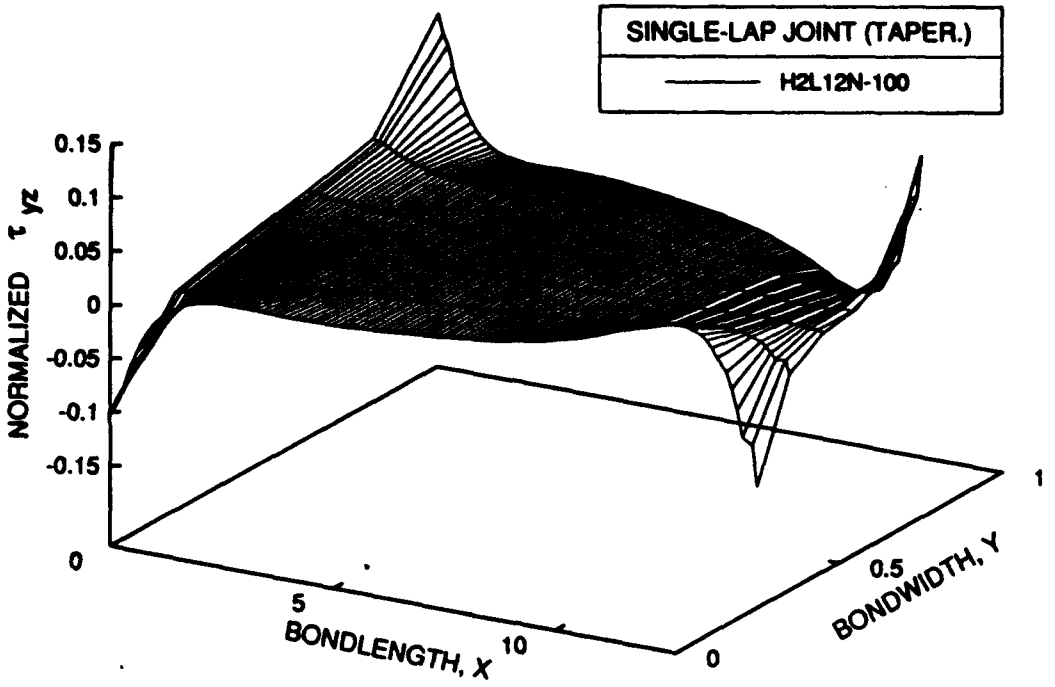

Figure 70. Singular τ_{yz} stress field in the tapered 3-D single-lap joint.

From the detailed study of various 2-D element performance, the optimum element configuration for use in general 3-D applications is selected as a two-layer formulation incorporating bilinear isoparametric assumed displacement fields and using the complete Hellinger-Reissner functional in which all field equilibrium and interface continuity conditions are identically satisfied. No convergence studies are performed in the 3-D case; the degree of discretization is fixed at 100 elements along the bondline with 5 elements through the width. The lack of mesh refinement through the joint width is due to the assumption of negligible 3-D stress variations. Results are compared with stress predictions using 8-node C3D8 displacement-based solid elements available from the ABAQUS library and the reference solution.

7.1 The H2L12N Element

The H2L12N element is formulated as a 12-node, two layer element as shown in Figure 71.

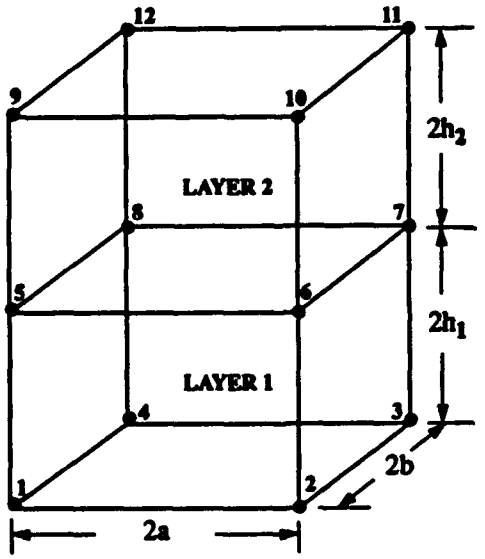

Figure 71. The H2L12N element configuration.

As a 3-D extension of the H2L6N element, two versions were developed in which complete linear and quadratic order expansions were assumed for each stress component. Equilibrium is enforced within each layer and continuity of the σ_{zz}, τ_{xz} and τ_{yz} stress components imposed at the layer interface. The H2L12N element is formulated to represent a general planform geometry to provide a robust element for 3-D analysis of arbitrary adhesive joint configurations.

The linear stress field contains 48 independent stress modes and is given by

$$
\begin{aligned}
\sigma^1_{xx} &= \beta_1 - x\beta_2 - x\beta_3 + y\beta_4 + z\beta_5 - xy\beta_6 - xz\beta_7 + zy\beta_8 \\
\sigma^1_{yy} &= \beta_9 + x\beta_{10} + y\beta_{11} + z\beta_{12} + xy\beta_{13} + xz\beta_{14} - zy\beta_{15} \\
\sigma^1_{zz} &= \beta_{18} + (h_1 + h_2 - z)\beta_{16} + (h_1 + h_2 - z)\beta_{17} + x(h_1 + h_2 - z)\beta_{19} + x\beta_{20} + \\
&\quad y(h_1 + h_2 - z)\beta_{21} + y\beta_{22} + xy\beta_{23} \\
\tau^1_{yz} &= \beta_{27} + (z - h_1)\beta_{25} - h_2\beta_{28} + x(h_1 - z)\beta_{13} + x\beta_{29} + h_2x\beta_{30} + y\beta_{17} + xy\beta_{19} \\
\tau^1_{zx} &= \beta_{31} + (z - h_1)\beta_3 - h_2\beta_{32} + x\beta_{16} + y(z - h_1)\beta_6 + y\beta_{33} - h_2y\beta_{34} + xy\beta_{21} \\
\tau^1_{xy} &= \beta_{24} - x\beta_{11} - x\beta_{25} + y\beta_2 + z\beta_{26} + xz\beta_{15} + zy\beta_7 \\
\sigma^2_{xx} &= \beta_{35} - x\beta_{36} - x\beta_{32} + y\beta_{37} + z\beta_{38} - xy\beta_{34} - xz\beta_{39} + yz\beta_{40} \\
\sigma^2_{yy} &= \beta_{41} + x\beta_{42} + y\beta_{47} + z\beta_{43} + xy\beta_{30} + xz\beta_{44} - zy\beta_{45} \\
\sigma^2_{zz} &= \beta_{18} + x\beta_{20} + y\beta_{22} - z\beta_{16} - z\beta_{17} + xy\beta_{23} - xz\beta_{19} - zy\beta_{21} \\
\tau^2_{yz} &= \beta_{27} + x\beta_{29} + y\beta_{17} + z\beta_{28} + xy\beta_{19} - xz\beta_{30} \\
\tau^2_{zx} &= \beta_{31} + x\beta_{16} + y\beta_{33} + z\beta_{32} + xy\beta_{21} + yz\beta_{34} \\
\tau^2_{xy} &= \beta_{46} - x\beta_{47} - x\beta_{28} + y\beta_{36} + z\beta_{48} + xz\beta_{45} + zy\beta_{39}
\end{aligned}
\tag{62}
$$

The quadratic stress field contains 78 independent stress modes and is given by

$$
\begin{aligned}
\sigma^1_{xx} &= \beta_{10} + yz\beta_1 + xz\beta_2 + z\beta_3 + y^2\beta_4 + x^2\beta_5 + xy\beta_6 + y\beta_7 + x\beta_8 + z^2\beta_9 \\
\sigma^1_{yy} &= \beta_{19} + yz\beta_{11} + xz\beta_{12} + z\beta_{13} + y^2\beta_{14} + x^2\beta_{15} + xy\beta_{16} + y\beta_{17} + x\beta_{18} + z^2\beta_{20} \\
\sigma^1_{zz} &= \beta_{30} + z(z - 2h_1)\beta_{21} + yz\beta_{22} + xz\beta_{23} + z\beta_{24} + y^2\beta_{25} + x^2\beta_{26} + xy\beta_{27} + y\beta_{28} + \\
&\quad x\beta_{29} - 2zh_2\beta_{31} \\
\tau^1_{yz} &= \beta_{43} + y(2h_1 - z)\beta_{21} - xy\beta_{23} - y\beta_{24} - yz\beta_{14} - 2xz\beta_{34} - xz\beta_{16} - z\beta_{17} - y\beta_{41} + \\
&\quad x\beta_{42} - z\beta_{36} + 2yh_2\beta_{31} + z^2\beta_{39} + yz\beta_5 + y^2\beta_{44} - 2xy\beta_{45} + x^2\beta_{46} \\
\tau^1_{zx} &= \beta_{48} - xy\beta_{22} - 2yz\beta_{33} + xz\beta_{14} + y\beta_{47} - z\beta_{35} + x\beta_{41} + z^2\beta_{38} - xz\beta_5 - yz\beta_6 - \\
&\quad xz\beta_{21} - z\beta_8 + y^2\beta_{49} - 2xy\beta_{44} + x^2\beta_{45} \\
\tau^1_{xy} &= \beta_{37} - yz\beta_2 - xz\beta_{11} + z\beta_{32} + y^2\beta_{33} - xy\beta_{14} + x^2\beta_{34} + y\beta_{35} + x\beta_{36} - 2yz\beta_{38} - \\
&\quad 2xz\beta_{39} - xy\beta_5 + z^2\beta_{40} + xy\beta_{21} \\
\sigma^2_{xx} &= \beta_{58} + yz\beta_{50} + xz\beta_{51} + z\beta_{52} - 2xy\beta_{53} + y^2\beta_{54} + x^2\beta_{55} + y\beta_{56} + x\beta_{57} + z^2\beta_{59} - xy\beta_{60} \\
\sigma^2_{yy} &= \beta_{69} + yz\beta_{61} + xz\beta_{62} + z\beta_{63} + y^2\beta_{64} + x^2\beta_{65} + xy\beta_{66} + y\beta_{67} + x\beta_{68} + z^2\beta_{70} \\
\sigma^2_{zz} &= \beta_{30} + (-h_2^2 + z^2 - 2h_1h_2)\beta_{31} + y(h_2 + h_1 + z)\beta_{22} + x(h_2 + h_1 + z)\beta_{23} + (h_2 + h_1 + z)\beta_{24} + \\
&\quad y^2\beta_{25} + x^2\beta_{26} + xy\beta_{27} + y\beta_{28} + x\beta_{29} - h_1^2\beta_{21} \\
\tau^2_{yz} &= \beta_{43} + (z^2 - h_2^2)\beta_{77} + y(z + h_2)\beta_{55} - (h_2 + z)\beta_{67} + y(h_2 - z)\beta_{31} - y(z + h_2)\beta_{64} - x(z + h_2)\beta_{66} - \\
&\quad (h_2 + z)\beta_{73} - 2x(z + h_2)\beta_{72} - xy\beta_{23} - y\beta_{24} - h_1y\beta_{14} - 2h_1x\beta_{34} - h_1x\beta_{16} - h_1\beta_{17} - y\beta_{41} + \\
&\quad x\beta_{42} - h_1\beta_{36} + h_1^2\beta_{39} + h_1y\beta_5 + h_1y\beta_{21} + y^2\beta_{44} - 2xy\beta_{45} + x^2\beta_{46} \\
\tau^2_{zx} &= \beta_{48} + (z^2 - h_2^2)\beta_{76} + y(z + h_2)\beta_{60} + x(z + h_2)\beta_{64} - x(z + h_2)\beta_{55} - x(z + h_2)\beta_{31} + (h_2 + z)\beta_{75} - \\
&\quad xy\beta_{22} - 2h_1y\beta_{33} + h_1x\beta_{14} + y\beta_{47} - h_1\beta_{35} + x\beta_{41} + h_1^2\beta_{38} - h_1x\beta_5 - h_1y\beta_6 - h_1x\beta_{21} - \\
&\quad h_1\beta_8 + y^2\beta_{49} - 2xy\beta_{44} + x^2\beta_{45} \\
\tau^2_{xy} &= \beta_{74} - xz\beta_{61} - yz\beta_{51} + z\beta_{71} + y^2\beta_{53} - xy\beta_{64} + x^2\beta_{72} - xy\beta_{55} + x\beta_{73} - y\beta_{57} + xy\beta_{31} - \\
&\quad y\beta_{75} - 2yz\beta_{76} - 2xz\beta_{77} + z^2\beta_{78}
\end{aligned}
\tag{63}
$$

The effect of high aspect ratio is examined using the element configuration shown in Figure 72. Isotropic material properties were selected with $E = 1000.0$ and $\mu = 0.25$. An eigenanalysis of the two versions of H2L12N compared with a displacement-based formulation is depicted in Table 3 and shows the elimination of low-energy or 'weak' characteristic deformation modes by incorporating a higher-order expansion for the stresses. In addition, the hybrid formulation has the desirable feature of relieving the stiff deformation modes demonstrated in the displacement-based element.

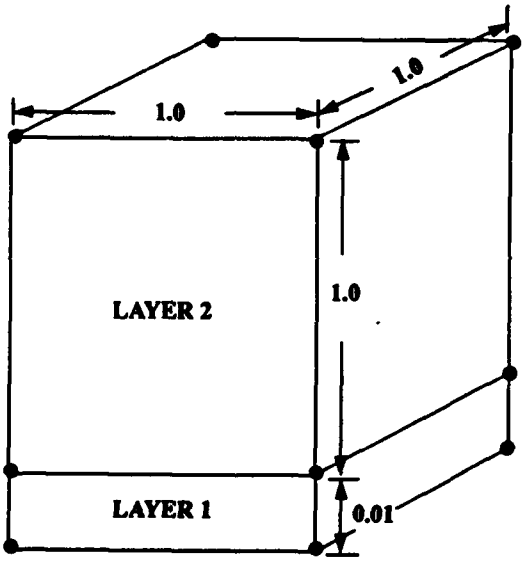

Figure 72. The H2L12N element with a high aspect ratio layer.

Table 3. Comparison of eigenvalues obtained in the H2L12N element incorporating complete linear and quadratic stress expansions with a displacement-based element.

λ	Linear Expansions	Quadratic Expansions	Disp.-Based
1	0.0	0.0	0.0
2	0.0	0.0	0.0
3	0.0	0.0	0.0
4	0.0	0.0	0.0
5	0.0	0.0	0.0
6	0.0	0.0	0.0
7	1.205410	2.532107	40.09000
8	1.205410	10.11471	50.37687
9	1.419593	10.11471	68.25251
10	4.272703	22.95363	68.25251
11	22.60332	35.13044	84.25569
12	29.99786	45.20570	122.9616
13	42.86800	72.59133	146.6858
14	61.04669	72.59133	146.6858
15	61.04669	77.22080	173.4341
16	67.45520	98.23903	197.0593
17	83.67022	116.6506	231.0399
18	83.67022	116.6506	231.0399
19	137.3086	175.6953	323.4468
20	137.3086	204.7085	326.4697
21	153.5916	204.9439	330.7372
22	157.4737	204.9439	331.6464
23	171.8504	210.0055	331.6464
24	221.2042	235.4628	760.4554
25	223.5920	235.1390	2322.606
26	225.2890	246.5870	2322.606
27	225.2890	246.5870	6683.630
28	295.3580	356.1471	6723.343
29	359.8182	487.7587	6820.932
30	359.8182	487.7587	6827.265
31	416.4106	499.1765	6969.071
32	491.4209	506.5908	20025.89
33	617.3870	679.0603	20025.89
34	681.1891	1077.723	20144.81
35	681.1891	1077.723	20144.81
36	1225.438	1567.056	60153.68

Figures 73 through 78 depict stress predictions over the bond surface and along the centerline for a 3-D single-lap adhesive joint with a rectangular planform. Solutions are obtained for the normal peel stress distribution, σ_{zz}, and the transverse shear stress distribution, τ_{xz}, across the bond surface. Quadratic stress fields are assumed in the H2L12N element and stress predictions are compared to results obtained using displacement-based elements and the reference solution.

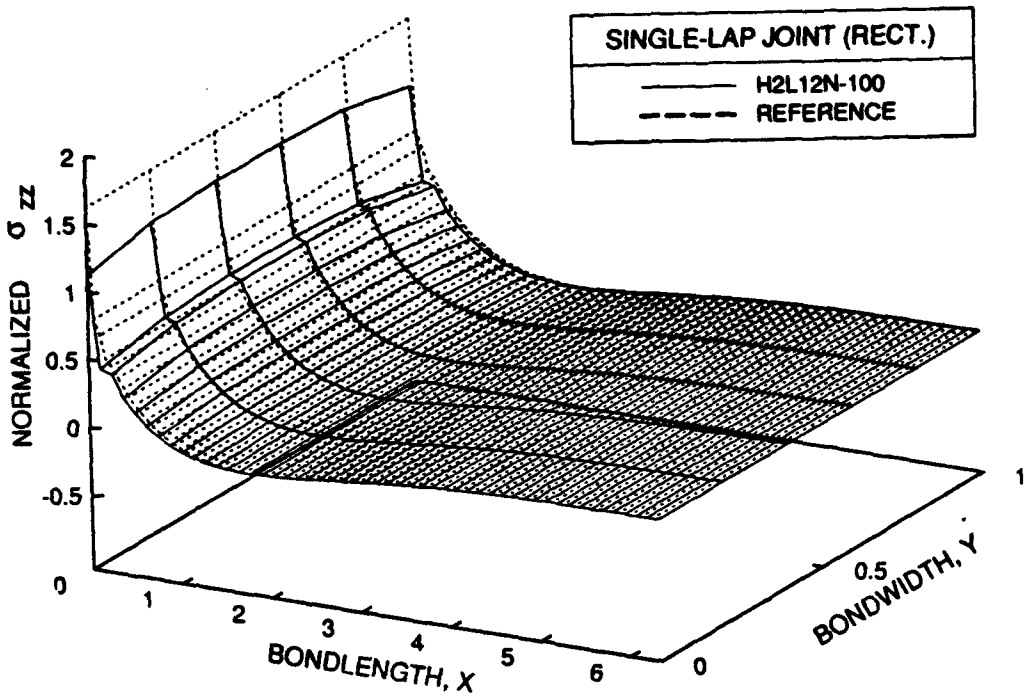

Figure 73. H2L12N σ_{zz} stress prediction over the bond surface in rectangular 3-D single-lap joint.

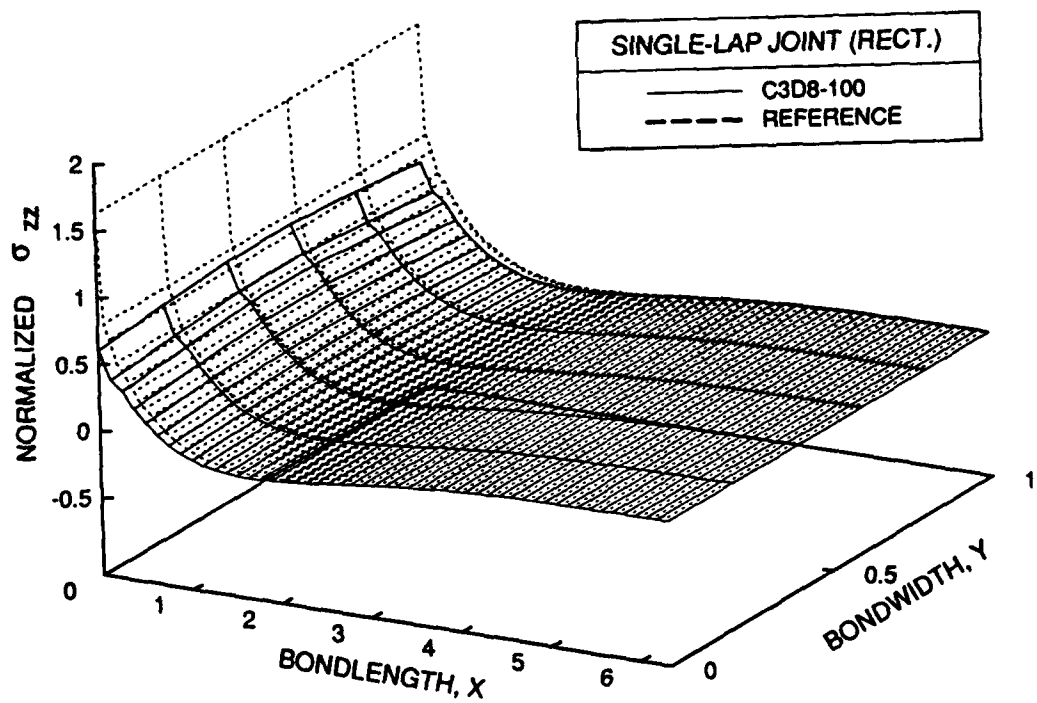

Figure 74. C3D8 σ_{zz} stress prediction over the bond surface in rectangular 3-D single-lap joint.

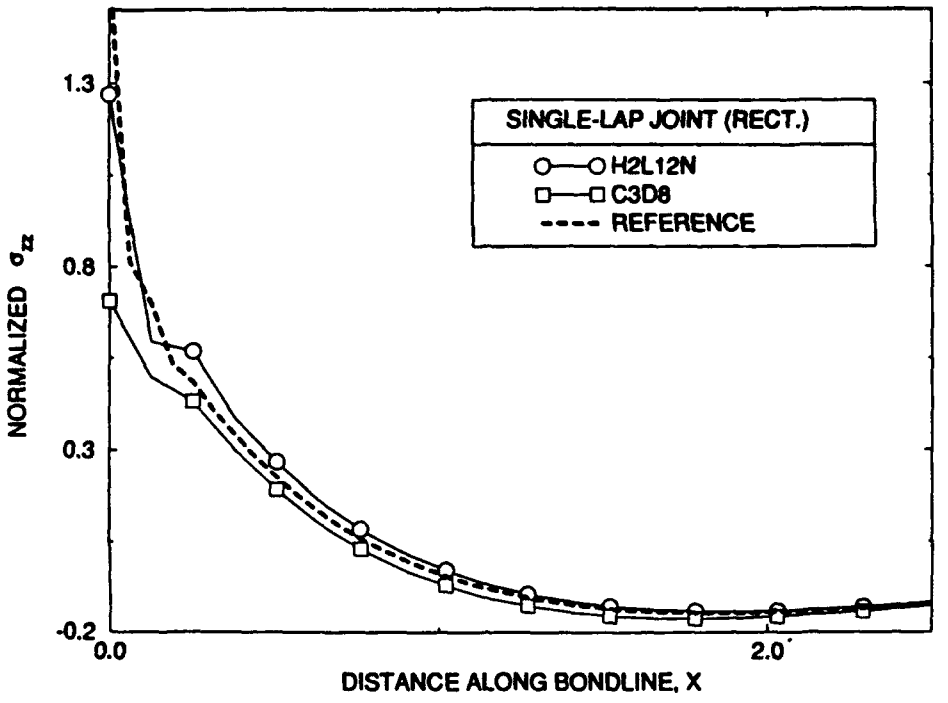

Figure 75. σ_{zz} stresses along centerline of adhesive bond in rectangular 3-D single-lap joint.

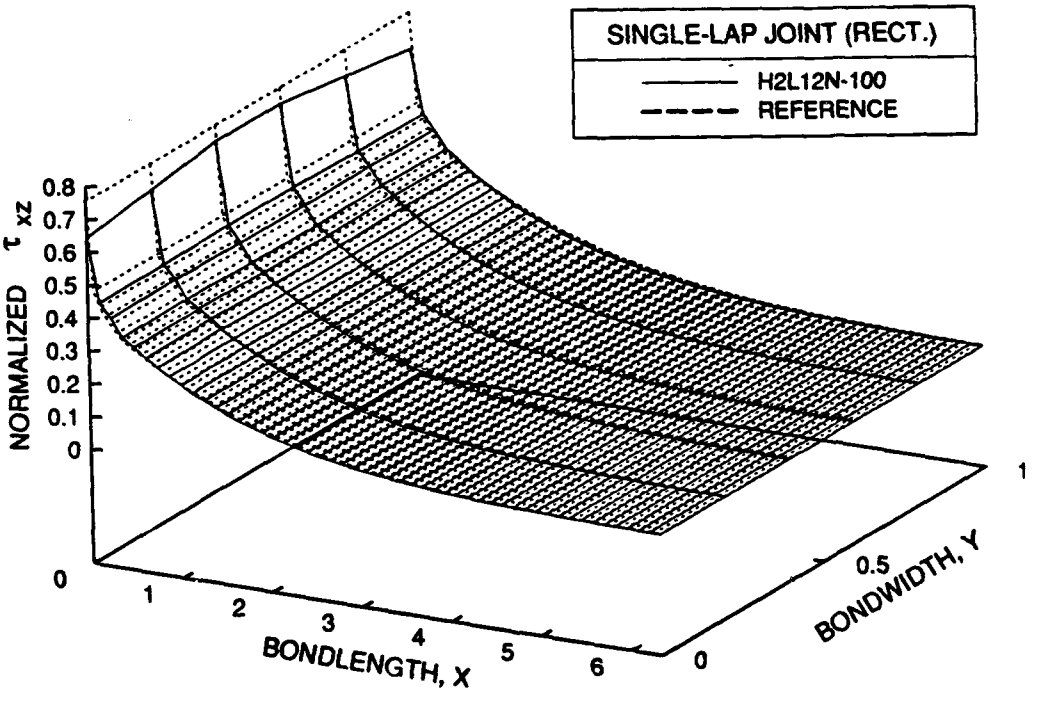

Figure 76. H2L12N τ_{xz} stress prediction over the bond surface in rectangular 3-D single-lap joint.

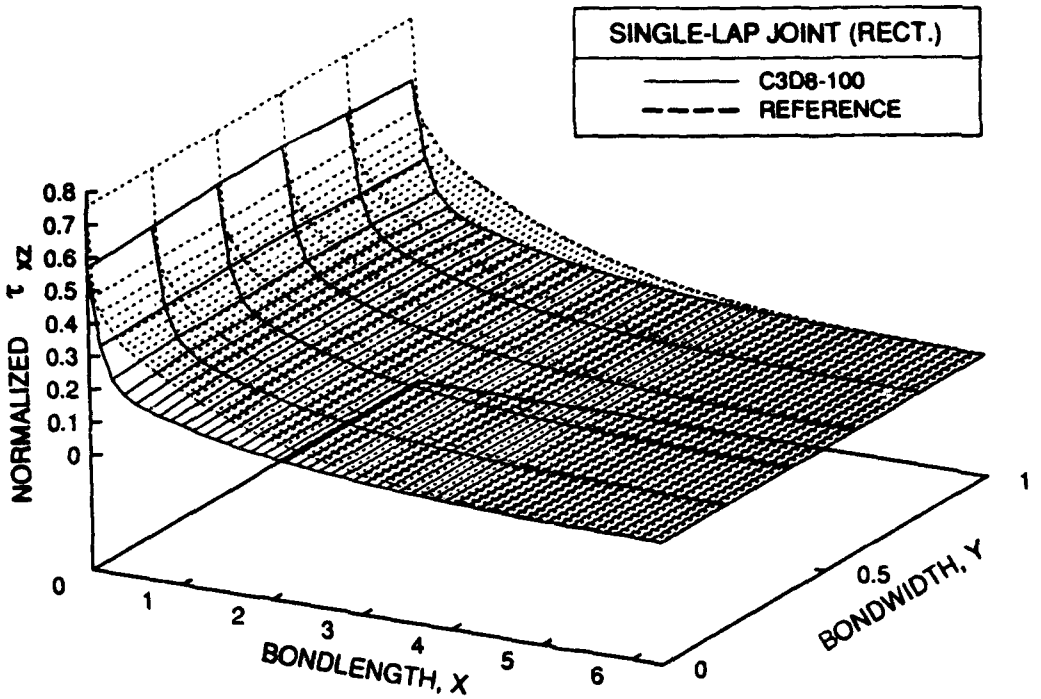

Figure 77. C3D8 τ_{xz} stress prediction over the bond surface in rectangular 3-D single-lap joint.

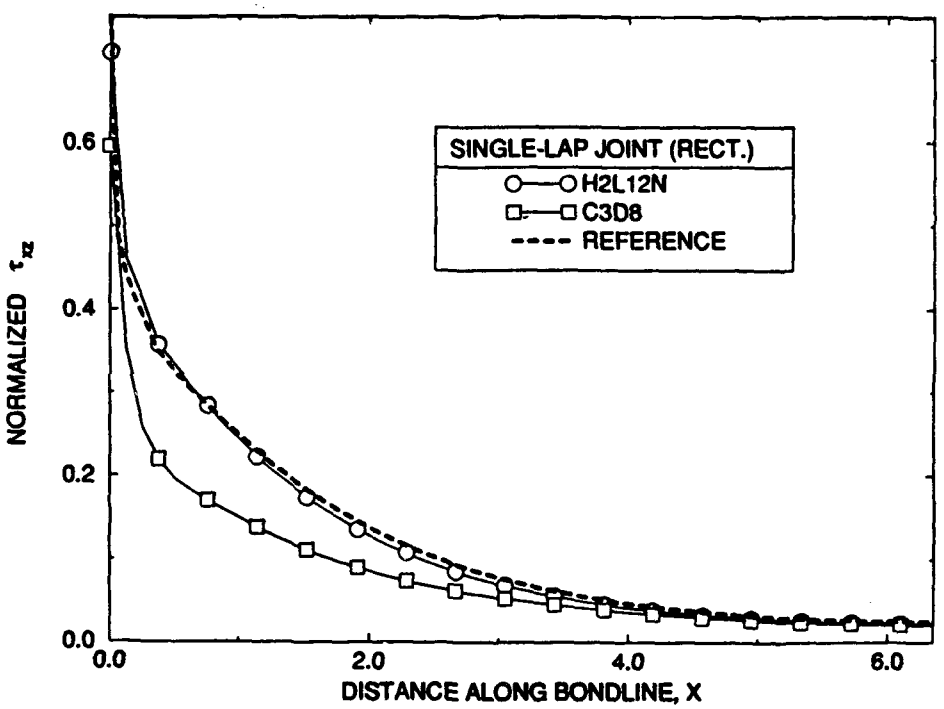

Figure 78. τ_{xz} stresses along centerline of adhesive bond in rectangular 3-D single-lap joint.

As shown, the H2L12N element predictions are excellent while the displacement-based element solutions converge away from the reference solution. The slight departure from the reference solution is attributed to the deviation from a state of plane-strain due to the three-dimensional nature of the singularities in the τ_{yz} stress field which influences σ_{zz} and τ_{xz} through the equilibrium constraints.

Stress predictions are obtained for the normal peel stress distribution, σ_{zz}, and the transverse shear stress distribution, τ_{xz}, across the bond surface in a tapered joint and are shown below in Figures 79 through 84

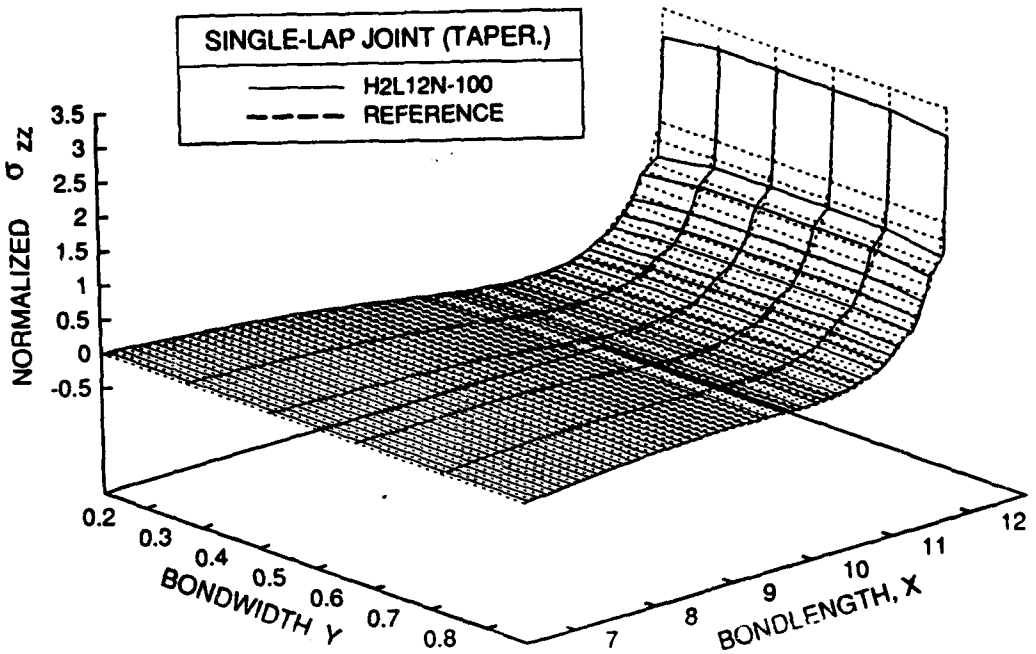

Figure 79. H2L12N σ_{zz} stress prediction over the bond surface in a tapered 3-D single-lap joint.

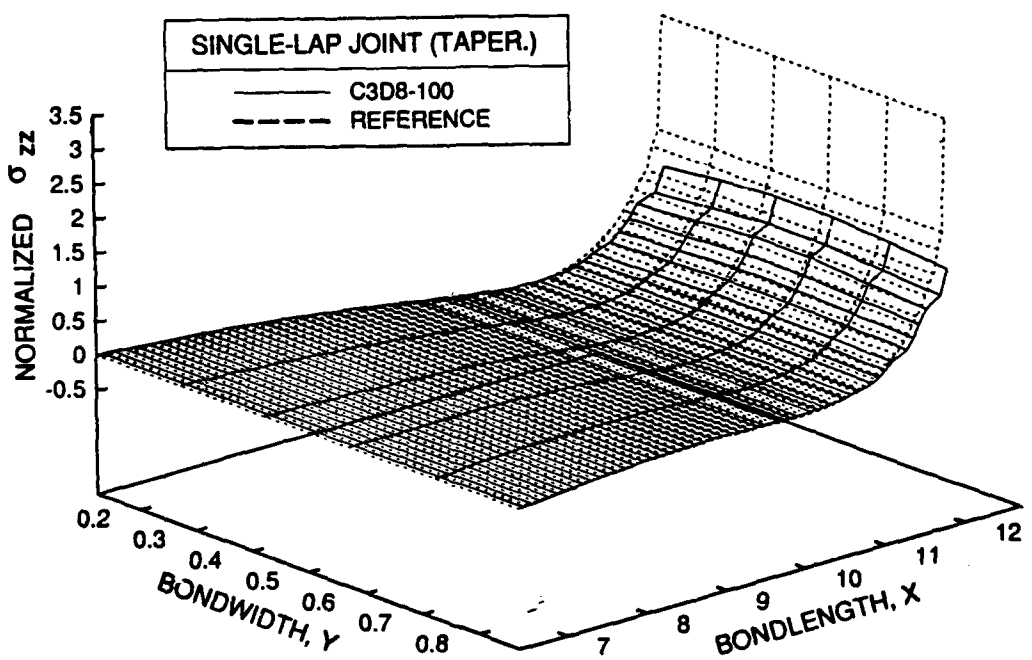

Figure 80. C3D8 σ_{zz} stress prediction over the bond surface in a tapered 3-D single-lap joint.

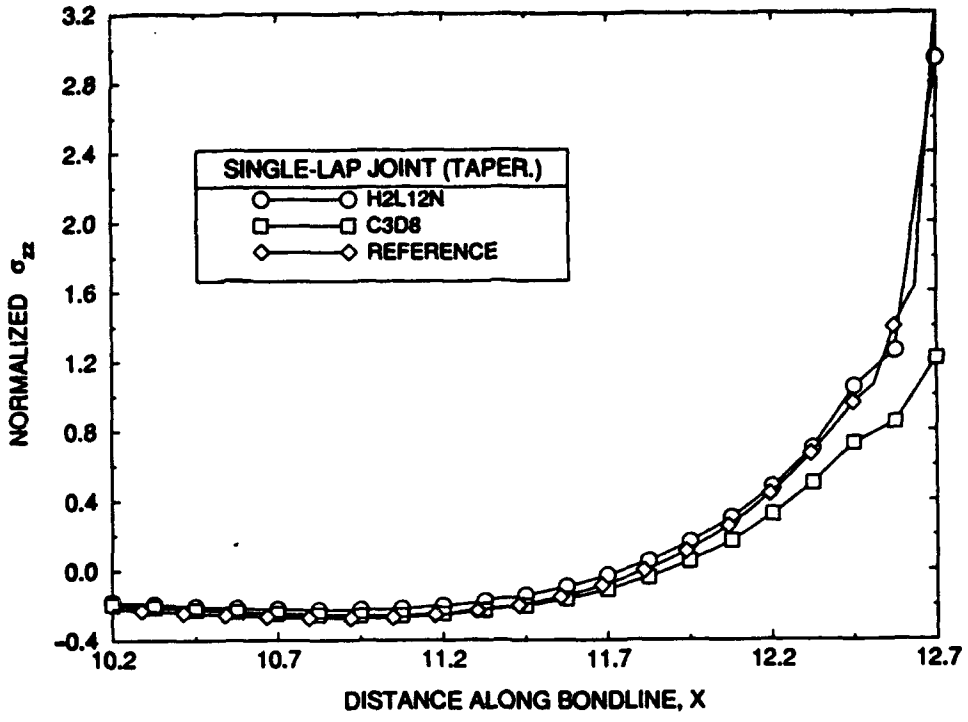

Figure 81. σ_{zz} stresses along centerline of adhesive bond in a tapered 3-D single-lap joint.

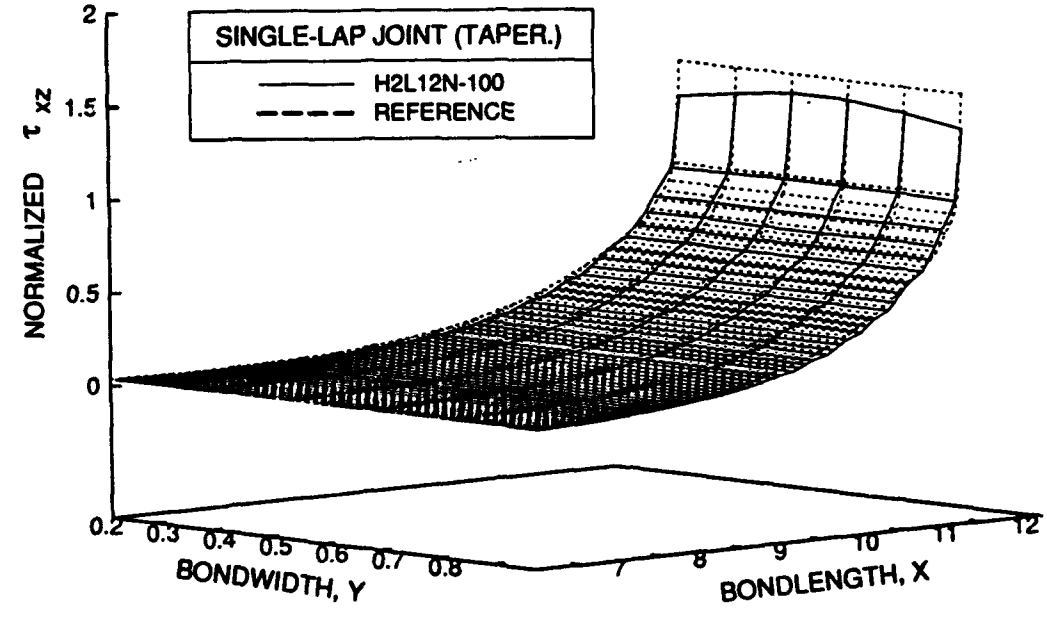

Figure 82. H2L12N τ_{xz} stress prediction over the bond surface in a tapered 3-D single-lap joint.

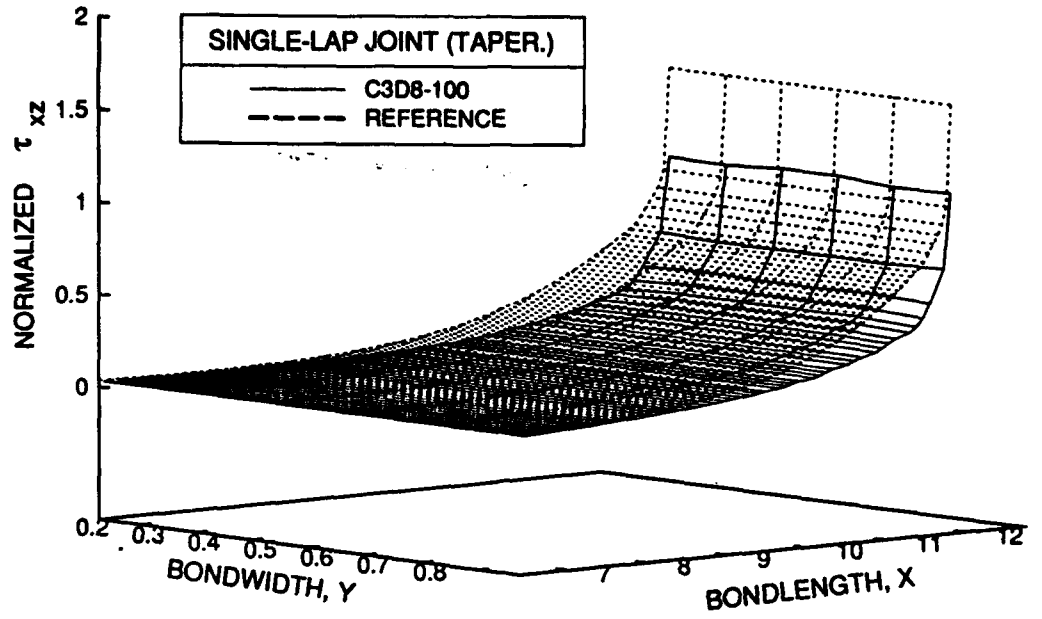

Figure 83. C3D8 τ_{xz} stress prediction over the bond surface in a tapered 3-D single-lap joint.

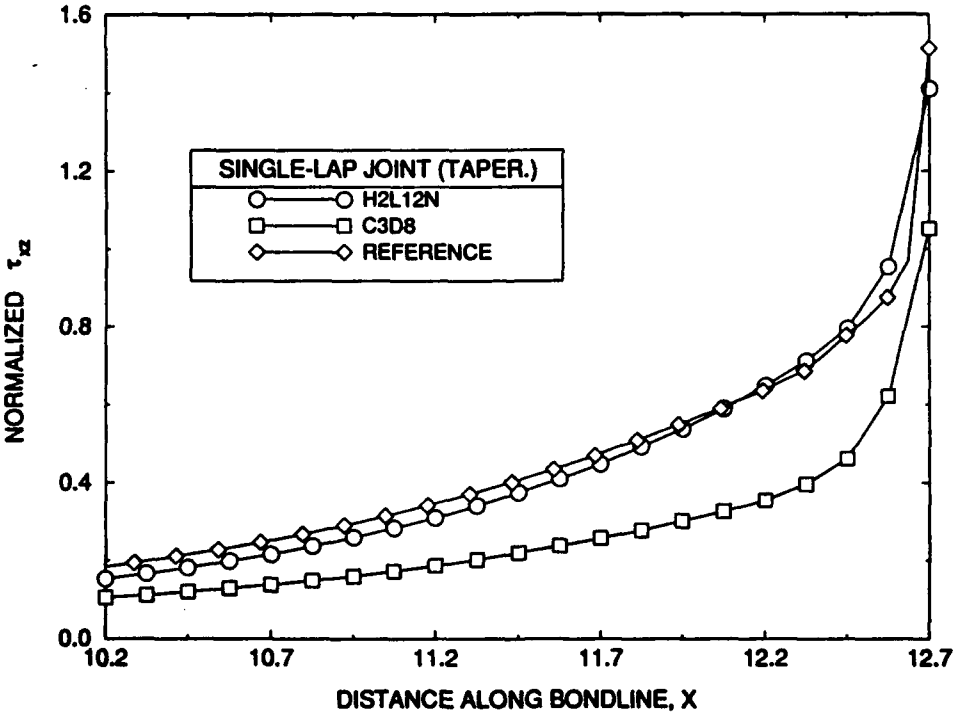

Figure 84. τ_{xz} stresses along centerline of adhesive bond in a tapered 3-D single-lap joint.

7 2 Remarks on 3-D Element Performance

The H2L12N element demonstrates the same improvement over displacement-based 8-node solid elements as was shown in the assessment of the 2-D H2L6N element. The 3-D element formulation developed herein permits a general adhesive joint planform to be modelled and demonstrates ideal flexible behavior in high aspect ratio element configurations.

8 Closure

Numerous specialized layered element formulations have been derived to fully assess the performance of the hybrid element technique in the application to improve the computational efficiency and accuracy of determining critical stresses along the bond interfaces in adhesive joints. The best performing elements have been the lower-order element formulations due to the difficulty encountered with the zero energy modes present in the higher-order layered elements. Optimal element performance has been associated with the strict enforcement of all layer equilibrium and interface continuity constraints. A clear improvement in stress prediction has been demonstrated over the use of displacement-based element which validates the superior behavior of the hybrid stress technique in this particular application. For a robust finite element-based analytical framework for the study of adhesive bond stresses, the optimum element configurations developed herein are expected to form the basis for further development. Future work is suggested in the incorporation of incompatible displacement modes in 2-D lower-order elements to enhance the derived elements for problems involving significant bending stresses. Nonlinear material behavior should be supported in future efforts to predict the reduction of peak stress due to plastic material yielding at the joint ends together with the capability to model large displacements which occur in various adhesive joint configurations under peak service loading. Finally, a local failure analysis methodology should be developed, perhaps including a micromechanical level analysis of the adhesive/adherend interface, to predict the initiation of bond failure.

Acknowledgment

The authors are indebted to Prof. T. H. H. Pian, who originally developed the hybrid stress technique, for acting as consultant and providing invaluable guidance through the first phase of this research. Early results on the success of the 2-D layered adhesive element were published by Prof. Pian in Reference [37].

References

[1] M. Golan and E. Reissner, 'Stresses in cemented joints,' *J. Appl. Mech, Trans ASME* **11**, A17-A27, (1944).

[2] L. J. Hart-Smith, 'Adhesive-bonded single-lap joints,' NASA CR-112236, Jan. (1973)

[3] I. U. Ojalvo and H. L. Eidinoff, 'Bond thickness effects upon stresses in single-lap adhesive joints', *AIAA Journal* **16**, No. **3** pp. 204-211, (1977).

[4] W. J. Renton and J. R. Vinson, 'Analysis of adhesively bonded joints between panels of composite materials', *J. of Appl. Mech* pp. 101-106, (1977).

[5] D. Chen and S. Cheng, 'An analysis of adhesive-bonded single-lap joints', *J. Appl. Mech* **50**, pp. 109-115, (1983).

[6] J. A. Harris and R. D. Adams, 'Strength prediction of bonded single lap joints by non-linear finite element methods,' *Int. J. Adhesion and Adhesives*, **4**, No. **2** pp. 65-78 (1984).

[7] S. Amijima and T. Fujii, 'Extension of a one-dimensional finite element model program for analysing elastic-plastic stresses and progressive failure of adhesive bonded joints,' *Int. J. Adhesion and Adhesives*, Oct. pp. 243-249, (1989).

[8] F. Delale and F. Erdogan, 'Viscoelastic analysis of adhesively bonded joints,' *J. Applied Mech.*, Vol. **48**, pp. 331-338, (1981).

[9] S. Yadagiri, C. P. Reddy and T. S. Reddy, 'Viscoelastic analysis of adhesively bonded joints,' *Comp. and Struct.*, Vol. **27**, No. **4**, pp. 445-454, (1987).

[10] U. Edlund and A. Klarbring, 'A geometrically nonlinear model of the adhesive joint problem and its numerical treatment,' *Comp. Meth. Appl'd. Mech. and Eng.*, **96**, pp. 329-350, (1992).

[11] K. Temma, T. Sawa and A. Iwata, 'Three-dimensional stress analysis of adhesive butt joints with disbonded areas and spew fillets,' *Int. J. Adhesion and Adhesive*, Vol. bf 10, No. **4**, pp. 294-300, (1990).

[12] R. D. Adams and J. A. Harris, 'The influence of local geometry on the strength of adhesive joints,' *Int. J. Adhesion and Adhesives*, pp. 69-80, (1987).

[13] G. R. Wooley and D. R. Carver, 'Stress concentration factors for bonded lap joints,' *AIAA Journal* **8**, No. **10** pp. 817-820, (1971).

[14] R. D. Adams and N. A. Peppiatt, 'Stress analysis of adhesive-bonded lap joints,' *J. of Strain Anal.* **9**, No. **3** pp. 185-196, (1972).

[15] A. K. Pickett and L. Hollaway, 'The analysis of elastic adhesive stresses in bonded lap joints in FRP structures,' *Comp. Struct.* **3** pp. 55-79, (1985).

[16] A. J. Kinloch, *Adhesion and Adhesives* Chapman and Hall, (1986).

[17] P. Destuynder, F. Michavila and A. Santos, 'Some theoretical aspects in computational analysis of adhesive lap joints,' *Int. J. Num. Meth. Engrg* **35**, pp. 1237-1262, (1992).

[18] N. L. Harrison and W. J. Harrison, 'The stresses in an adhesive layer,' *J. Adhesion*, Vol. **3**, pp. 195-212, (1972).

[19] Y. Weitsman, 'Stresses in adhesive joints due to moisture and temperature,' *J. Comp. Mat.*, Vol. **11**, pp. 378-394, (1977).

[20] D. A. Bigwood and A. D. Crocombe, 'Elastic analysis and engineering design formulae for bonded joints,' *Int. J. Adhesion and Adhesive*, Vol. **9**, No. **4**, pp. 229-242, (1989).

[21] D. J. Allman, 'A theory for elastic stresses in adhesive bonded lap joint,' *Q. J. Mech. Appl. Math*, Vol. xxx, Pt. 4, (1977).

[22] R. D. Adams and N. A. Peppiatt, 'Stress analysis of adhesive bonded tubular lap joints,' *J. Adhesion* 9, pp. 1-18, (1977).

[23] K. Temma, T. Sawa and A. Iwata, 'Two-dimensional stress analysis of adhesive butt joints subjected to cleavage loads,' *Int. J. Adhesion and Adhesive*, Vol. 10, No. 4, pp. 285-293, (1990).

[24] A. S. Kuo, 'A two-dimensional shear spring element,' *AIAA Journal* 22, No. 10 pp. 1460-1464, (1983).

[25] R. M. Barker and F. Hatt, 'Analysis of bonded joints in vehicular structures,' *AIAA Journal* 11, No. 12 pp. 1650-1654, (1973).

[26] W. C. Carpenter, 'Stresses in bonded connections using finite elements,' *Int. J. of Numer. Meth. Engrg* 15 pp. 1659-1680, (1980).

[27] H. L. Goth, 'Calculation of stresses in bonded joints using the substructuring technique,' *Int. J. Adhesion and Adhesives*, Vol. 6, No. 1, pp. 31-35, (1986).

[28] S. Aivazzadeh and G. Verchery, 'Stress analysis at the interface in adhesive joints by special finite elements,' *Int. J. Adhesion and Adhesives*, Vol. 6, No. 4, pp. 185-187, (1986).

[29] T. H. H. Pian and K. Sumihara, 'Rational approach for assumed stress finite element', *Int. J. Num. Meth. Engrg.* 20, 1685-1695, (1984).

[30] O. C. Zienkiewicz and R. L. Taylor, *The Finite Element Method*, Vol. I, *Basic Introduction and Linear Problems*, 4th edn. McGraw-Hill (1989).

[31] H. S. Jing and M. L. Liao, 'Partial hybrid stress element for the analysis of thick laminated composite plates,' *Int. J. Num. Meth. Engrg.* 28, 2813-2827, (1989).

[32] T. H. H. Pian and D.P. Chen, 'On the suppression of zero energy deformation modes,' *Int. J. Num. Meth. Engrg.* 19, 1741-1752 (1983).

[33] T. H. H. Pian and C.C. Wu, 'A rational approach for choosing stress terms for hybrid finite element formulations,' *Int. J. Num. Meth. Engrg.* 26, 2331-2343, (1988).

[34] E. Saether and K. Weight, 'User-defined subroutine for implementation of special finite elements in ABAQUS for the analysis of adhesive joints,' ARL-TR-450, U.S. Army Research Laboratory, June, (1994).

[35] E. Saether, 'Minimization of computational requirements in the hybrid stress finite element method,' ARL-TR-336, U.S. Army Research Laboratory, Feb. 1994.

[36] E. Saether, 'Explicit determination of element stiffness matrices in the hybrid stress method,' *Int. J. Num. Meth. Engrg.* (to appear).

[37] T. H. H. Pian 'Development of multi-layered hybrid stress elements for analyzing adhesive bond and thick composite structure,' Final Contract Report for Battelle, Columbus Div., No. DAAL03-86-D-001, (1992).

DISTRIBUTION LIST

No. of Copies	To
1	Office of the Under Secretary of Defense for Research and Engineering, The Pentagon, Washington, DC 20301
	Director, U.S. Army Research Laboratory, 2800 Powder Mill Road, Adelphi, MD 20783-1197
1	ATTN: AMSRL-OP-SD-TP, Technical Publishing Branch
1	AMSRL-OP-SD-TM, Records Management Administrator
	Commander, Defense Technical Information Center, Cameron Station, Building 5, 5010 Duke Street, Alexandria, VA 23304-6145
2	ATTN: DTIC-FDAC
1	MIA/CINDAS, Purdue University, 2595 Yeager Road, West Lafayette, IN 47905
	Commander, Army Research Office, P.O. Box 12211, Research Triangle Park, NC 27709-2211
1	ATTN: Information Processing Office
	Commander, U.S. Army Materiel Command, 5001 Eisenhower Avenue, Alexandria, VA 22333
1	ATTN: AMCSCI
	Commander, U.S. Army Materiel Systems Analysis Activity, Aberdeen Proving Ground, MD 21005
1	ATTN: AMXSY-MP, H. Cohen
	Commander, U.S. Army Missile Command, Redstone Arsenal, AL 35809
1	ATTN: AMSMI-RD-CS-R/Doc
	Commander, U.S. Army Armament, Munitions and Chemical Command, Dover, NJ 07801
2	ATTN: Technical Library
	Commander, U.S. Natick Research, Development and Engineering Center, Natick, MA 017 0
1	ATTN: DFAS-IN-, Technical Library
	Commander, U.S. Army Satellite Communications Agency, Fort Monmouth, NJ 07703
1	ATTN: Technical Document Center
	Commander, U.S. Army Tank-Automotive Command, Warren, MI 48397-5000
1	ATTN: AMSTA-ZSK
1	AMSTA-TSL, Technical Library
	President, Airborne, Electronics and Special Warfare Board, Fort Bragg, NC 28307
1	ATTN: Library
	Director, U.S. Army Research Laboratory, Weapons Technology, Aberdeen Proving Ground, MD 21005-5066
1	ATTN: AMSRL-WT

No. of Copies	To
	Commander, Dugway Proving Ground, UT 84022
1	ATTN: Technical Library, Technical Information Division
	Commander, U.S. Army Research Laboratory, 2800 Powder Mill Road, Adelphi, MD 20783
1	ATTN: AMSRL-SS
	Director, Benet Weapons Laboratory, LCWSL, USA AMCCOM, Watervliet, NY 12189
1	ATTN: AMSMC-LCB-TL
1	AMSMC-LCB-R
1	AMSMC-LCB-RM
1	AMSMC-LCB-RP
	Commander, U.S. Army Foreign Science and Technology Center, 220 7th Street, N.E., Charlottesville, VA 22901-5396
3	ATTN: AIFRTC, Applied Technologies Branch, Gerald Schlesinger
	Commander, U.S. Army Aeromedical Research Unit, P.O. Box 577, Fort Rucker, AL 36360
1	ATTN: Technical Library
	U.S. Army Aviation Training Library, Fort Rucker, AL 36360
1	ATTN: Building 5906-5907
	Commander, U.S. Army Agency for Aviation Safety, Fort Rucker, AL 36362
1	ATTN: Technical Library
	Commander, Clarke Engineer School Library, 3202 Nebraska Ave., N, Fort Leonard Wood, MO 65473-5000
1	ATTN: Library
	Commander, U.S. Army Engineer Waterways Experiment Station, P.O. Box 631, Vicksburg, MS 39180
1	ATTN: Research Center Library
	Commandant, U.S. Army Quartermaster School, Fort Lee, VA 23801
1	ATTN: Quartermaster School Library
	Naval Research Laboratory, Washington, DC 20375
2	ATTN: Dr. G. R. Yoder - Code 6384
	Chief of Naval Research, Arlington, VA 22217
1	ATTN: Code 471
	Commander, U.S. Air Force Wright Research & Development Center, Wright-Patterson Air Force Base, OH 45433-6523
1	ATTN: WRDC/MLLP, M. Forney, Jr.
1	WRDC/MLBC, Mr. Stanley Schulman
	U.S. Department of Commerce, National Institute of Standards and Technology, Gaithersburg, MD 20899
1	ATTN: Stephen M. Hsu, Chief, Ceramics Division, Institute for Materials Science and Engineering

No. of Copies	To
1	Committee on Marine Structures, Marine Board, National Research Council, 2101 Constitution Avenue, N.W., Washington, DC 20418
1	Materials Sciences Corporation, Suite 250, 500 Office Center Drive, Fort Washington, PA 19034
1	Charles Stark Draper Laboratory, 555 Technology Square, Cambridge, MA 02139
	Wyman-Gordon Company, Worcester, MA 01601
1	ATTN: Technical Library
	General Dynamics, Convair Aerospace Division, P.O. Box 748, Fort Worth, TX 76101
1	ATTN: Mfg. Engineering Technical Library
	Plastics Technical Evaluation Center, PLASTEC, ARDEC, Bldg. 355N, Picatinny Arsenal, NJ 07806-5000
1	ATTN: Harry Pebly
1	Department of the Army, Aerostructures Directorate, MS-266, U.S. Army Aviation R&T Activity - AVSCOM, Langley Research Center, Hampton, VA 23665-5225
1	NASA - Langley Research Center, Hampton, VA 23665-5225
	U.S. Army Vehicle Propulsion Directorate, NASA Lewis Research Center, 2100 Brookpark Road, Cleveland, OH 44135-3191
1	ATTN: AMSRL-VP
	Director, Defense Intelligence Agency, Washington, DC 20340-6053
1	ATTN: ODT-5A (Mr. Frank Jaeger)
	U.S. Army Communications and Electronics Command, Fort Monmouth, NJ 07703
1	ATTN: Technical Library
	U.S. Army Research Laboratory, Electronic Power Sources Directorate, Fort Monmouth, NJ 07703
1	ATTN: Technical Library
	Director, U.S. Army Research Laboratory, Watertown, MA 02172-0001
2	ATTN: AMSRL-OP-WT-IS, Technical Library
10	Authors